MODELING LUNG TISSUE MOTIONS AND DEFORMATIONS: APPLICATIONS IN TUMOR ABLATIVE PROCEDURES

(Spine title: Modeling Lung Tissue Motions and Deformations)

(Thesis format: Integrated Article)

by

Ali Sadeghi Naini

Graduate Program
in
Electrical and Computer Engineering
Biomedical Systems

A thesis submitted in partial fulfillment
of the requirements for the degree of
Doctor of Philosophy

The School of Graduate and Postdoctoral Studies
The University of Western Ontario
London, Ontario, Canada

THE UNIVERSITY OF WESTERN ONTARIO
School of Graduate and Postdoctoral Studies

CERTIFICATE OF EXAMINATION

Supervisors

Dr. Abbas M. Samani

Dr. Rajni V. Patel

Supervisory Committee

Dr. Hanif M. Ladak

Dr. Ting-Yim Lee

Examiners

Dr. James C. Lacefield
(ECE, MBP, RRI, University of Western Ontario)

Dr. Serguei L. Primak
(ECE, University of Western Ontario)

Dr. David W. Holdsworth
(SRG, MBP, RRI, University of Western Ontario)

Dr. Jeffrey H. Siewerdsen
(BME, School of Medicine, John Hopkins University)

The thesis by

Ali Sadeghi Naini

entitled:

Modeling Lung Tissue Motions and Deformations: Applications in Tumor Ablative Procedures

is accepted in partial fulfillment of the
requirements for the degree of
Doctor of Philosophy

May 25, 2011
Date

Dr. James A. Voogt
Chair of the Thesis Examination Board

Abstract

Various types of motion and deformation that the lung undergoes during minimally invasive tumor ablative procedures have been investigated and modeled in this dissertation. The lung frequently undergoes continuous large respiratory deformation, which can greatly affect the pre-planned outcome of the operation, hence deformation compensation becomes necessary. The first type of major deformation involved in a target lung throughout a tumor ablative procedure is the one encountered in procedures where the lung is totally deflated before starting the operation. A consequence of this deflation is that pre-operative images (acquired while the lung was partially inflated) become inaccurate for targeting the tumor. Another issue is that minimally invasive procedures usually employ intra-operative US imaging for guidance. However, US images of the deflated lung have very poor quality due to the small amount of air remaining in the deflated lung. To address the challenges associated with deflating the lung, a novel construction technique has been proposed in this thesis to obtain CT images of the totally deflated lung. This technique processes the lung's 4D-CT respiratory image sequence acquired pre-operatively. It consists of a deformable registration/air volume estimation/extrapolation pipeline. The pipeline does not require any external marker as it is capable of estimating the lung's air volume from the CT images automatically using a newly developed segmentation approach introduced in this thesis. To deal with poor quality issue of the US image, a novel registration strategy has been introduced to enhance the quality of the lung's intra-operative US image by employing the constructed high quality CT image. The second major type of lung deformation tackled in this thesis is the one due to respiratory anatomical contact forces or needle insertion, which can be characterized using tissue biomechanical models. Two essential prerequisites of developing such models are realistic biomechanical parameters of the lung soft tissue, and proper lung tissue discretization, for which inevitable, yet reasonable, geometry simplification should be incorporated. These two critical necessities have been investigated in the last two parts of this thesis. The results reported in these parts have paved the way for accurate biomechanical modeling of the lung for predicting tissue deformation resulting from contact forces and needle insertion in future studies.

Keywords

Lung Cancer, Respiratory Motion, Lung Deformation, Tumor Ablative Procedures, Brachytherapy, Respiratory Sequence, 4D-CT, Modeling, Deformable Models, Image Registration, Lung's Air Volume Estimation, Image Segmentation, Ultrasound Image Enhancement, Lung Tissue Properties, Hyperelastic Parameters, Geometry Simplification, Neglecting Lung's Non-significant Airways.

Co-Authorship Statement

This thesis has been written by Ali Sadeghi Naini under supervision of Dr. Abbas Samani and Dr. Rajni V. Patel. Parts of the material presented in this thesis have been published in several peer-reviewed journal papers and refereed conference proceedings as listed below. The research presented in each publication has been conducted by the principal author and guided/supported by or in collaboration with the underlined authors who are the research supervisors or members of the supervisory committee.

The material presented in Chapter 2 has been published in: A. Sadeghi Naini, T. Y. Lee, R. V. Patel, A. Samani, "Estimation of lung's air volume and its variations throughout respiratory CT image sequences", *IEEE Transaction on Biomedical Engineering*, vol. 58, issue 1, pp. 152-158, 2011.

The material presented in Chapter 3 has been published in: A. Sadeghi Naini, G. Pierce, T. Y. Lee, R. V. Patel, A. Samani, "CT image construction of a totally deflated lung using deformable model extrapolation", *Medical Physics*, vol. 38, issue 2, pp. 872-883, 2011. G. pierce provided the 4D-CT sorting algorithm used in this research work for acquiring the input image sequence, with a brief description.

The material presented in Chapter 4 has been published in: A. Sadeghi Naini, R. V. Patel, A. Samani, "CT enhanced ultrasound image of a totally deflated lung for image-guided minimally invasive tumor ablative procedures", *IEEE Transaction on Biomedical Engineering*, vol. 57, issue 10, pp. 2627-2630, 2010.

The material presented in Chapter 5 has been peer reviewed and is currently pending revision for publication in: A. Sadeghi Naini, R. V. Patel, A. Samani, "Measurement of lung hyperelastic properties using inverse finite element approach", *IEEE Transaction on Biomedical Engineering*, 2011.

The material presented in Chapter 6 has been published in: A. Sadeghi Naini, R. V. Patel, A. Samani, "Effects of deflated lung's geometry simplifications on the biomechanical model of its tumor motion: a phantom study", *Proc. of SPIE Medical Imaging 2011: Visualization, Image-Guided Procedures, and Modeling*, Orlando, Florida, USA, vol. 7964, 79642F, 2011.

Acknowledgments

I would like to seize this opportunity to thank the people without whose support, this achievement would not be fruitful.

My first and foremost gratitude belongs to my supervisors, Dr. Abbas Samani and Dr. Rajni Patel, for their forward and continuous encouragements during my PhD studies. I would like to specialize my graceful appreciations for Dr. Samani due to his kind guidance, his precise advices, his constructive comments, in addition to his effortless contributions throughout these years. The door to his office was always open to me for exploring ideas towards practical solutions which were fruited as this thesis.

I also appreciate the time and efforts spent by members of my supervisory committee, Dr. Hanif Ladak and Dr. Ting Lee, for serving and providing beneficial suggestions in our productive group meetings.

My colleagues and friends at UWO made the PhD studies a wonderful experience for me. I'm thankful to all of them for making such friendly atmosphere available.

Finally, my deepest gratitude goes to my kind family, specially my parents for their constant supports and encouragements since my childhood. My highest grace also belongs to my wife, Zahra, who provided me with her warmest inspiration towards my achievements since we formed such a charming family. At the end I would like to present my love to my little son, Mahdiar, whose cute smiles brought me the sun in the rainy days.

Table of Contents

List of Tables

List of Figures

List of Acronyms and Abbreviations

1D	one-dimensional or one dimension
2D	two-dimensional or two dimensions
3D	three-dimensional or three dimensions
3D-CRT	Three-dimensional conformal radiotherapy
4D-CT	four-dimensional CT
AAPM	Association of Physicists in Medicine
ANN	Artificial Neural Network
ARMA	Auto-Regressive Moving Average
CSRBF	Compactly Supported Radial Basis Functions
CT	Computed Tomography
FBCT	Free Breathing CT
FE	Finite Element
FEM	Finite Element Method
FEV_1	Forced Expiratory Volume in one second
FFD	Free-Form Deformation
GPU	Graphics Processing Unit
HDR	High Dose Rate
IMRT	Intensity Modulated Radio Therapy
LDR	Low Dose Rate
LSE	Least Squares Error
MIS	Minimally Invasive Surgery
MR	Magnetic Resonance
MRI	Magnetic Resonance Imaging
NARX	Nonlinear Auto-Regressive Network
RFA	Radio-Frequency Ablation
SFEM	Statistical FEM
STD	Standard Deviation
TFI	Transfinite Interpolation
TLC	Total Lung Capacity
US	Ultrasound
VR	Virtual Reality

List of Appendices

Chapter 1

Introduction

1.1 Background and Motivation

ACCORDING to the American Cancer Society, lung cancer is the most prevalent form of cancer, with about 22,520 new cases during 2010 in the United States [1]. While being the most common form of cancer, lung cancer is often difficult to treat. As a result, lung cancer remains the leading cause of cancer death in men, and since the late 1980's it has surpassed breast cancer to become the most prevalent cause of cancer death in both men and women. Currently available treatments for lung cancer include surgery, chemotherapy, and radiation therapy. While surgical resection of cancerous lung tumors is the treatment of choice, patients who are weak or have poor pulmonary function are not deemed fit to undergo this procedure. Also, morbidity rates following resection are much higher. Chemotherapy, a possible alternative treatment, may be successful for some patients who are at early stages of the disease. However, it involves significant side effects.

1.1.1 Minimally Invasive Tumor Ablative Procedures

Minimally invasive tumor ablative procedures are newly proposed medical interventions which could be used as effective alternatives to current lung cancer treatment methods. They include cryotherapy in which the cancerous cells are killed thorough a freezing process [2, 3], Radio-Frequency Ablation (RFA) where the tumor cells' structure are

destroyed via a localized over-heating procedure [4, 5], and brachytherapy, which includes application of internal radiation sources for ablating the malignant tissue [6-10]. The application of these minimally invasive procedures in treating lung cancer is expected to have lower morbidity rates and fewer side effects, compared to the current treatment techniques.

Brachytherapy is categorized into two major classes: High Dose Rate (HDR) [6-8] or Low Dose Rate (LDR) [9, 10]. In HDR brachytherapy, higher dose radioisotopes are positioned in the patient's body temporarily where the cancerous tissue is affected by the internal radiation for a short period of time. The technique involves the insertion of numerous intra-trachea catheters under local anaesthesia based on pre-operative Computed Tomography (CT) planning. As such, HDR brachytherapy is more suitable for tumors located near airways of higher generations. LDR brachytherapy employs low dose radioisotopes that are permanently implanted in the patient's body. Such radioisotopes may consist of iodine ($_{125}$I), palladium ($_{103}$Pd) or gold ($_{193}$Au). The radioisotopes are frequently placed inside titanium shells and are called seeds. The LDR seeds emit very low radiation that is directly absorbed by the tissue surrounding the seed. Long rigid hollow needles with outer diameters of approximately 1.5 mm are often used to directly implant the radioactive seeds into malignant cancerous tissue. As such, LDR brachytherapy has been proposed for targeting lung tumors regardless of their physical location within the lung, *e.g.*, regions at the far end of the inferior lobes.

The principal issue in delivering radioactive seeds in LDR brachytherapy is accurate placement of seeds according to a distribution plan determined by medical physicists to achieve a proper radiation dosage. Small deviations in seed alignment can create significant areas of radiation over- or under-dosage [11]. Although minimally invasive LDR brachytherapy has been used in treating brain cancer [12-14] and prostate cancer [15-19], efforts to establish its clinical application for lung cancer treatment [9, 10] are ongoing and the field is in its infancy. To adapt minimally invasive brachytherapy for lung cancer therapy, a number of difficulties need to be overcome. These difficulties stem from the fact that due to its porous structure, which is associated with its millions of tiny alveoli, the lung is the most deformable organ in the body. As such, the lung undergoes

continuous large deformation during respiration. This deformation can greatly affect achieving pre-planned dosage of radiation during the operation.

1.1.2 Practical Challenges

There are two major challenges that need to be considered in developing a successful LDR lung brachytherapy system. One is the tissue deformation which stems from deflating the target lung by applying negative pressures on its corresponding trachea using an intra-trachea tube. The deflation is performed before staring the operation in order to minimize the target lung's motion during surgical procedures. Such tissue deformation causes significant differences in lung tissue geometry, size and tumor location between - pre- and intra-operative states. A consequence of these differences is that pre-operative images acquired while the lung is partially inflated become inaccurate for targeting the tumor. The other challenge is tumor motion as a result of lung tissue shift and deformation caused by needle insertion as well as respiratory contact forces. The superposition of these two motion sources determines the position of the tumor at each time step. Accurate estimation of this position is required to adjust parameters of each needle insertion (*e.g.*, needle initial orientation, insertion depth, and trigger time) to achieve the planned seed spatial distribution.

The concept of minimally invasive LDR brachytherapy involves imaging for treatment planning, localizing the tumor intra-operatively, and fusing tumor location information with real-time navigation data during the procedure. Unlike in brain brachytherapy where tissue motion is not an issue [13, 14], in lung brachytherapy, tissue deformation due to lung deflation is a major challenge that limits the effectiveness of pre-operative images significantly. Ineffectiveness of pre-operative images shifts focus to intra-operative ultrasound (US) imaging. However, unlike prostate's US images [15], US images of the deflated lung have a very poor quality. Such poor quality is due to the small amount of air remaining in the deflated lung. To address the poor quality issue of deflated lung's intra-operative US images, it is possible to register these images with high quality images obtained pre-operatively. A suitable candidate for such high quality image is pre-operative CT images. However, given that they correspond to the respiring lung with various levels of inflation, the CT images need to be processed to construct CT images

pertaining to the lung's deflated state. The constructed CT image could also be used for pre-operative tasks such as treatment planning.

The other major factor which directly impacts the accuracy of radioactive seed-implantation is tumor motion as a result of lung tissue shift and deformation caused by needle insertion and anatomical contact forces during respiration. This stems from the fact that such motion leads to significant deviations from the seed pattern specified based on radiation dosimetry. Predicting the resultant tissue shift and deformation caused by these two factors can be achieved using a tissue biomechanical modeling approach [20]. This approach often leads to utilizing the Finite Element Method (FEM) [21-23]. Such modeling requires accurate three-dimensional (3D) image of the anatomy in order to extract the geometry. Since the lung undergoing brachytherapy is in its deflated state, pre-operative images would not be useful for biomechanical modeling. Hence, to extract a realistic geometry of the anatomy during brachytherapy, a 3D image corresponding to the lung's deflated state is required. Two other essential prerequisites for biomechanical modeling of the lung include biomechanical parameters of the lung soft tissue, as well as generating the lung's finite element mesh, for which geometry simplification is inevitable.

1.2 Literature Review

As described earlier, there are two major sources of tissue motion and deformation during lung tumor ablative procedures: lung deflation at the start of the procedure, and respiratory contact forces and needle insertion during the procedure. The first leads to significant tissue deformation but occurs only once in the procedure. This complicated deformation can be estimated by processing pre-operative lung images acquired at various respiratory phases and then be modeled by an extrapolation based technique. The result can be presented as a static image *e.g.*, a CT image. The second and third sources, however, have continuous effect during the procedure leading to complex tissue motions and deformations. Prediction of such motions and deformations can be achieved by a tissue biomechanical modeling approach. Recent studies regarding the above issues are briefly reviewed in the following section.

1.2.1 Estimating Anatomical Motions and Deformations Using Image Processing Techniques

Image processing based tissue motion estimation has gained much attention among researchers in several applications. Such a motion prediction approach requires non-rigid or deformable image processing techniques as soft tissue deforms significantly under loading. Courtis and Samani proposed tissue biomechanics based multimodality image registration techniques to determine prostate tissue displacements resulting from US probe pressure [24, 25]. While reasonably accurate, these techniques are time consuming since they require performing Finite Element (FE) analysis iteratively. Archip *et al.* applied non-rigid registration techniques to align pre- and intra-procedural images of different modalities to improve targeting of liver tumors during radiofrequency ablations [26]. They also used these techniques to enhance visualization and navigation in image-guided neurosurgery [27]. Rohlfing *et al.* modeled liver motion during respiratory cycle using non-rigid registration techniques [28]. For this purpose they acquired Magnetic Resonance (MR) images of the abdomen at end-inspiration, end-expiration in addition to eight time points in between using respiratory gating. The deformation fields between the images were then computed using registration techniques, which were thus employed to model the liver motion during respiration. Global motion of the liver was modeled by a rigid transformation [29] while its local motion was modeled by a Free-Form Deformation (FFD) [30] based on B-splines. Rodríguez-Vila *et al.* applied 3D deformable registration to model the prostate motion in order to monitor radiotherapy treatment outcome in prostate cancer [31]. Guerrero *et al.* estimated Intra-thoracic lung tumor motion from breath hold CT images in normal inspiration and expiration modes [32]. They used a 3D optical flow method to calculate both the displacement of each pixel from expiration to inspiration and the reverse. The resulting displacements were then plotted in histogram format and analysed to provide insight regarding the tumor motion for use in radiation therapy. Klinder *et al.* extracted lung motion fields of seven patients in four-dimensional CT (4D-CT) inhale-exhale images using an iterative shape-constrained deformable model approach [33]. Using this approach, a continuous description of the sparse lung motion field was obtained by interpolation using thin-plate-splines [34]. A detailed motion field analysis was then performed in order to investigate

the reproducibility of breathing motion over the weeks of treatment in radiation therapy, tumor ablation, and other treatments of the thorax and upper abdomen. It was concluded from the analysis that by using patient-specific mean motion models 50-70% of the breathing motion can be captured on average which corresponds to an average estimation error of about 2.0 to 5.50 mm. McClelland *et al.* performed a similar task using a different approach [35]. For each patient, they acquired a CT volume at breath hold to be used as a reference volume. They also acquired several sequences of cine CT volumes while the patient was breathing freely (Free-Breathing CT, FBCT) together with a respiratory signal from the patient. Hence, they found correspondences between the reference volume and each of the FBCT volumes by means of non-rigid registration. A temporal fitting of the registration results was then performed to their corresponding position in the respiratory cycle. For this purpose, an approximating B-spline [36] was fitted to the data using a nonlinear least squares optimization. This enabled predicting the non-rigid transformation, and hence the position of the anatomy, at any desired position in the respiratory cycle. Tissue motion and its consequences can be detected and analysed in intra-operative images. To achieve this, Hornblower *et al.* proposed a technique for creating intra-operative, near real-time 3D US images of human lung nodules [37-39]. It was claimed that this is the world's first example of thoracoscopic 3D US imaging of a human lung nodule. However, unfortunately due to the small amount of remaining air in the deflated lung, the acquired US images had very poor quality and, as such, this intra-operative imaging modality is not deemed sufficiently reliable.

1.2.2 Modeling Motions and Deformations via Mathematical Representations and Machine Learning Techniques

Modeling anatomical motions and deformations through mathematical representations and/or machine learning approaches includes several implicit and explicit model based techniques. These methods are specifically successful in predicting (almost) periodic motions; *e.g.*, motion associated with respiration, heartbeat, *etc.* Recent studies focused on investigating such techniques for use in motion prediction in different biomedical applications. Sharp *et al.* employed several techniques to predict respiratory tumor motion in real-time image-guided radiotherapy [40]. These techniques included linear

prediction, linear extrapolation, Artificial Neural Network (ANN), and the Kalman filter. They indicated that by using tumor 3D motion prediction during a radiotherapy procedure, the root mean squared error of tumor's position localized by a realtime tumour-tracking system is improved. Borgert *et al.* derived an affine motion model to assess respiratory motion compensation for image-guided interventional procedures [41]. They acquired position data during a liver biopsy procedure from two electromagnetically tracked sensors, one placed on the patient's sternum and the other incorporated into the biopsy needle. They acquired position data of the two sensors to be used to train their model for predicting the biopsy needle position as a function of the other sensor's position. To predict respiratory motion Ernst *et al.* used wavelet-based multi-scale auto-regression techniques [42] while McCall and Jeraj employed a dual-component model [43]. The latter described the respiration motion as a non-periodic time series superimposed onto a periodic waveform. The periodic and non-periodic components of the respiration motion were modeled mathematically using a periodic Auto-Regressive Moving Average (ARMA) algorithm. Their results showed that the accuracy of the periodic ARMA model is more strongly dependent on the variations of cycle length than the amplitude of the respiration cycles. Sayeh *et al.* obtained correlation models between internal tumor position and external marker position in their Synchrony system to track respiratory motion during Robotic Radiosurgery [44]. Khamene *et al.* looked at the respiratory motion as a Markov process [45]. They established a Markov model to map and synchronize pre-operative fluoroscopic image frames with the corresponding phase from 4D-CT. The mapping procedure was formulated as an optimization process, which finds an optimal mapping maximizing the image similarity between the corresponding pairs, while preserving a temporal coherency to the established Markov model for breathing. Ramrath *et al.* predicted the respiratory motion using a multi-frequency based extended Kalman filter [46]. They developed their state-space model based on the assumption of multiple sinusoidal components contributing to respiratory motion. Recently, Kumar has used two ANN models to predict the lung tumor motion due to respiration during a lung brachytherapy procedure [47]. In his first model, he trained a Focused Time-Delay Dynamic Neural Network to predict the 3D position of any point over the lung using a sequence of its previous positions as input. His second

model, however, involved a Nonlinear Auto-Regressive Network (NARX) and used a few recent measurements of the lung volumes as the input to predict the future position of a particular point on the lung. He also integrated and evaluated his first ANN model with InterNAV [48], an image-based navigation system for needle guidance in minimally invasive procedures.

1.2.3 Biomechanical Modeling of Anatomical Motions and Deformations

Modeling soft tissue requires its biomechanical properties [49] through *ex vivo* or *in vivo* measurements. Such measurements are used to obtain tissue constitutive laws required to develop spring-mass or finite element models for real-time simulations. Samani *et al.*, O'Hagan *et al.* and Mehrabian *et al.* developed several techniques to measure soft tissue *ex vivo* and *in vivo* elastic and hyperelastic parameters [50-55]. Simone and Okamura [56] investigated needle insertion forces for bovine liver where they used a nonlinear spring model to simulate tissue stiffness. While mass-spring models are sufficiently fast, their lack of accuracy renders them inappropriate for this application. DiMaio and Salcudean [57] proposed a two-dimensional (2D) FEM to estimate force distribution along needle shaft and tissue deformation during insertion. Alteroviz *et al.* [58] presented another FE model to simulate needle insertion with application to prostate brachytherapy. For planning seed implantation in the prostate, Alteroviz *et al.* [59] proposed a planning technique, which combines numerical optimization with soft tissue mechanical simulation. These FE models require tissue needle shaft interaction parameters that need to be measured. For this purpose, Dehghan *et al.* [60, 61] proposed a measurement technique that determines these parameters. They found these parameters by systematically adjusting them such that a good fit is achieved between tissue displacements acquired by US imaging and simulated data obtained from an FE model. To investigate the mechanical behavior of human lung, Al-Mayah *et al.* developed a 3D FE model based on 4D-CT scanning of one cancer patient with a tumor in the left lung [62]. They used this FEM to model the lung motion due to breathing by including proper material properties based on experimental investigation, and by modeling contact surface interaction between the lungs and chest cavities. These techniques require FE simulation,

which suffers from low computational speed, and thus are inappropriate for real-time applications. To improve the accuracy of FE models, Bro-Nielsen introduced a condensation technique in which surface and interior nodes are decomposed and FE equations are solved on surface elements [63]. To further speed up this technique, Bro-Nielsen and Cotin [64] inverted the stiffness matrix explicitly and used a selective matrix-vector multiplication for a linearized FE model. Later Cotin *et al.* [65] developed a quasi-static pre-computed linear elastic model to compute any deformation from superposition of a set of elementary deformations of surface nodes. More recently, Mousavi *et al.* proposed a Statistical FEM (SFEM) [66]. This technique is both highly accurate and very fast so that each analysis takes less than 0.1sec on a regular desktop computer irrespective of the model's complexity.

1.3 Objectives

The objective of this work is investigating and modeling different types of motion and deformation involved in lungs undergoing minimally invasive tumor ablative procedures, such as surgery and LDR brachytherapy. As described earlier, modeling such motions and deformations are necessary for enhancing the accuracy of Minimally Invasive Surgery (MIS) in the lung. For modeling lungs in MIS, a typical MIS setup is assumed where the lung is accessed through a number of ports for imaging / visualization and surgical tools insertion and maneuvering.

The first type of major deformation involved in the target lung throughout a MIS tumor ablative procedure is the one encountered in procedures where the lung is totally deflated before starting the operation. To address the challenge associated with deflating the lung, a novel construction technique is proposed in this thesis to obtain CT image of a totally deflated lung using the lung's 4D-CT respiratory sequence acquired pre-operatively. The proposed technique which consists of a deformable registration/air volume estimation/extrapolation pipeline does not require any external marker, as it is capable of estimating the lung's air volume from the CT images automatically using a newly developed segmentation approach introduced in this thesis. To deal with the issue of poor quality of the US image, a novel registration strategy has been introduced to

enhance the quality of the lung's intra-operative US image by employing the constructed high quality CT image.

The second major deformation type of the lung tackled in this thesis is the one due to anatomical respiratory contact forces, *e.g.*, diaphragm contact forces, or due to needle insertion. This type of deformation can be characterized effectively using tissue biomechanical modeling. In addition to the deflated lung's geometry, which can be extracted from previously constructed CT image, there are two other essential prerequisites of lung's biomechanical modeling. They include biomechanical parameters of the lung soft tissue, as well as generating the lung's finite element mesh for which geometry simplification is inevitable. Measuring the lung's tissue hyperelastic properties and assessing the effects of simplifying the deflated lung's geometry on its biomechanical model's accuracy are presented in this study.

1.4 Thesis Outline

The thesis objective defined above has been presented in five separate chapters followed by a closing chapter where a thesis summary and future directions are discussed. The material presented in each chapter is outlined below.

1.4.1 Chapter 2

In Chapter 2 a technique for accurate image sequence segmentation is introduced which is based on a novel image sequence analysis. This concept is proposed to estimate the lung's air volume and its variations in respiratory CT image sequences using sequence combined histogram. The proposed method was initially validated using breath-hold CT image sequence of a lung with known lung's air volumes followed by an experiment to demonstrate the method's application in a 4D-CT respiratory sequence. The obtained results indicated a very favorable ability of the proposed technique for estimating the lung's air volume and its variations in a respiratory image sequence.

1.4.2 Chapter 3

Chapter 3 introduces a new technique for constructing CT image of a totally deflated lung using the lung's free-breathing 4D-CT image sequence acquired pre-operatively. The

proposed technique involves determining the lung tissue deformations that occur during the respiratory cycle. Each deformation is presented by means of free-form deformable registration parameters. This step is followed by formulating the obtained registration parameters as functions of the lung's air volume variations. The image construction pipeline estimates the lung's air volume automatically in each image using the technique proposed in Chapter 2; hence there is no need to use any external marker for position tracking throughout the respiratory cycle. The fitted deformation function is then used to extrapolate parameters of tissue deformation that would occur as a result of total deflation of the lung. The predicted deformation is finally used to construct a new CT image corresponding to the lung in its deflated state from one of the lung's pre-operative images that was used as a reference image. Results obtained from the experiments conducted for evaluating this technique were very encouraging, as they demonstrated the technique's capability of constructing reliable CT image of the deflated lung.

1.4.3 Chapter 4

In Chapter 4, an enhancement pipeline is proposed to improve the quality and usability of a deflated lung's intra-operative US images undergoing tumor ablative procedure. The proposed pipeline applies two concurrent and fully-automatic registration processes which do not need registration landmarks. This chapter introduces a CT enhanced US image of a totally deflated lung for the first time to complement the CT image construction technique described in Chapter 3. A number of experiments were conducted in order to validate the technique. The results indicate that the proposed technique is quite beneficial for enhancing the quality of deflated lung's intra-operative US images as it yields reasonably accurate and reliable images of lung undergoing tumor ablative procedure.

1.4.4 Chapter 5

Hyperelastic parameters of the lung's soft tissue were characterized in Chapter 5 using three different strain energy models. For this purpose and following a strict protocol for tissue resection, preparation, and indentation, several tests were performed on various fresh lung specimens using a small hemispherical ended indenter. After collecting the

indentation experimental data and in order to find the optimum hyperelastic parameters for each specimen, the force-displacement profile obtained experimentally was fitted to the one obtained from specimen specific FE model simulation. Reported results indicate successful convergences for all the three models with reasonably low average fitting errors. In order to ensure the uniqueness of the obtained results a set of independent validation tests were also performed using a considerably larger indenter tip on different indentation points within each tissue specimen. The outcomes of the validation tests demonstrated the uniqueness of the obtained parameters. As such, it can be concluded that the obtained results are convincingly reliable paving the way for more accurate and realistic modeling of the lung tissue behavior under loading.

1.4.5 Chapter 6

The influence of a deflated lung's geometry simplification on the accuracy of its tumor motion prediction is investigated in Chapter 6. In this investigation, tumor's motion was assessed by tissue biomechanical modeling. The simplification has been performed via neglecting less significant airways inside the lung. Several numerical experiments were conducted with different tumor and airway sizes and locations using both elastic and hyperelastic material models. Sensitivity of the tumor's motion prediction accuracy to the geometry simplification was then presented as a function of airways' size relative to the tumor's size. The results obtained in this study suggest that, as long as the lung's airway size does not exceed the tumor size, tumor displacement due to surface contact forces is not very sensitive to the geometry simplification. As such, it was concluded that such small airways can be omitted in the deflated lung's FE model without imposing significant error in the tumor motion estimation.

1.4.6 Chapter 7

This Chapter summarizes the material presented in chapters 2 through 6. It also suggests possible future directions for the research described in the thesis and finally concludes this dissertation.

References

[1] A. Jemal, R. Siegel, J. Xu, E. Ward, "Cancer statistics, 2010", CA. Cancer J. Clin., vol. 60, issue 5, pp. 277-300, 2010.

[2] H. Wang, P. J. Littrup, Y. Duan, Y. Zhang, H. Feng, Z. Nie, "Thoracic masses treated with percutaneous cryotherapy: initial experience with more than 200 procedures", Radiology, vol. 235, issue 1, pp. 289–298, 2005.

[3] O. Maiwand, G. Asimakopoulos, "Cryosurgery for lung cancer: clinical results and technical aspects", Technol. Cancer Res. Treat., vol. 3, pp. 143-150, 2004.

[4] M. C. Ambrogi, P. Dini, F. Melfi, A. Mussi, "Radiofrequency ablation of inoperable non-small cell lung cancer", J. Thorac Oncol., vol. 2, S2-3, 2007.

[5] T. T. Healey, D. E. Dupuy, "Radiofrequency Ablation: a safe and effective treatment in nonoperative patients with early-stage lung cancer", Cancer, vol. 17, issue 1 – pp. 33-37, 2011.

[6] J. Ricke, P. Wust, G. Wieners, S. Hengst, M. Pech, E. L. Hänninen, R. Felix, "CT-guided interstitial single fraction brachytherapy of lung tumors", Chest, vol. 127, issue 6, pp. 2237-2242, 2005.

[7] H. D. Becker, W. Harms, "Navigated bronchoscopy and endobronchial ultrasound for brachytherapy of inoperable peripheral lung cancer: a feasibility study", Chest, vol. 128, issue 4 (suppl), pp. 327S, 2005.

[8] B. O'Connor, H. Malhotra, B. Cunningham, D. Klippenstein, M. Kuettel, W. Jaggernauth, "Image-guided interstitial brachytherapy of lung tumors", Brachytherapy, vol. 5, pp. 104–105, 2006.

[9] A. L. Trejos, A. W. Lin, M. P. Pytel, R. V. Patel, R. A. Malthaner, "Robot-Assisted Minimally Invasive Brachytherapy for Lung Cancer", Telesurgery, Chap. 4, pp. 33-52, Springer Berlin Heidelberg, 2007.

[10] A. L. Trejos, A. W. Lin, M. P. Pytel, R. V. Patel, R. A. Malthaner, "Robot-assisted minimally invasive lung brachytherapy", International Journal of Medical Robotics and Computer Assisted Surgery, vol. 3, pp. 41–51, 2007.

[11] V. W. K. Ng, J. E. S. Husband, V. M. C. Nicolson, I. Minty, A. Bamias, "CT evaluation of treatment response in advanced gastric cancer". Clin Radiol, issue 3, pp. 214-220, 1996.

[12] S. Nag, E. R. Cano, D. J. Demanes, A. A. Puthawala, B. Vikram, "The American Brachytherapy Society recommendations for high–dose-rate brachytherapy for head and-neck carcinoma", Int. J. Radiat. Oncol. Biol. Phys., vol. 50, issue 5, pp. 1190-1198, 2001.

[13] R. C. Krempien, S. Daeuber, F. W. Hensley, M. Wannenmacher, W. Harms, "Image fusion of CT and MRI data enables improved target volume definition in 3D-brachytherapy treatment planning", Brachytherapy vol. 2, pp. 164–171, 2003.

[14] N. Tselis, C. Kolotas, G. Birn, S. Röddiger, I. Filipowicz, M. Kontova1, G. Fountzilas, P. Selviaridis, D. Baltas, R. Heyd, G. Anagnostopoulos, N. Zamboglou1, "CT-guided interstitial HDR brachytherapy for recurrent glioblastoma multiforme", Strahlentherapie und Onkologie, vol. 183, pp. 563-570, 2007.

[15] S. Nag, J. P. Ciezki, R. Cormack, S. Doggett, K. DeWyngaert, G. K. Edmundson, R. G. Stock, N. N. Stone, Y. Yu, M. J. Zelefsky, "Intraoperative planning and evaluation of permanent prostate brachytherapy: report of the American Brachytherapy Society", Int. J. Radiat. Oncol. Biol. Phys., vol. 51, no. 5, pp.1422–1430, 2001.

[16] G. Fichtinger, T. L. DeWeese, A. Patriciu, A. Tanacs, D. Mazilu, J. H. Anderson, K. Masamune, R. H. Taylor, D. Stoianovici, "System for robotically assisted prostate biopsy and therapy with intraoperative CT guidance", Journal of Academic Radiology, vol. 9, 2002.

[17] G. Fichtinger, E. C. Burdette, A. Tanacs, A. Patriciu, D. Mazilu, L. L. Whitcomb, D. Stoianovici, "Robotically assisted prostate brachytherapy with transrectal ultrasound guidanced–phantom experiments", Brachytherapy, vol. 5, 2006.

[18] C. Buron, B. L. Vu, J. M. Cosset, P. Pommier, D. Peiffert, M. Delannes, T. Flam, S. Guerif, N. Salem, L. Chauveinc, A. Livartowski, "Brachytherapy versus prostatectomy in localized prostate cancer: Results of a French multicenter prospective medico-economic study", Int. J. Radiat. Oncol. Biol. Phys., vol. 67, issue 3, pp. 812-822, 2007.

[19] W. S. Bice, B. R. Prestidge, S. M. Kurtzman, S. Beriwal, B. J. Moran, R. R. Patel, M. J. Rivard, "Recommendations for permanent prostate brachytherapy with ^{131}Cs: A consensus report from the Cesium Advisory Group", Brachytherapy, vol. 7, issue 4, pp. 290-296, 2008.

[20] W. Maurel, Y. Wu, N. M. Thalmann, D. Thalmann, "Biomechanical models for soft tissue simulation", Springer Berlin Heidelberg, 1998.

[21] M. Bro-Nielsen, "Finite element modeling in medical VR," J. IEEE, vol. 86, no. 3, pp. 490–503, 1998.

[22] A. Horsch, T. M. Deserno, H. Handels, H. P. Meinzer, T. Tolxdorff, "Finite element simulation of moving targets in radio therapy", Informatik aktuell, Part 12, pp. 353-357, Springer Berlin Heidelberg, 2007.

[23] A. P. Santhanam, C. Imielinska, P. Davenport, P. Kupelian, J. P. Rolland, "Modeling real-time 3-D lung deformations for medical visualization", IEEE Trans. on Inform. Tech. in Biomed., vol. 12, no. 2, 2008.

[24] P. R. Courtis, A. Samani, "Biomechanical registration of prostate images using statistical shape models" SPIE Medical Imaging, 6143 – 37, San Diego, CA, USA, 2006.

[25] P. Courtis, A. Samani, "Detecting mechanical abnormalities in prostate tissue using FE-based image registration." 10th Int. Conf. Med. Image Comput.

Comput. Assist. Interv. (MICCAI), Part 2, pp. 244-251, Brisbane, Australia, 2007.

[26] N. Archip, S Tatli, P Morrison, F. A. Jolesz, S. K. Warfield, S. G. Silverman, "Non-rigid registration of pre-procedural MR images with intra-procedural unenhanced CT images for improved targeting of tumors during liver radiofrequency ablations", 10th Int. Conf. Med. Image Comput. Comput. Assist. Interv. (MICCAI), Part 2, pp. 969-77, Brisbane, Australia, 2007.

[27] N. Archip, O. Clatz, S. Whalen, D. Kacher, A. Fedorov, A. Kot, N. Chrisochoides, F. Jolesz, A. Golby, P. M. Black, S. K. Warfieldb, "Non-rigid alignment of pre-operative MRI, fMRI, and DT-MRI with intra-operative MRI for enhanced visualization and navigation in image-guided neurosurgery", NeuroImage, vol. 35, pp. 609–624, 2007.

[28] T. Rohlfing, C.R. Maurer, W.G. O'Dell, J. Zhong, "Modeling liver motion and deformation during the respiratory cycle using intensity-based nonrigid registration of gated MR images" Med. Phys., vol. 31, no. 3, pp.427-432, 2004.

[29] J. V. Hajnal, D. L. G. Hill, D. J. Hawkes, "Medical image registration", CRC Press, Boca Raton, 2001.

[30] D. Rueckert , L. I. Sonoda , C. Hayes , D. L. G. Hill , M. O. Leach , D. J. Hawkes, "Nonrigid registration using free-form deformations: Application to breast MR images", IEEE Trans. Med. Imaging, vol. 18, no. 8, pp. 712-721, 1999.

[31] B. Rodriguez-Vila, J. Pettersson, M. Borga, F. Garcia-Vicente, E. J. Gomez, H. Knutsson, "3D deformable registration for monitoring radiotherapy treatment in prostate cancer", 15th Scandinavian conference on image analysis (SCIA'07), Aalborg, Denmark, 2007.

[32] T. Guerrero, G. Zhang, T. Huang, K. P. Lin, "Intrathoracic tumour motion estimation from CT imaging using the 3D optical flow method", Phys. Med. Biol., vol. 49, pp. 4147–4161, 2004.

[33] T. Klinder, C. Lorenz, J. V. Berg, S. Renisch, T. Blaffert, J. Ostermann, "4D-CT image-based lung motion field extraction and analysis", SPIE Medical Imaging, San Diego, California, USA, 2008.

[34] F. L. Bookstein, "Principal warps: thin-plate splines and the decomposition of deformations", IEEE Transactions on Pattern Analysis and Machine Intelligence, vol. 11, issue 6, pp. 567–585, 1989.

[35] J. R. McClelland, J. M. Blackall, S. Tarte "A continuous 4D motion model from multiple respiratory cycles for use in lung radiotherapy", Med. Phys., vol. 33, no. 9, 2006.

[36] J. R. McClelland, A. G. Chandler, J. M. Blackall, S. Ahmad, D. B. Landau, D. J. Hawkes, "4D motion models over the respiratory cycle for use in lung cancer radiotherapy planning", Proc. SPIE 5744, pp. 173–183, 2005.

[37] V. Hornblower, L. Gardi, E. W. Yu, J. J. Battista, A. Fenster, R. A. Malthaner,

"Intraoperative 3D ultrasound imaging of a lung tumour", Can. J. Surg., vol. 47(Suppl), issue 30, abstract 78, 2004.

[38] V. Hornblower, "Three-dimensional ultrasound imaging of lung tumors", M.E.Sc. dissertation, University of Western Ontario, London, Ontario, Canada, 2005.

[39] V. Hornblower, E. W. Yu, A. Fenster, J. J. Battista, R. A. Malthaner, "Performance evaluation of thoracoscopic 3D ultrasound imaging in an in vitro porcine model", Can. J. Surg., vol. 49(Suppl), issue 28, abstract 72, 2006.

[40] G. C. Sharp, S. B. Jiang, S. Shimizu, H. Shirato, "Prediction of respiratory tumour motion for real-time image-guided radiotherapy". Phys. Med. Biol., vol. 49, pp. 425–440, 2004.

[41] J. Borgert, S. Kruger, H. Timinger, J. Krücker, N. Glossop, A. Durrani, A. Viswanathan, B. J. Wood, "Respiratory motion compensation with tracked internal and external sensors during CT-guided procedures", Comput Aided Surg, vol. 11, pp. 119–125, 2006.

[42] F. Ernst, A. Schlaefer, A. Schweikard, "Prediction of respiratory motion with wavelet-based multiscale autore-gression", N. Ayache, S. Ourselin, A. Maeder (Eds.), MICCAI 2007, Brisbane, Australia, pp. 668–675, 2007.

[43] K. C. McCall, R. Jeraj, "Dual-component model of respiratory motion based on the periodic autoregressive moving average (periodic ARMA) method" Phys. Med. Biol., vol. 52, issue 12, pp. 3455-3467, 2007.

[44] S. Sayeh, J. Wang, W. T. Main, W. Kilby, C. R. Maurer, "Respiratory motion tracking for robotic radiosurgery", Treating Tumors that Move with Respiration, Section 1, Springer Berlin Heidelberg, 2007.

[45] A. Khamene, C. Schaller, J. Hornegger, "A novel image based verification method for respiratory motion management in radiation therapy", IEEE 11th Int. Conf. on Computer Vision (ICCV2007), 2007.

[46] L. Ramrath, A. Schlaefer, F. Ernst, S. Dieterich, A. Schweikard, "Prediction of respiratory motion with a multi-frequency based Extended Kalman Filter", 21st Int. Conf. Exhib. Comp. Assist. Radiol. Surg. (CARS'07), Berlin, Germany, 2007.

[47] S. Kumar, "Neural network based modelling of respiratory motion for robot-assisted lung brachytherapy," M.E.Sc. dissertation, Dept. ECE, University of Western Ontario, London, Ontario, Canada, 2007.

[48] M. P. Pytel, "The development of an image-based navigation system for use in interstitial lung brachytherapy", M.E.Sc. dissertation, University of Western Ontario, London, Ontario, Canada, 2005.

[49] Y. C. Fung, "Biomechanics: mechanics properties of living tissues", Springer, New York, 1993.

[50] A. Samani, J. Bishop, C. Luginbuhl, D. B. Plewes, "Measuring the elastic modulus of *ex vivo* small tissue samples", Phys. Med. Biol., vol. 48, pp. 2183-2198, 2003.

[51] A. Samani, D.B. Plewes, “A method to measure the hyperelastic parameters of *ex vivo* breast tissue samples” Phys. Med. Biol., vol. 49, pp. 4395-4405, 2004.

[52] A. Samani, J. Zubovits, D. B. Plewes, “Elastic Moduli of Normal and Pathological Human Breast Tissues: An Inversion-technique-based Investigation of 169 Samples” Phys. Med. Biol., vol. 52, pp. 1565-1576, 2007.

[53] J. O’Hagan, A. Samani, “Measurement of the hyperelastic properties of tissue slices with tumour inclusion”, Phys. Med. Biol., vol. 53, pp. 7087–7106, 2008.

[54] H. Mehrabian, A. Samani “Constrained hyperelastic parameters reconstruction of PVA phantom undergoing large deformation”, SPIE Medical Imaging, Orlando, FL, USA, 2009.

[55] H. Mehrabian, G. Campbell, A. Samani, “A constrained reconstruction technique of hyperelasticity parameters for breast cancer assessment”, Phys. Med. Biol., vol. 55, pp. 7489-7508, 2010.

[56] C. Simone, A. K. Okamura, “Haptic modeling of needle insertion for robot-assisted percutaneous therapy”, IEEE Inter. Conf. on Robot-assisted and Auto., pp. 2085-2091, 2002.

[57] S. P. DiMaio, S. E. Salcudean, “Needle insertion modelling and simulation”, IEEE Trans. Robot. Autom., vol. 19 (special issue on Medical Robotics), pp. 864-875, 2003.

[58] R. Alterovitz, J. Pouliot, R. Taschereau, I. C. Hsu, K. Goldberg, "Simulating needle insertion and radioactive seed implantation for prostate brachytherapy", Medicine Meets Virtual Reality 11 (MMVR11), J.D. Westwood *et al.,* (Eds.), IOS Press, pp. 19-25, 2003.

[59] R. Alterovitz, K. Goldberg, J. Pouliot, R. Taschereau, I. C. Hsu, "Sensorless planning for medical needle insertion procedures", 2003 IEEE/RSJ Int. Conf. on Intelligent Robots and Systems (IROS 2003), pp. 3337-3343, 2003.

[60] E. Dehghan, X. Wen, R. Zahiri-Azar, M. Marchal, S. E. Salcudean, "Modeling of needle-tissue interaction using ultrasound-based motion estimation", 10th Int. Conf. Med. Image Comput. Comput. Assist. Interv. (MICCAI), Brisbane, Australia, 2007.

[61] E. Dehghan, X. Wen, R. Zahiri-Azar, M. Marchal, S. E. Salcudean, “Needle-tissue interaction modeling using ultrasound-based motion estimation: phantom study” Computer Aided Surgery, vol. 13, issue 5, pp.265-280, 2008.

[62] A. Al-Mayah, J. Moseley. K. K. Brock, “Contact surface and material nonlinearity modeling of human lungs”, Phys. Med. Biol., vol. 53, pp. 305-317, 2008.

[63] M. Bro-Nielsen, “Medical image registration and surgery simulation,” Ph.D. dissertation, Dept. Math. Model., Tech. Univ. Denmark, 1997.

[64] M. Bro-Nielsen, S. Cotin, “Real-time volumetric deformable models for surgery simulation using finite elements and condensation”, Computer Graphics Forum, vol. 15, no.3, pp. 57-66, 1996.

[65] S. Cotin, H. Delingette, N. Ayache, “Real time elastic deformations of soft tissues for surgery simulation”, IEEE Transactions on Visualization and Computer Graphics, vol. 5, issue 1, pp. 62–73, 1999.

[66] S. R. Mousavi, I. Khalaji, A. Sadeghi Naini, K. Raahemifar, A. Samani, “Statistical finite element method for real-time tissue deformation estimation”, In Press, Computer Methods in Biomechanics and Biomedical Engineering, 2011.

Chapter 2

Estimating Air Volume of the Lung throughout Respiratory CT Image Sequences

The material presented in this chapter has been published in IEEE Tran. Biomed. Eng., 58(1): 152-158 (2011).[*]

2.1 Introduction

HIGH mortality rates of lung diseases [1] have encouraged many researchers to focus their efforts on improving their diagnosis and treatment methods. Many lung disease diagnosis and treatment methods involve a procedure in which respiratory image sequences are analyzed [2-9]. The image sequence may consist of several static breath-hold images [2, 3, 8] or a respiratory-gated free-breathing image sequence [4, 6, 7]. In image sequence analysis, the main emphasis is often on estimating dynamic parameters and properties of the lung such as air volume variations [2, 3, 5, 7], tissue motions [4, 6, 8], *etc.* Given that respiration is the principal function of the lung, air volume of the lung and/or its variations usually play a major role in many applications involving such analysis. For example, radiation pneumonitis [10] is one of the conditions that can be

[*]

assessed based on measuring air volume of the lung. This measurement can be done noninvasively using Computed Tomography (CT) image sequence segmentation in order to determine the extent of this disease and treat it properly to prevent radiation fibrosis. Because of the highly complex geometry of the airways and alveoli segmentation techniques using deformable models [11] or level set approach [12] are not suitable for lung's air segmentation. As such, threshold based segmentation is frequently the technique of choice for image based lung's air volume estimation. However, finding the optimum segmentation threshold for a specific application is usually a challenging task. *A priori* information such as physical density or statistical analysis such as image's histogram is usually useful to select a more appropriate threshold. For example, the intensity value which maximizes the separation between two peaks of a histogram is typically used as a rough estimation for the threshold between the corresponding segmentation classes. However, the resulting rough segmentation sometimes requires additional fine tuning steps to make the segmentation contours more accurate.

For estimating lung's air volume and/or its variations, Gamsu *et al.* estimated Total Lung Capacity (TLC) and Forced Expiratory Volume in 1 sec (FEV_1) using posteroanterior and lateral X-ray images of the chest [13]. Their estimation method consisted of manual segmentation of the lungs' X-ray images followed by a set of distance measurements and volume calculations. Later on, Kauczor *et al.* used a threshold-based technique to segment the whole lung automatically from a static helical CT image sequence acquired at deep inspiration and deep expiration in order to estimate different lung volumes including the tidal volume [2]. In their technique, the estimated volumes depended on the selected threshold. As such, various threshold values used in their segmentation technique were obtained empirically. In 2001, the same research group used a segmentation technique to estimate ventilated airspace from ^{3}He Magnetic Resonance (MR) images by applying experimentally obtained threshold values [14]. The segmentation process was followed by a manual correction step in order to exclude image artifacts and obtain the lung volume including both airspace and tissue. To obtain the air volume, they utilized an airspace-to-tissue correction ratio of 82% which was obtained empirically. This correction factor approach is ad-hoc leaving room for attempts to develop more accurate techniques of estimating ventilated lung volume. Goris *et al.*

employed segmentation techniques using experimental threshold values in order to quantitatively measure air trapping in mild cystic fibrosis using high-resolution CT image sequences acquired at inspiration and expiration [3]. Zaporozhan *et al.* also used experimental lower and upper threshold values in their image segmentation in order to quantify ventilated split-lung volumes in single-lung transplant recipients [15]. It should be noted that using empirical threshold values has limited validity which usually hampers segmentation accuracy. As such, what seems to be a major shortcoming in most of these studies is the lack of a more reliable non-empirical approach to obtain customized upper and lower segmentation threshold values for given conditions of a specific application. Furthermore, since empirical approaches for finding general upper and lower threshold values for accurate air segmentation inside the lung are often unavailable, the threshold values are frequently set to segment the whole lung including both lung tissue and air. The air volume variations in the sequence are, then, estimated by calculating the whole lung volume differences within the image sequence. In this approach, air volume of the lung in each image, however, needs to be estimated from the whole lung volume, or its corrected version using another empirical correction factor. This usually results in larger errors in both estimations of the lung's air volume and its variations throughout the sequence.

There are other applications *e.g.*, lung brachytherapy systems, where air volume of the lung and/or its variations during a respiratory sequence could be used as either a dependent [6, 7] or independent [8, 16] variable. However, in some cases due to lack of a reliable method to track the lung's air volume variations, one might prefer to use other volume change dependent variables which are easier to measure or track accurately. For example McClelland *et al.* developed a method of constructing computational lung motion models as a function of position in the respiratory cycle using four-dimensional CT (4D-CT) image sequences [4]. For this purpose, they registered Free-Breathing CT (FBCT) images acquired during a few respiratory cycles with a high quality breath-hold CT image. Next, using an optimization technique, they formulated each registration parameter as a function of position in the respiratory cycle. To identify the position of each FBCT image in the respiratory cycle, they used either the location of external skin surface or three-dimensional (3D) coordinates of a reflective marker attached to the

patient's chest tracked with a tracking system. Although the reflective marker method improved their respiratory signal accuracy, it still involved some errors. As a more general alternative that does not require any marker or tracking system, Sadeghi Naini *et al.* proposed a novel method to construct the CT image of a totally deflated lung based on its partially inflated images [8]. Such CT image is potentially very useful in performing tumor ablative procedures such as Low Dose Rate (LDR) brachytherapy [17] for treating lung cancer. In LDR lung brachytherapy which involves direct and permanent placement of radioactive seeds into malignant tumors, the target lung is almost completely deflated initially in order to minimize the tumor motion during the intervention. As such the pre-operative CT images will no longer represent the physical domain of the lung and hence would not be reliable during the surgery. The proposed CT construction method involved Free-Form Deformation (FFD) registration [18] where each parameter was formulated as a function of the lung's air volume. Registration parameters corresponding to the totally deflated lung were then determined using extrapolation. A key for applying the extrapolation technique in conjunction with a free-breathing 4D-CT imaging protocol was having an effective technique for estimating air volume of the lung and its variations. This has been the main motivation behind this research. More details on the proposed technique for constructing CT image of the totally deflated lung can be found in chapter 3.

In this chapter, a technique for accurate image sequence segmentation is introduced based on a novel image sequence analysis. As described in Section 2.2, this concept is proposed to estimate air volume of the lung and its variations in respiratory CT image sequences using sequence combined histogram. The proposed method was initially validated using breath-hold CT image sequence of *ex vivo* porcine left lung with known lung's air volumes followed by an *ex vivo* lung experiment to demonstrate the method's application in a 4D-CT respiratory sequence. The conducted experiments and their results are presented in Section 2.3. As discussed and concluded in Section 2.4, the results indicate a very favorable ability of the proposed technique for estimating air volume of the lung and its variations in a respiratory image sequence.

2.2 Method

2.2.1 Segmentation of Lung Image Sequences

Image segmentation plays a major role in many applications of biomedical imaging such as diagnosis, localization of pathology [19], treatment planning [20], computer aided surgery [21], quantification of tissue volumes [22], partial volume correction of functional imaging data [23], and study of anatomical structure [24]. An effective yet simple segmentation technique is thresholding in which finding and fine tuning the threshold values is the most important step. The proposed method for estimating air volume of the lung is based on a novel image sequence segmentation technique that determines the threshold values systematically. The concept behind this technique takes advantage of the fact that the segmentation classes of background air, lung's air and soft tissue appear in all images in the sequence, though with variable shape and size. The technique employs such variations in conjunction with air mass conservation and tissue incompressibility principles to find the best segmentation thresholds for a variable class throughout the sequence. The segmentation problem in this context is formulated as an optimization problem to find the optimal points that satisfy the mass conservation and incompressibility principles.

2.2.1.1 Initial Guess for Lower and Upper Thresholds

To avoid uniqueness issues in the segmentation optimization problem, an initial guess close enough to the solution is necessary. Figure 2.1 shows a typical combined histogram of a lung image sequence. This histogram can be obtained by overlaying the histograms of all images in the sequence. As seen in this figure, the combined histogram is characterized by having two nodes, $I_1=A$ and $I_2=B$, in the middle region where the histograms converge together, *i.e.* the distances between them reach a minimum. We argue that the histogram regions before point A, between points A and B and after point B correspond to the background air volume (free air), lung's air volume (free air surrounded by soft tissue), and soft tissue volume, respectively. In other words, nodes A and B correspond to good initial estimates of the lower and upper threshold values of the lung's air, respectively.

In the *ex vivo* experiments conducted in this study, voxels with image intensity corresponding to convergence point *A* were displayed. It was observed that those voxels correspond mainly to the outlines of the lung and bronchi. This is quite justified as tissue partial volume effect starts to kick in at the interface regions between air and lung tissue including the lung boundary and bronchi. This implies that CT numbers up to point *A* correspond to the background air which has the smallest CT numbers within the field of view. Note that a sequence of respiratory histograms always converges to a point *A*, and this point represents the tissue-air interface regions for the following reason. The surface variation of such tissue interface regions during respiration is negligible compared to the corresponding volume variation of air inside the lung. Therefore, the convergence point *A*, which corresponds to minimal number of voxels variation *w.r.t.* volume variation during respiration, is the best point that represents the interface regions. After point *A*, intensity values will correspond to air mixed with small amount of alveoli tissue. This continues until a point *B* where the lung tissue starts to be dominant with small amount of air. As such, each histogram curve between points *A* and *B* provides a good approximation to the lung's air volume. We argue that point *B*, the second convergence point in the combined histogram, is a good initial guess for the upper threshold. This is based on tissue incompressibility or near incompressibility of the soft tissue phase of the lung. As seen in Figure 2.1, the histograms almost coincide starting from point *B*. Given that volume of the lung's soft tissue is proportional to the area underneath that part of the histogram, we conclude that tissue incompressibility can be approximately satisfied if the lung tissue corresponds to the region of histogram starting from point *B* and continuing to the end.

2.2.1.2 Optimization Formulation

While the convergence points $I_1=A$ and $I_2=B$ provide good estimates of the segmentation lower and upper threshold values, these estimates can still be improved by seeking new values that best satisfy air mass conservation and tissue incompressibility constraints. This concept was formulated as an optimization problem. To satisfy air mass conservation during respiration, one mathematical constraint can be derived from the fact that a reduction in the volume of the background air (proportional to the area underneath

each histogram up to the sought lower threshold point $I_1=\alpha$) must lead to equal increase in the volume of air in the lung (proportional to the area underneath each histogram between the sought lower and upper threshold points $I_1=\alpha$ and $I_2=\beta$) and vice versa. This can be described mathematically as follows:

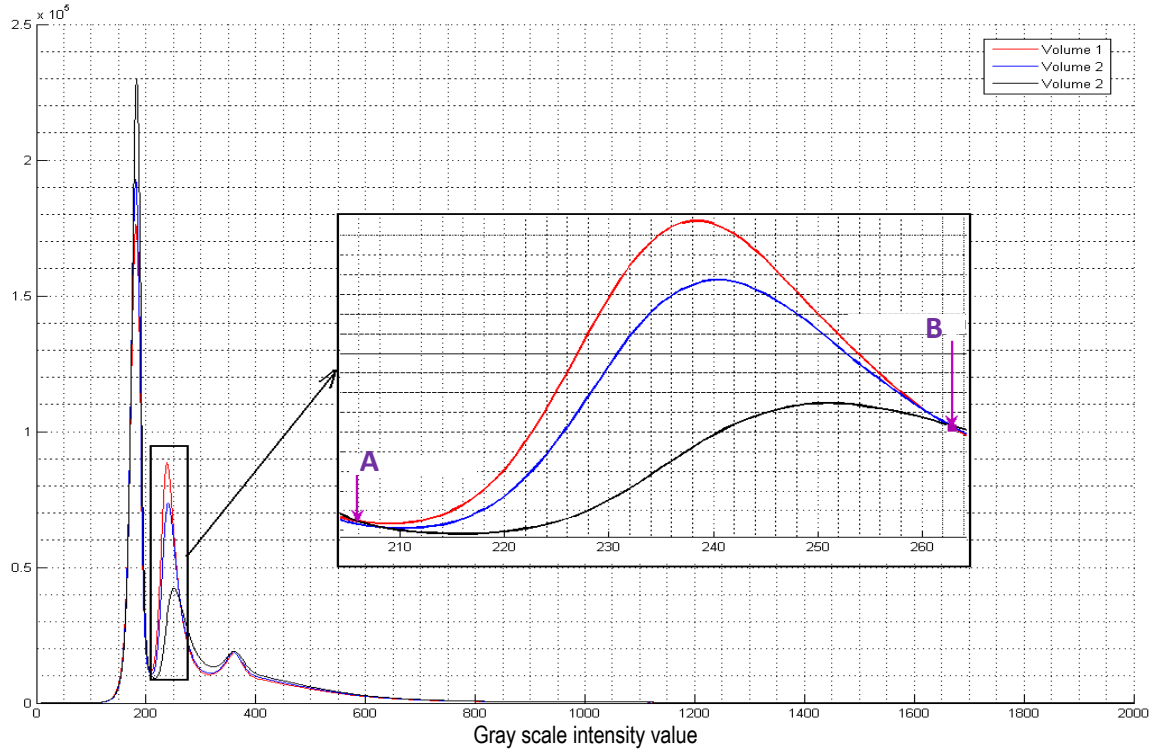

Figure 2.1: Combined sequence histogram for a respiratory sequence consisted of three static breath-hold CT images acquired at 700, 600, and 320 ml, respectively. The figure has been zoomed in to focus on the region of interest within the original combined histogram; the convergence points are indicated by arrows.

$$\sum_{j=1}^{n-1}\left[\int_{0}^{\alpha}\{H_{j+1}(I)-H_j(I)\}dI-\int_{\alpha}^{\beta}\{H_j(I)-H_{j+1}(I)\}dI\right]\simeq 0 \qquad (2.1)$$

Where H_{j+1} and H_j represent two consecutive histograms and n is the number of histograms in the sequence. Equation 2.1 requires that the entire lung volume is located inside the field of view of the image. The other constraint can be derived based on the incompressibility of the lung's soft tissue phase noting that the histogram portions after

point *B* are close to each other but not identical. This can be demonstrated mathematically as below:

$$\sum_{j=1}^{n-1} \int_{\beta}^{I_{max}} \{H_{j+1}(I) - H_j(I)\}^2 dI \simeq 0 \tag{2.2}$$

Where I_{max} is the maximum intensity seen in the histograms. As such, using a positive weight factor, ω, we derive a cost function which combines the two constraints and seek two parameters $I_1=\alpha$ and $I_2=\beta$ that minimizes it as follows:

$$\begin{aligned} \text{Minimize } C(I_1, I_2) \\ = \sum_{j=1}^{n-1} [\int_{0}^{I_1} \{H_{j+1}(I) - H_j(I)\} dI - \int_{I_1}^{I_2} \{H_j(I) - H_{j+1}(I)\} dI] \\ + \omega \sum_{j=1}^{n-1} \int_{I_2}^{I_{max}} \{H_{j+1}(I) - H_j(I)\}^2 dI \end{aligned} \tag{2.3}$$

2.2.2 Air Volume Estimation Framework

Figure 2.2 shows a block diagram of the proposed method for estimating air volume of the lung and its variations in a respiratory CT image sequence. As described in the previous sections, initial guesses of the lower and upper threshold values can be extracted from the sequence's combined histogram.

The framework starts with the input block where the whole image sequence is input. In the first step, histograms of all images within the sequence are calculated separately. These histograms are then passed to the second block where they are overlaid in order to form the sequence's combined histogram. After smoothing the histogram curves in order to remove high frequency noise-like variations, the convergence points *A* and *B* in the sequence's combined histogram are extracted in the next block as described earlier. For this purpose, standard deviation of all the histograms within the sequence is calculated for each intensity value. Consequently, the converging areas are searched for the points with a minimum standard deviation which are selected as the convergence points *A* and *B***.** The

convergence points are then used in the next block as initial guesses of the optimization algorithm where the optimized lower and upper thresholds α and β are calculated based on Eq. 3. Given that lower and upper segmentation thresholds have integer values in the image space, the optimization process can be simply performed by a two dimensional brute-force search in the integer space and within a large enough neighbourhood of the initial guesses obtained previously. In the next step, after segmentation is performed using the determined threshold values in the fifth block, the sixth block counts the voxels segmented as the lung's air for each image separately. In the last block, the air volume of the lung is calculated for each image by multiplying the number of voxels counted as the air by the voxel size. This block also calculates the air volume variations within the sequence by subtracting air volumes of the lung between successive images. The experiments conducted to validate this approach are presented in the next section.

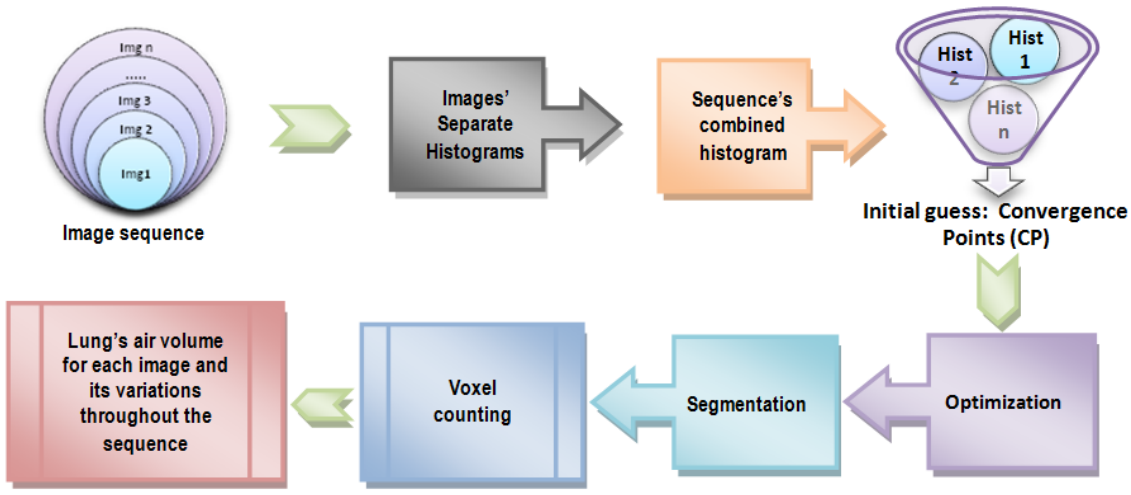

Figure 2.2: Block diagram of the framework proposed to estimate air volume of the lung and its variations in a respiratory CT image sequence.

2.3 Experiments and Results

Two sets of *ex vivo* experiments were conducted on porcine left lungs in order to validate the proposed technique in static breath-hold CT and free-breathing 4D-CT respiratory sequences, respectively. The first experiment was conducted using a number of static breath-hold CT images from a respiratory sequence, acquired while air volume of the lung was controlled and known in each image. The second experiment, however, was

performed to generalize the idea by employing it to a 4D-CT respiratory sequence where air volume of the lung was unknown in each image.

In the first experiment, a lung obtained from an adult ~80 kg pig was inflated using an intra-trachea tube and a North American Drager Narkomed 2A ventilator machine. The air volume inside the lung was controlled by the ventilator. Micro-CT imaging was performed using a GE Locus Ultra scanner. Prior to each breath-hold lung ventilation, residual air was sucked out of the lung to ensure that the residual air volume is negligible**.** The static breath-hold CT images of the lung were acquired at volumes of 700 ml, 600 ml, and 320 ml, respectively. The final images size was (228×186×324) voxels with a voxel size of (0.62^3) mm^3. These three 3D images were fed into the air volume estimation framework as the respiratory image sequence. Figure 2.1 shows the combined sequence histogram obtained for these images. In this figure, the second hill belongs to the lung's air voxels in different images. The convergence points A and B at the beginning and the end of this hill are indicated by arrows. As mentioned before, these points represent an approximation for the lower and upper thresholds in the lung's air segmentation process. Figure 2.3 demonstrates the objective function surface for different lower and upper threshold values of I_1 and I_2 calculated according to Equation 2.3 with an optimal ω value of 1. The minimum point (α, β) found by the optimization algorithm has been indicated by the shown arrow. This point corresponds to segmentation thresholds which are close to the convergence points.

The resultant segmented images are displayed using MicroView open source software (GE Healthcare). Figure 2.4 demonstrates one middle slice of the CT images acquired at different volumes where the air inside the lung is segmented using the obtained threshold values. Air volumes of the lung calculated based on the performed segmentation using the thresholds obtained from the optimization algorithm are given in Table 2.1. This table also includes the comparative results from the maximum separation method where the threshold values were calculated based on maximum separation between two histogram peaks. Following this method, each image histogram was analyzed separately and the intensity values in the middle of distance between the lung's air peak and its preceding (background air) and successive (soft tissue) peaks were selected as the lower and upper

segmentation thresholds, respectively. The table indicates that the air volume estimation errors corresponding to the threshold values obtained from our optimization technique range from 3% to 4.1%, which is very low. However, the estimation errors corresponding to the maximum peak separation thresholding is high where they become even higher while approaching the least inflated phases.

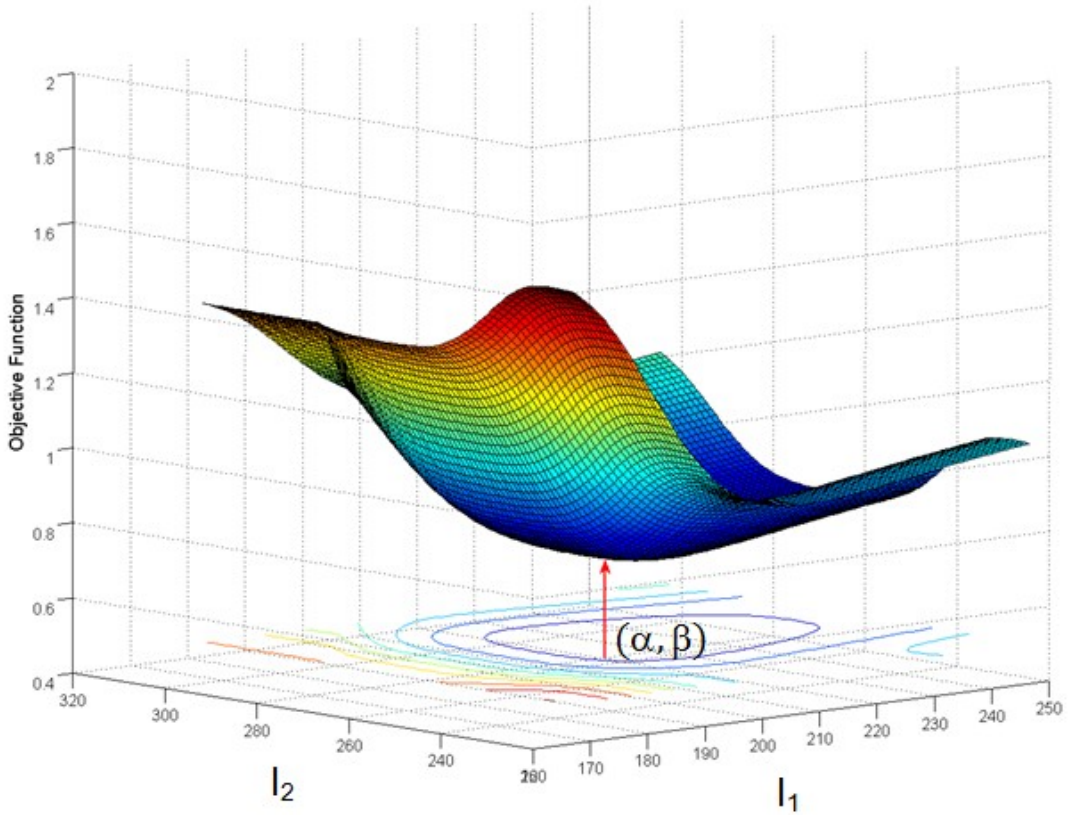

Figure 2.3: Objective function surface for different lower and upper threshold values of I_1 and I_2 in the combined histogram shown in Fig. 1. The minimum point has been indicated by the arrow.

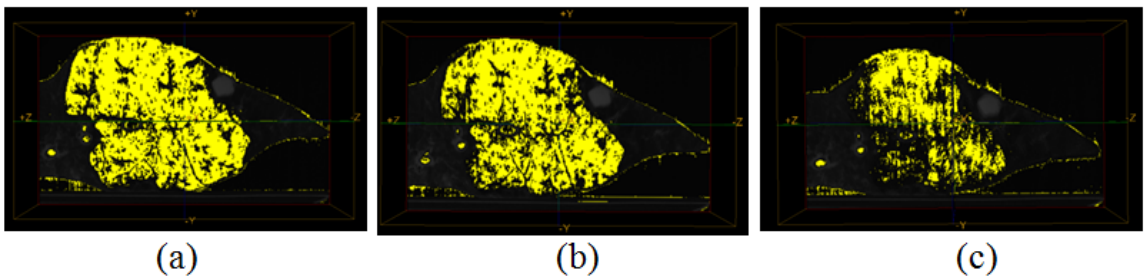

Figure 2.4: One middle slice of the static breath-hold CT images acquired at: (a) 700 ml, (b) 600 ml, (c) 320 ml; the air inside the lung is segmented using the lower and upper threshold values extracted from the sequence's combined histogram. The bright and dark regions show the air and soft tissue with the background, respectively.

Table 2.1: Results of estimated lung's air volumes in the static breath-hold respiratory CT sequence using two different techniques to extract the segmentation thresholds from the histograms.

Image #	Lung's air volume	Convergence points		Maximum peak separation	
		Estimated lungs' air volume	Error	Estimated lungs' air volume	Error
1	700 ml	679 ml	3.0%	839 ml	19.8%
2	600 ml	576 ml	4.0%	740 ml	23.3%
3	320 ml	333ml	4.1%	540 ml	68.7%

The second experiment was conducted on a free-breathing 4D-CT sequence [25] acquired while the lung was being respired using an intra-trachea tube and a ventilator with a respiration frequency of 10 Breath/Min. the lung used in this experiment was obtained from a young ~20 kg pig. The 4D-CT sequence consisted of sixteen 3D images with an equal number of images during inhalation and exhalation phases and a voxel size of $(0.33\times0.33\times0.625)$ mm^3 in all the images. Eight successive images from the whole sequence were then fed into the segmentation framework as the input sequence. Figure 2.5 shows the combined sequence histogram for these 8 images. In this figure, the hill bounded by the vertical solid lines corresponds to the lung's air voxels where the convergence points are shown by the arrows. In the combined sequence's histogram, the lung's air volume variations have clear correlation with the variations in the hill's height. Figure 2.6 illustrates the objective function surface corresponds to the combined histogram shown in Figure 2.5 where the minimum point found by the optimization algorithm has been indicated by the shown arrow. This point again corresponds to segmentation thresholds which are close to the convergence points as anticipated.

Figure 2.7 demonstrates one middle slice of each CT image acquired while the lung was continuously being respired. The air inside the lung was segmented using the threshold values corresponding to the minimum point of the objective function given in Figure 2.6. The estimated air volumes of the lung corresponding to the image sequence were (a) 234 ml, (b) 222 ml, (c) 207 ml, (d) 185 ml, (e) 159 ml, (f) 132 ml, (g) 127 ml, (h) 116 ml, respectively. The gradual air volume variation inside the lung can be noticed in this sequence, which is consistent with the gradual variation in the combined sequence

histogram. The obtained results were validated by evaluating their consistency with the tissue near incompressibility principle. For this purpose, the whole lung contours were segmented in each phase throughout the sequence using a more complicated region growing algorithm followed by a manual correction step. The lung's air volume estimated previously by the proposed technique was then subtracted from the resulting whole lung volume obtained for each phase. The volumes obtained as such represent the soft tissue volumes in different phases which should be similar according to tissue near incompressibility principle. Obtained results are given in Table 2.2. As the table suggests, estimation results for air volume of the lung confirms the soft tissue near incompressibility. The maximum variation of the estimated soft tissue volume did not exceed 14 ml (3.6%) which is reasonably low. This further supports the accuracy of the proposed technique for estimating air volume of the lung throughout a respiratory sequence.

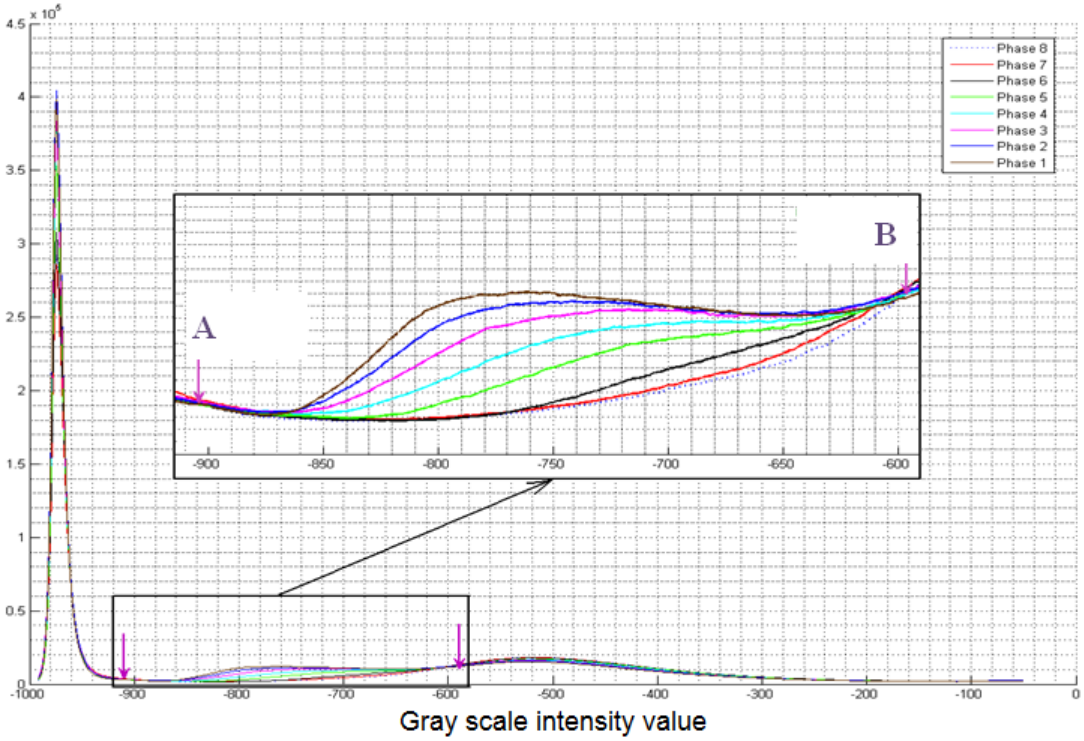

Figure 2.5: Combined sequence histogram for the eight CT images from a full 4D-CT respiratory sequence acquired while the lung was being respired continuously. The figure has been zoomed in to focus on the region of interest within the original combined histogram; the convergence points are indicated by arrows.

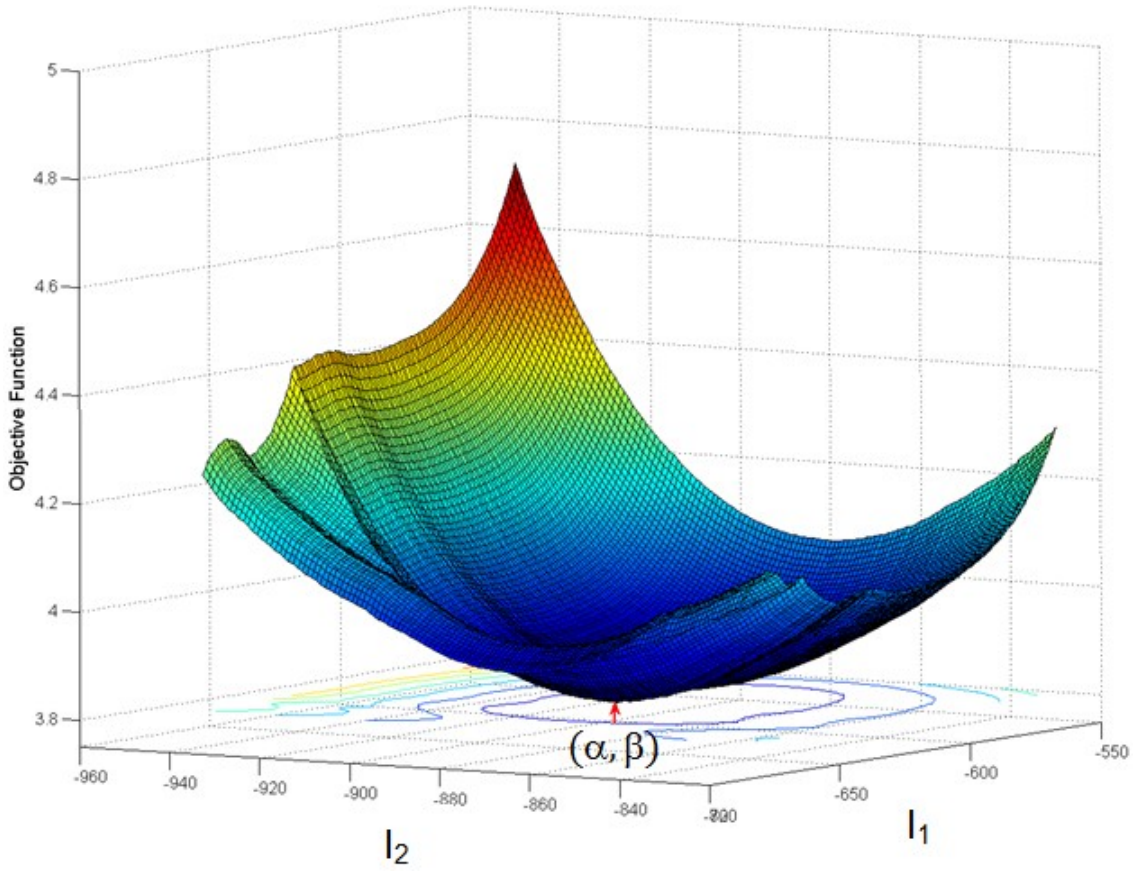

Figure 2.6: Objective function surface for different lower and upper threshold values of I_1 and I_2 in the combined histogram shown in Fig. 5. The minimum point has been indicated by the arrow.

2.4 Discussion and Conclusions

In this chapter, a novel concept of image sequence analysis was introduced in order to obtain appropriate lower and upper threshold bounds for threshold-based image segmentation. This concept is equally useful for segmenting both static and dynamic image sequences. In this research, the concept was utilized to estimate air volume of the lung and its variations in respiratory CT image sequences using combined sequence histogram and satisfying lung's air mass conservation as well as tissue incompressibility principles.

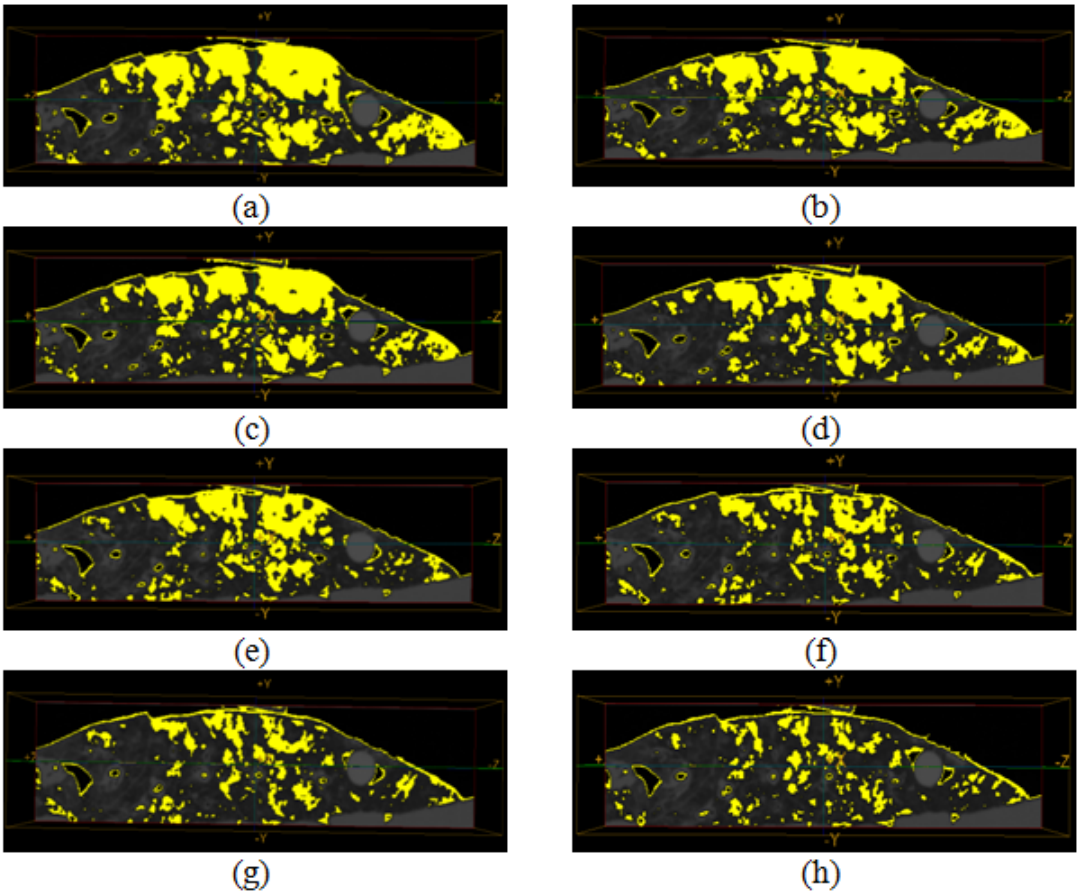

Figure 2.7: One middle slice of the eight CT images from a full 4D-CT respiratory sequence acquired while the lung was being respired continuously; the air inside the lung is segmented using the lower and upper threshold values extracted from the sequence's hidden information. The estimated air volumes calculated based on the segmentations are: (a) 234 ml, (b) 222 ml, (c) 207 ml, (d) 185 ml, (e) 159 ml, (f) 132 ml, (g) 127 ml, (h) 116 ml, respectively.

Table 2.2: Results of the estimated air volume of the lung and their corresponding tissue volumes in the 4D-CT respiratory sequence. Each tissue volume was estimated by subtraction of the estimated air volume of the lung from the whole lung volume. The maximum variation of estimated tissue volume in comparison with all other phases is also given for each phase.

Phase	Whole lung volume	Estimated lung's air volume	Estimated tissue volume	Maximum variation in estimated tissue volume in comparison with all other phases
a	619 ml	234 ml	385 ml	3.6%
b	609 ml	222 ml	387 ml	3.1%
c	596 ml	207 ml	389 ml	2.6%
d	578 ml	185 ml	393 ml	1.5%
e	555 ml	159 ml	396 ml	2.8%
f	530 ml	132 ml	398 ml	3.3%
g	526 ml	127 ml	399 ml	3.5%
h	514 ml	116 ml	398 ml	3.3%

Ex vivo experiments were conducted on porcine left lungs in order to demonstrate the effectiveness of the segmentation method developed based on this concept. The proposed method was initially validated using a breath-hold CT image sequence with known lung air volumes. The obtained results indicated a very good ability of the method for estimating air volume of the lung and its variations throughout a respiratory image sequence. A comparison between the two sets of obtained results shows that the proposed optimization thresholding technique outperforms the maximum peak separation thresholding when used in lung's air volume estimation. We hypothesize that one reason for such a substantial difference, specially in the less inflated phases, is the following. Partial volume effect in which a voxel of the lung's image involves both air and tissue is a major source of error in the segmentation process. In the maximum peak separation technique where information pertaining to a single histogram is used to extract the segmentation threshold, the influence of partial volume cannot be considered affectively. Neglecting this influence hampers the estimation of lung's air volume more significantly in less inflated phases since, most likely, more weights correspond to the tissue portion in a typical partial volume situation. The proposed technique, which benefits from a sequence combined histogram where the patterns of variations are available for all the involving histograms, can take into the account the effect of partial volume more effectively according to its foundations discussed in the Methods.

The proposed method was also applied to a 4D-CT respiratory sequence where air volumes of the lung were unknown. Given the similarity of the imaging modality, protocol and animal model compared to the first experiment, it is expected that the results obtained from this experiment have similar accuracy. Consistency of the obtained results in the latter experiment with the tissue near incompressibility principle was also validated as the lung tissue volume results showed little variations over the respirations cycle.

Considering its favorable capabilities, this technique can be used effectively in clinical applications such as LDR lung brachytherapy where the air volume of the lung and/or its variations in a respiratory sequence are needed as described in Section 2.1. The concept of finding the optimum segmentation threshold values from an image sequence's combined histogram introduced in this work can also be used in other biomedical

applications where important physiological parameters need to be extracted. An example of such applications is estimation of the ventricle's ejection fraction from sequential cardiac images [26]. Here, the proposed technique can be applied in order to find the optimum lower and upper thresholds for an effective segmentation of the ventricle's blood volume followed by a calculation of the ventricle's blood volume variations throughout the end- diastole – end-systole image sequence. This automatic method may improve or even substitute existing complex semi-automatic algorithms [27] or empirical threshold-based methods [28] currently used for ejection fraction estimation.

References

[1] American Lung Association, "2008 press releases", available at http://www.lungusa.org/press-room/press-releases/2008-press-releases/index.jsp?page=4, 2008.

[2] H. U. Kauczor, C. P. Heussel, B. Fisher, R. Klamm, P. Mildenberger, M. Thelen, "Assessment of lung volumes using helical CT at inspiration and expiration: comparison with pulmonary function tests", AJR, vol. 171, pp.1091-1095, 1998.

[3] M. L. Goris, H. J. Zhu, F. Blankenberg, *et al.*, "An automated approach to quantitative air trapping measurements in mild cystic fibrosis", Chest, vol. 123, pp. 1655-1663, 2003.

[4] J. R. McClelland, J. M. Blackall, S. Tarte, F. Chan, T. E. Robinson, "A continuous 4D motion model from multiple respiratory cycles for use in lung radiotherapy", Med. Phys., vol. 33, pp. 3348-58, 2006.

[5] A. J. Swift, N. Woodhouse, S. Fichele, J. Siedel, G. H. Mills, E. J. Van Beek, J. M. Wild, "Rapid lung volumetry using ultrafast dynamic magnetic resonance imaging during forced vital capacity maneuver: correlation with spirometry", Invest Radiol., vol. 42(1), pp. 37-41, 2007.

[6] J. M. Reinhardt, K. Ding, K. Cao, *et al.*, "Registration-based estimates of local lung tissue expansion compared to xenon CT measures of specific ventilation", Med. Image Anal., vol. 12, pp. 752-763, 2008.

[7] G. Li, N. C. Arora, H. Xie, G. E. Christensen, E. A. Hoffman, S. V. Bodas, "Quantitative prediction of respiratory tidal volume based on the external torso volume change: a potential volumetric surrogate", Phys. Med. Biol., vol. 54, pp. 1963–1978, 2009.

[8] A. Sadeghi Naini, R. V. Patel, A. Samani, "CT image construction of the lung in a totally deflated mode", Proc. of the 2009 IEEE International Symposium on Biomedical Imaging: From Nano to Macro (ISBI 2009), Boston, Massachusetts, USA, pp. 578-581, June 2009.

[9] T. Zhang, H. Keller, R. Jeraj, R. Manon, J. Welsh, R. Patel, J. Fenwick, M. Mehta, T. R. Mackie, B. Paliwal, "Breathing synchronized delivery - a new technique for radiation treatment of the targets with respiratory motion", International Journal of Radiation OncologyBiologyPhysics, vol. 57 (2), pp. S185-S186, 2003.

[10] G. Rodrigues, M.l Lock, D. D'Souza, E. Yu, J. Van Dyk, "Prediction of radiation pneumonitis by dose-volume histogram parameters in lung cancer--a systematic review", Radiotherapy and Oncology, Volume 71 (2), pp. 127-138, 2004.

[11] M. Kass, A. Witkin, D. Terzopoulos, "Snakes: active contour models", International Journal of Computer Vision 321-331, 1988.

[12] R. Malladi, J. Sethian, B. Vemuri, "Shape modeling with front propagation: A

level set approach", IEEE Transactions on Pattern Analysis and Machine Intelligence, vol. 17, pp. 158-175, 1995.

[13] G. Gamsu, D. M. Shames, J. McMahon, R. H. Greenspan, "Radiographically determined lung volumes at full inspiration and during dynamic forced expiration in normal subjects", Invest Radiol, vol. 10, pp. 100-108, 1975.

[14] H. U. Kauczor, K. Markstaller, M. Puderbach, J. Lill, B. Eberle, G. Hanisch, T. Grossmann, C. P. Heussel, W. Schreiber, M. Thelen, "Volumetry of ventilated airspaces by 3He MRI. Preliminary results", Invest Radiol, vol. 36, pp. 110-114, 2001.

[15] J. Zaporozhan, K. K. Gast, S. Ley, J. Schmiedeskamp, A. Biedermann, B. Eberle, H. U. Kauczor, "Functional analysis in single lung transplant recipients. A comparative study of high resolution CT, 3He MRI, and pulmonary function tests", Chest, vol. 125, pp. 173-181, 2004.

[16] W. Lu, P. J. Parikh, I. M. El Naqa, M. M. Nystrom, J. P. Hubenschmidt, S. H. Wahab, S. Mutic, A. K. Singh, G. E. Christensen, J. D. Bradley, D. A. Low, "Quantitation of the reconstruction quality of a four-dimensional computed tomography process for lung cancer patients", Med. Phys., vol. 32 (4), pp. 890-901, 2005.

[17] A. W. Lin, A. L. Trejos, R. V. Patel, R. A. Malthaner, "Robot-Assisted Minimally Invasive Brachytherapy for Lung Cancer", Telesurgery, Chap. 4, pp. 33-52, Springer Berlin Heidelberg, 2007.

[18] D. Ruckert, L. I. Sonoda, C. Hayes, D. L. G. Hill , M. O. Leach , D. J. Hawkes, "Nonrigid registration using free-form deformations: Application to breast MR images", IEEE Trans. Med. Imaging, vol. 18, no. 8, pp. 712-721, 1999.

[19] A. P. Zijdenbos, B. M. Dawant, "Brain segmentation and white matter lesion detection in MR images", Critical Reviews in Biomedical Engineering, vol. 22, pp.401-465, 1994.

[20] E. Rietzel, G. T. Chen, N. C. Choi, C. G. Willet, "Four-dimensional image-based treatment planning: Target volume segmentation and dose calculation in the presence of respiratory motion", Int. J. Radiat. Oncol., Biol., Phys. vol. 61 (5), pp. 1535–1550, 2005.

[21] L. Soler, H. Delingette, G. Malandain, J. Montagnat, N. Ayache, C. Koehl, O. Dourthe, B. Malassagne, M. Smith, D. Mutter, J. Marescaux, "Fully automatic anatomical, pathological, and functional segmentation from CT scans for hepatic surgery", Computer Aided Surgery, vol. 6 (3), pp. 131-142, 2001.

[22] S. M. Larie, S. S. Abukmeil, "Brain abnormality in schizophrenia: a systematic and quantitative review of volumetric magnetic resonance imaging studies", J. Psychiatry, vol. 172, pp. 110–120, 1998.

[23] H. W. Muller-Gartner, J. M. Links, J. L. Prince, R. N. Bryan, E. Mcveigh, J. P. Leal, C. Davatzikos, J. Frost, "Measurement of radiotracer concentration in brain gray matter using positron emission tomography: MRI-based correction for partial volume effects", J. Cereb. Blood Flow Metab., vol. 12, pp. 571–583,

1992.

[24] P. A. Yushkevich, P. Piven, H. C. Hazlett, R. G. Smith, S. Ho, J. C. Gee, G. Gerig, "User-guided 3D active contour segmentation of anatomical structures: significantly improved efficiency and reliability", Neuroimage, vol. 31 (3), pp. 1116-1128, 2006.

[25] G. Carnes, S. Gaede, E. Yu, J. Van Dyk, J. Battista, T. Y. Lee, "A fully automated non-external marker 4D-CT sorting algorithm using a serial cine scanning protocol", Phys. Med. Biol., vol. 54, pp. 2049–2066, 2009.

[26] M. S. Krishnam, A. Tomasian, M. Iv, S. G. Ruehm, R. Saleh, C. Panknin, J. G. Goldin, "Left ventricular ejection fraction using 64-slice CT coronary angiography and a new evaluation software: initial experience", Br .J. Radiol., vol. 81, pp. 450-455, 2008.

[27] W. Sun, M. Çetin, R. Chan, V. Reddy, G. Holmvang, V. Chandar, A. Willsky, "Segmenting and tracking the left ventricle by learning the dynamics in cardiac images", Inf. Process. Med. Imag. (IPMI), pp. 553–565, 2005.

[28] K. U. Juergens, H. Seifarth, F. Range, S. Wienbeck, M. Wenker, W. Heindel, R. Fischbach, "Automated threshold-based 3D segmentation versus short-axis planimetry for assessment of global left ventricular function with dual-source MDCT", AJR, vol. 190, pp. 308–314, 2008.

Chapter 3

CT Image Construction of a Totally Deflated Lung Using Deformable Model Extrapolation

The material presented in this chapter has been published in Med. Phys., 38(2): 872-883 (2011).[*]

3.1 Introduction

ONE major challenge described earlier in clinical implementation of lung tumor ablative procedures, such as Low Dose Rate (LDR) brachytherapy, is tissue deformation which causes significant differences in lung tissue geometry, size and tumor location between - pre- and intra-operative states. This deformation stems from deflating the target lung in order to minimize its motion during surgical procedures. This chapter addresses the challenges associated with deflating the lung in such procedures. For this purpose, a novel technique is proposed to construct Computed Tomography (CT) images of the lung in a totally deflated mode from the inflated lung's CT images obtained pre-operatively. Our method uses pre-operative CT images of partially inflated lung at a number of phases during respiration to construct images of the deflated lung. The image

[*]

construction process involves a registration-extrapolation pipeline to predict the deflation motion of the lung tissue. The predicted motion is then applied to the lung's pre-operative CT image, called reference image, to construct an image of the deflated lung.

A preliminary study of this approach was presented by Sadeghi Naini *et al.* [1, 2]. As described there, the preliminary experiments were conducted using a few number of static breath-hold CT images of a porcine lung acquired at different phases of respiration. The images were acquired while the volume of the lung was controlled by the ventilator at each phase. These images were then used for constructing the CT image of the totally deflated lung. Results obtained from that study was encouraging. While sufficient as proof of principle, the study involved a few pre-operative images which, in most clinical cases, are not sufficient for accurate construction of the totally deflated lung's CT image. Acquiring a substantially larger number of pre-operative CT images using breath-hold static protocol also did not seem practical, specially in clinical applications as the protocol is not straightforward enough to implement and is not convenient for lung disease patients. This encouraged us to switch the CT imaging protocol to a free-breathing four-dimensional CT (4D-CT) protocol [3] in which acquiring a large number of pre-operative CT images of the partially inflated lung is feasible while it is more convenient for lung cancer patients. Our proposed CT image construction technique requires a set of partially inflated lung images corresponding to known air volumes. However, with 4D-CT there is no control mechanism over the lung's inhaled air volume while free-breathing images are acquired; hence the lung's air volumes corresponding to the acquired images are unknown. As such, in order to apply the extrapolation technique in conjunction with the free-breathing 4D-CT imaging protocol, an effective technique for estimating the lung's air volume and its variations is a paramount necessity. For this purpose we developed a novel technique for estimating the lung's air volume throughout respiratory image sequences which is presented in Chapter 2. Applying this technique makes the image construction process possible without the need for any external marker for tracking position of 4D-CT images within a respiratory cycle.

This chapter is organized as follows. In the next section, after describing preliminaries, the method used to construct the CT image of the lung in a totally deflated mode is

introduced. Conducted experiments as well as obtained results are then presented in sections 3.3 and 3.4, respectively. Finally obtained results are discussed and the chapter is concluded in section 3.5

3.2 Method

3.2.1 Image Registration

In image registration, a one-to-one mapping or transformation is determined between the coordinates of one image space to those in the other. In rigid registration the transformation is limited to translation and rotation while in affine registration the transformation may also include scaling and shearing. Equation 3.1 shows the general form of three-dimensional (3D) affine transformation. In this equation T_{Shear}, T_{Scale}, and T_{Rigid} are 4×4 matrices and the a_{ij} parameters are coefficients related to rotation, scaling and shearing, while the t parameters determine translation [4].

$$T_{affine}(x,y,z)=\begin{bmatrix}x'\\y'\\z'\\1\end{bmatrix}=T_{shear}.T_{scale}.T_{rigid}.\begin{bmatrix}x\\y\\z\\1\end{bmatrix}=\begin{bmatrix}a_{11}&a_{12}&a_{13}&t_x\\a_{21}&a_{22}&a_{23}&t_y\\a_{31}&a_{32}&a_{33}&t_z\\0&0&0&1\end{bmatrix}.\begin{bmatrix}x\\y\\z\\1\end{bmatrix} \quad (3.1)$$

While rigid and affine registration are suitable for modeling global motion, they are not capable of modeling local motion which usually occurs in deformable objects such as soft tissue. To model the local motion, non-rigid or deformable registration approaches have been developed.

3.2.2 Free-Form Deformation

A Free-Form Deformation (FFD) technique was introduced by Ruckert *et al.* for registering breast Magnetic Resonance (MR) images [5]. Later, this FFD technique and its modified versions were widely used in other applications of non-rigid image registration by several research groups [6-9]. FFD models the global and local deformations within the object separately, and then combines them to form an overall smooth deformation. In practice this translates into a global transformation followed by a local transformation:

$$T(x,y,z) = T_{local}(T_{global}(x,y,z)) \tag{3.2}$$

where T_{global} is a rigid or affine transformation and T_{local} is a deformation model based on B-splines [10].

A modified implementation of the FFD is used in this chapter as the non-rigid registration technique in the construction pipeline described in Section 3.2.4. Following the original version of the FFD, let Φ denote an $n_x \times n_y \times n_z$ size mesh of control points ($\phi_{i,j,k}$) with a uniform spacing δ_d in direction d. Also suppose that $\varphi_{i,j,k}$ denotes the displacement of the corresponding control point. Hence, the local transformation can be formulated as a 3D tensor product of one-dimensional (1D) cubic B-splines:

$$T_{local}(x,y,z) = (x,y,z) + \sum_{l=0}^{3}\sum_{m=0}^{3}\sum_{n=0}^{3} B_l(u)B_m(v)B_n(w)\,\varphi_{i+l,j+m,k+n} \tag{3.3}$$

where

$$i = \left\lfloor \frac{x}{\delta_x} \right\rfloor - 1,\ j = \left\lfloor \frac{y}{\delta_y} \right\rfloor - 1,\ k = \left\lfloor \frac{z}{\delta_z} \right\rfloor - 1,\ u = \frac{x}{\delta_x} - \left\lfloor \frac{x}{\delta_x} \right\rfloor,\ v = \frac{y}{\delta_y} - \left\lfloor \frac{y}{\delta_y} \right\rfloor,\ w = \frac{z}{\delta_z} - \left\lfloor \frac{z}{\delta_z} \right\rfloor,$$

and the *B(.)*'s represent the basis functions of B-spline:

$$\begin{aligned} B_0(u) &= \frac{(1-u)^3}{6} \\ B_1(u) &= \frac{(3u^3 + 6u^2 + 4)}{6} \\ B_2(u) &= \frac{(-3u^3 + 3u^2 + 3\mathrm{u} + 1)}{6} \\ B_3(u) &= \frac{u^3}{6} \end{aligned} \tag{3.4}$$

As such, the algorithm uses an optimization technique to find the optimum displacements of the control points that yield the best registration in some sense (*e.g.*, maximum

similarity). Considering Equation 3.3, the derivative of the deformation field with respect to the B-spline coefficients can be given by:

$$\frac{\partial T_{local}(x,y,z)}{\partial \varphi_{i,j,k}} = B_l(u)B_m(v)B_n(w) \tag{3.5}$$

where $l = i - \left\lfloor \frac{x}{\delta_x} \right\rfloor + 1,\ m = j - \left\lfloor \frac{y}{\delta_y} \right\rfloor + 1,\ n = k - \left\lfloor \frac{z}{\delta_z} \right\rfloor + 1$,

and $B_l(u) = 0$ for $l < 0$ and $l > 3$

This implies that the derivative term is nonzero only in the neighbourhood of the corresponding control point. Having such a derivative equation for the transformation, the optimization part of the registration process can be implemented efficiently using an iterative gradient descent or other derivative-based optimization techniques.

3.2.3 Extrapolation

In the CT construction technique proposed in this chapter, a correspondence is made between the lung's tissue deformation parameters and its air volume variation. Corresponding values of the tissue deformation parameters are thus required when the lung undergoes complete deflation. Extrapolation is the technique of choice for this purpose. Generally, for a set of discrete points' data extrapolation, a curve is initially fitted to the data points and the resulting curve is used to predict points outside the interval covered by the data points. In polynomial extrapolation the aim is finding a polynomial to be used to determine the function value outside the data interval. The polynomial of an order m has the following general form:

$$y = a_0 + a_1 x + a_2 x^2 + \ldots + a_m x^m \tag{3.6}$$

If the number of known data points is equal to *m*, the polynomial passes through all data points, whereas if the number of known data points is greater than *m*, fitting a polynomial with a minimal average distance to the set of known data points involves an optimization process. The latter leads to a more reliable polynomial particularly when extrapolation is involved. As such, high order polynomial extrapolation must be used with due care as it

restricts the generalization ability of the extrapolation curve. An error estimate of the extrapolated value grows with the degree of the polynomial extrapolation. This is well known as Runge's phenomenon [11, 12].

3.2.4 CT Construction Pipeline

The hypothesis of the proposed image construction technique is that if the lung's tissue deformations are extracted throughout a respiratory image sequence and fitted as functions of the lung's air volume, the fitted deformation could be extrapolated in order to estimate the deformation the lung tissue would undergo when its air content is sucked out completely as a result of negative pressure on the corresponding bronchi. The extrapolated deformation can then be applied to a reference pre-operative image to construct the required lung's image in a totally deflated mode.

Figure 3.1 shows the proposed approach scheme for lung CT image construction in its totally deflated state. The input is pre-operative CT images of the lung at different volumes corresponding to respiratory cycle, which are fed into the pipeline. The pre-operative images are passed through two different branches simultaneously: 1) Registration branch (right), 2) Segmentation branch (underneath). The first branch is implemented based on the FFD method. It non-rigidly registers one of the pre-operative CT images of the lung acquired at a reference volume to each pre-operative lung CT image. This process is performed in two separate blocks. In the first block, an optimization process finds the best rigid and affine transform parameters, which align the reference image with each lung CT image. These parameters are then passed to the second block as the global registration parameters. The second block is used for finding the local transformation parameters of the deformable registration. In order to avoid being trapped in local minima during optimization, in addition to avoid unrealistic folding deformations, this block involves a multi-resolution hierarchical scheme starting with a coarse control point lattice. The second branch estimates the lung's air volume in each image based on the segmentation technique described in Chapter 2.

The final registration parameters from the first branch as well as the lung's air volume from the second branch are then fed to the extrapolation block for all images. This

extrapolation block, thus, determines the parameters required to construct the CT image of the lung in its deflated state. The extrapolation is performed by, first, finding a relationship between each registration parameter and the lung's air volume through a curve fitting process. Thus, the obtained curves are extrapolated to estimate the required registration parameters. Finally, in the last block, the extrapolated parameters are used in conjunction with the lung's image acquired at the reference volume to construct the required lung's CT image in its totally deflated state.

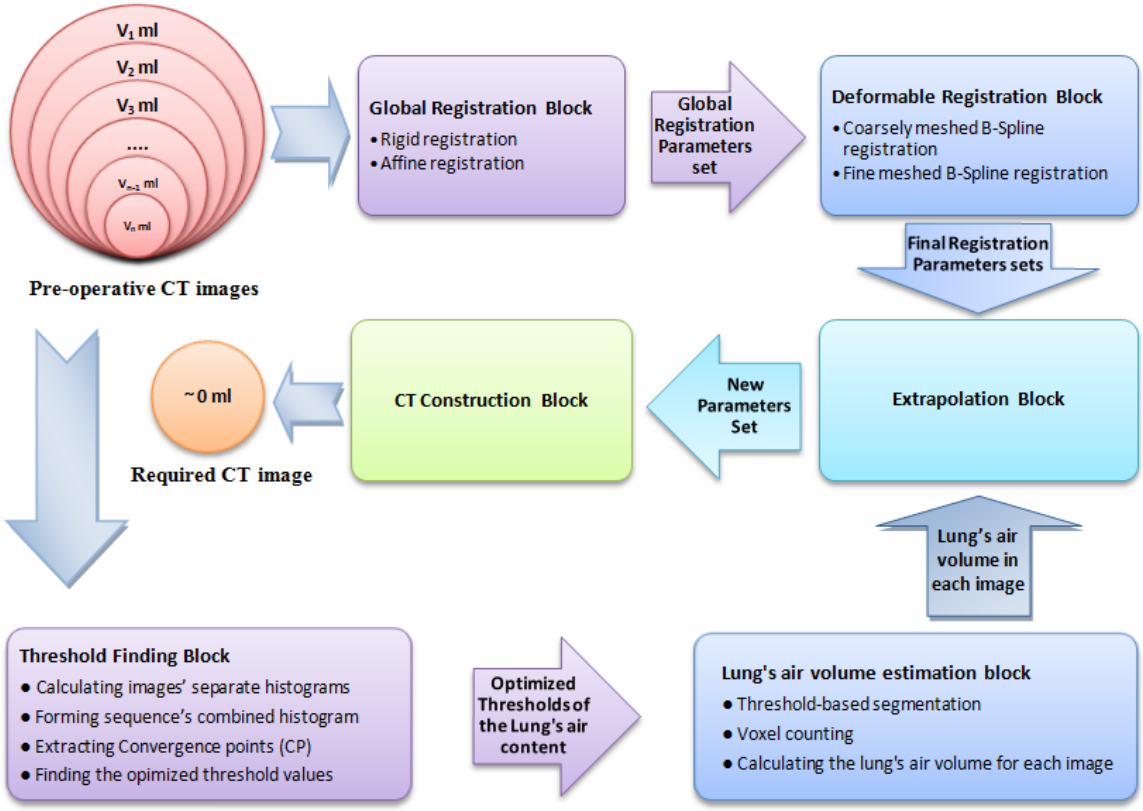

Figure 3.1: CT image construction pipeline. Input: pre-operative images; the right branch performs registration: 1st and 2nd block find the deformable registration's global and local transformation parameters to register a lung reference image with each pre-operative lung image; the branch underneath estimates the lung's air volume: 1st block finds the optimum lower and upper thresholds to segment the lung's air content while the 2nd block uses these thresholds to estimate the lung's air volume in each image. The extrapolation block extrapolates these parameters and passes them to the next block where the required image is constructed using the extrapolated parameters and the lung's CT image acquired at the reference volume. Output: Lung image in a totally deflated state.

3.3 Experiments

The constructed CT image of the lung in its totally deflated state is expected to be a sufficiently good representative of the almost completely deflated target lung. In order to evaluate the performance of the proposed technique, *ex vivo* experiments were conducted on a porcine lung. A number of phantom tumors were sutured inside a porcine left lung. The tumors were constructed of gelatin and agar in addition to ~3 mg/ml iodine CT contrast agent such that they had a Hounsfield Unit of ~200 HU. After tumor suturing, the lung was respired using an intra-trachea tube and a mechanical ventilator with a respiration frequency of 12 Breath/Minute and a respiration ratio of 50/50. In order to avoid sudden deflation of the lung in the beginning of exhalation, a compliant resistor was used in the exhaust tube of the ventilator. The resistor mimicked the role of the thorax in an *in vivo* experiment and helped maintaining a relatively smoother motion during exhalation. This allowed enough time for acquiring a sufficient number of CT images at different lung volumes during the 4D-CT data acquisition process.

All scans were performed using a GE Healthcare Discovery CT 750 HD scanner (Waukesha, WI). A series of 4.0 cm axial field of view sequential adjacent cine scans were performed. Each cine scan lasted for 6 seconds. The CT scanning parameters were: 80 kVp, 200 mA and a gantry rotation period of 0.4 s. Each cine scan was retrospectively reconstructed to 32 x 1.25 mm slices and a field of view of 22 cm. Adjacent cine scans were overlapped by 2 slices to provide the spatial link required for the 4D-CT sorting program.

The 4D-CT images were produced using a 4D-CT sorting method described in [3]. This involved producing coherent volumes by beginning with a starting cine scan position, taken from one of the middle cine scan positions. The starting scan position time series was divided into 20 time point volumes. The procedure for matching a full volume to the starting scan is the same for each time point and is described for one time point. Using one of the overlapping scan positions between the starting scan position and the adjacent cine scan position, an image matching algorithm was performed. The image matching algorithm searches the entire adjacent scan position time series for a match. Once the best match is found, it was added to the starting scan position and used to find

the match from the next adjacent cine scan position. This was continued in both the inferior and superior directions until an image from each scanned position was added to the volume.

Following the 4D-CT image acquisition, the lung was totally deflated and a static helical CT image was acquired for the purpose of validation. After cropping the region of interest from the original CT images, all the 4D and static CT images had a final image size of (411×211×274) voxels with a voxel size of (0.43×0.43×1.25) mm^3. The images are displayed in Figure 3.2 using ParaView open source software (Kitware, Inc.). Figure 3.2(a)-(t), and (w) each show an image slice crossing through a tumor corresponding to 4D-CT images of the lung acquired at different volumes, and the static CT image of the lung acquired in a totally deflated state, respectively.

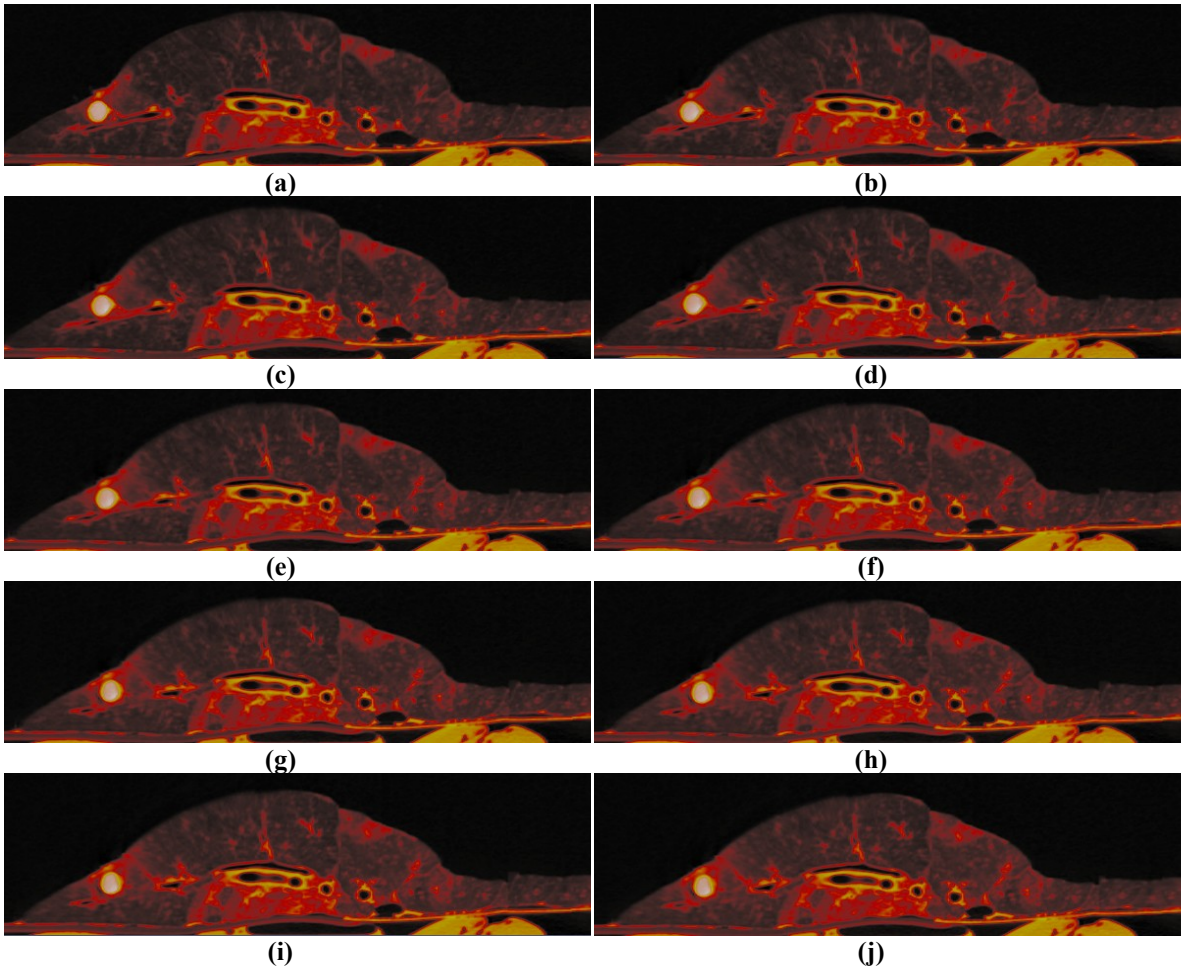

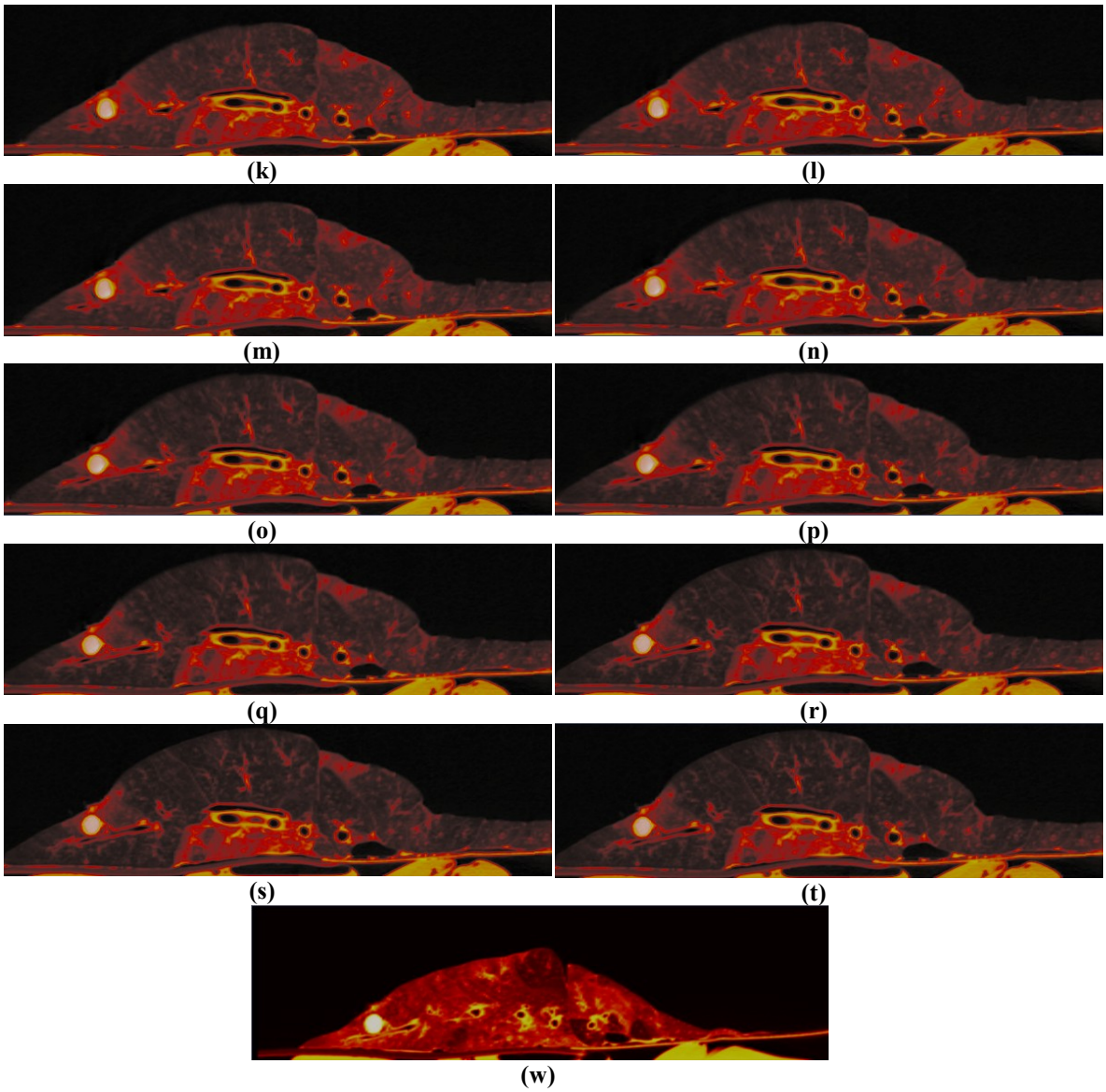

Figure 3.2: (a) - (t): Pre-operative free-breathing 4D-CT image sequence of a lung slice passing through a tumor acquired while the lung was being respired continuously; w: the same lung slice acquired while the lung was totally deflated (required).

To find the best subset of the pre-operative images to be used in the CT image construction pipeline, several numerical experiments were conducted. The experiments involved using subsets of the 4D-CT images corresponding to the exhalation, inhalation, in addition to sets of the smallest 3, 4, and 5 lung's air volumes. Finally, the complete set of the pre-operative 4D-CT images was also used. Results of deflated lung's CT image construction using a subset of the pre-operative 4D-CT images are given in section 3.4. The best construction results were obtained when the whole set of 4D-CT images was

used. Consequently, all of the twenty 4D-CT images were fed into the CT image construction pipeline as the pre-operative images. The CT image of the lung acquired at the most inflated phase (Figure 3.2 (t)) was selected as the reference image. Hence, each lung deformation field throughout the respiratory CT image sequence was estimated based on this reference image. The reason for selecting the image corresponding to the most inflated phase as the reference image was that selecting any other CT image would have led to a bidirectional motion (deflation/inflation) throughout the respiratory sequence, whereas choosing the lung image at the most inflated state yielded a one-directional motion (deflation). As such, this choice is expected to lead to less complex registration parameter variation leading to more accurate curve fitting and extrapolation process. Normalized Mutual information was employed as the similarity measure in all of registration blocks within the pipeline [13]. To avoid getting trapped in local minima, the applied image construction pipeline involved multi resolution hierarchical deformable registration block consisting of (8^3) and (28^3) nodes, respectively.

Several numerical experiments were conducted in order to obtain the best fitting equation to describe the relationship between the registration parameters and the lung's air variations. These experiments involved using 1^{st} to 5^{th} order linear and logarithmic scaled polynomials, as well as 1^{st} to 3^{rd} order B-spline extrapolations in order to obtain the most accurate registration parameter set required to construct the CT image of the deflated lung. It was observed that increasing the complexity of the fitting curve by using B-spline equations or by increasing the order of the fitting curve equation results in over-fitting leading to substantial unrealistic artifacts in the constructed CT image and rendering it highly inaccurate.

Among the tested fitting functions, a first order logarithmic polynomial (Equation 3.7) led to the highest accuracy, hence it was chosen to extrapolate each registration parameter in the lung in its deflated state. An important reason of the suitability of a logarithmic function for describing the lung's volume variations was that tissue deformation rate was higher at smaller volume values approaching the deflated state. Such variations can be best described by the following function:

$$Parameter = a_0 + a_1.\log(V) \tag{3.7}$$

In Equation 3.7, V denotes the volume of the lung's air estimated using the segmentation technique and log is the natural logarithm. While the extrapolation appears to use a simple linear function, it should be emphasized that it is presented using a logarithmic scale, hence it is actually nonlinear. Moreover, FFD registration typically involves several thousands of parameters, each of which describes the displacement of a local node in one direction only. Consequently, the ensemble of the extrapolated FFD registration parameters using Equation 3.7 is quite capable of representing highly complex tissue deformation expected in the lung while reaching full deflation state.

3.4 Results

Figure 3.3 shows the combined image sequence histogram obtained for 4D-CT images acquired at 20 phases of the porcine lung respiratory cycle. In this figure the second hill (also zoomed in), where the convergence points are also shown, corresponds to the lung's air voxels in different images. The lung's air volume variations have clear correlation with the variations in the hill's height. The optimal lower and upper threshold values determined using the technique described in Chapter 2 are shown by arrows in the figure.

Figure 3.4 (a)-(t) each shows a tumor passing slice from the lung's 4D-CT respiratory image sequence where the air inside the lung is segmented using the obtained threshold values. These images have been displayed using MicroView open source software (GE Healthcare). The lung's air volumes corresponding to the respiratory image sequence were estimated at (a) 920 ml, (b) 826 ml, (c) 782 ml, (d) 714 ml, (e) 642 ml, (f) 573 ml, (g) 501 ml, (h) 441 ml, (i) 436 ml, (j) 359 ml, (k) 347 ml, (l) 375 ml, (m) 445 ml, (n) 532 ml, (o) 728 ml, (p) 802 ml, (q) 878 ml, (r) 949 ml, (s) 982 ml, (t) 989 ml, respectively. The gradual air volume variation inside the lung is evident in this sequence. This is consistent with the gradual variation seen in the combined sequence histogram.

As described in section 3.2, the registration branch function detects the local tissue deformations throughout the respiratory image sequence and represents it with respect to a reference image selected from the images of the sequence. Since the CT image of the

lung acquired at the most inflated phase (end-inhalation) is selected as the reference image in this experiment, the largest relative motion takes place in the image corresponding to the least inflated phase (end-exhalation). Figure 3.5 shows the evaluation result obtained from registration of the reference image (Fig. 3.2 (t)) with the image acquired at the least inflated phase (Fig. 3.2 (l)). In this figure, the difference of these two images is demonstrated before and after the non-rigid registration process, respectively. In the difference of these two images before the registration process, the anatomy, boundaries and the tumors from two images are clearly visible. This implies significant misalignment. However, after the deformable registration, the difference image shows very little structure, especially at the tumor area. As such, the obtained registration results confirm a successful process of local motion detection throughout the respiratory cycle. As Figure 3.1 indicates, the registration parameters obtained from all images in the respiratory sequence along with the estimated lung's air volume in each image were then passed to the extrapolation block.

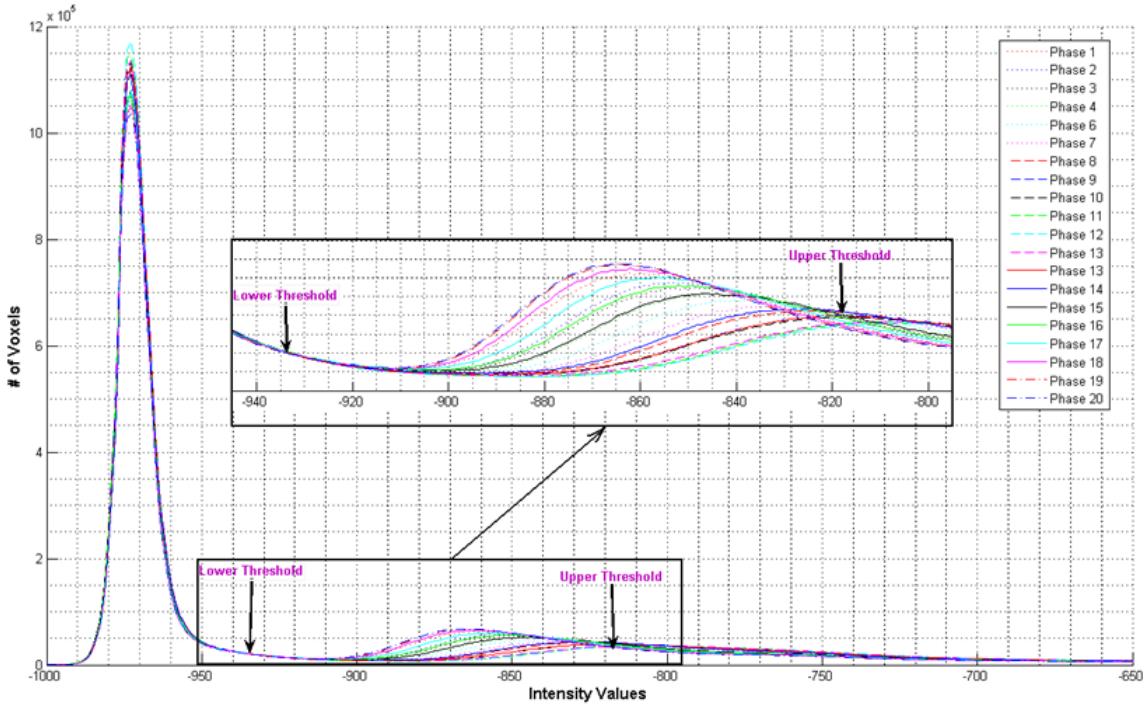

Figure 3.3: Combined sequence histogram for the twenty CT images of a 4D-CT respiratory sequence acquired while the lung was being respired continuously. The region of interest (black rectangle) has been zoomed in; optimal lower and upper segmentation thresholds are indicated by two arrows

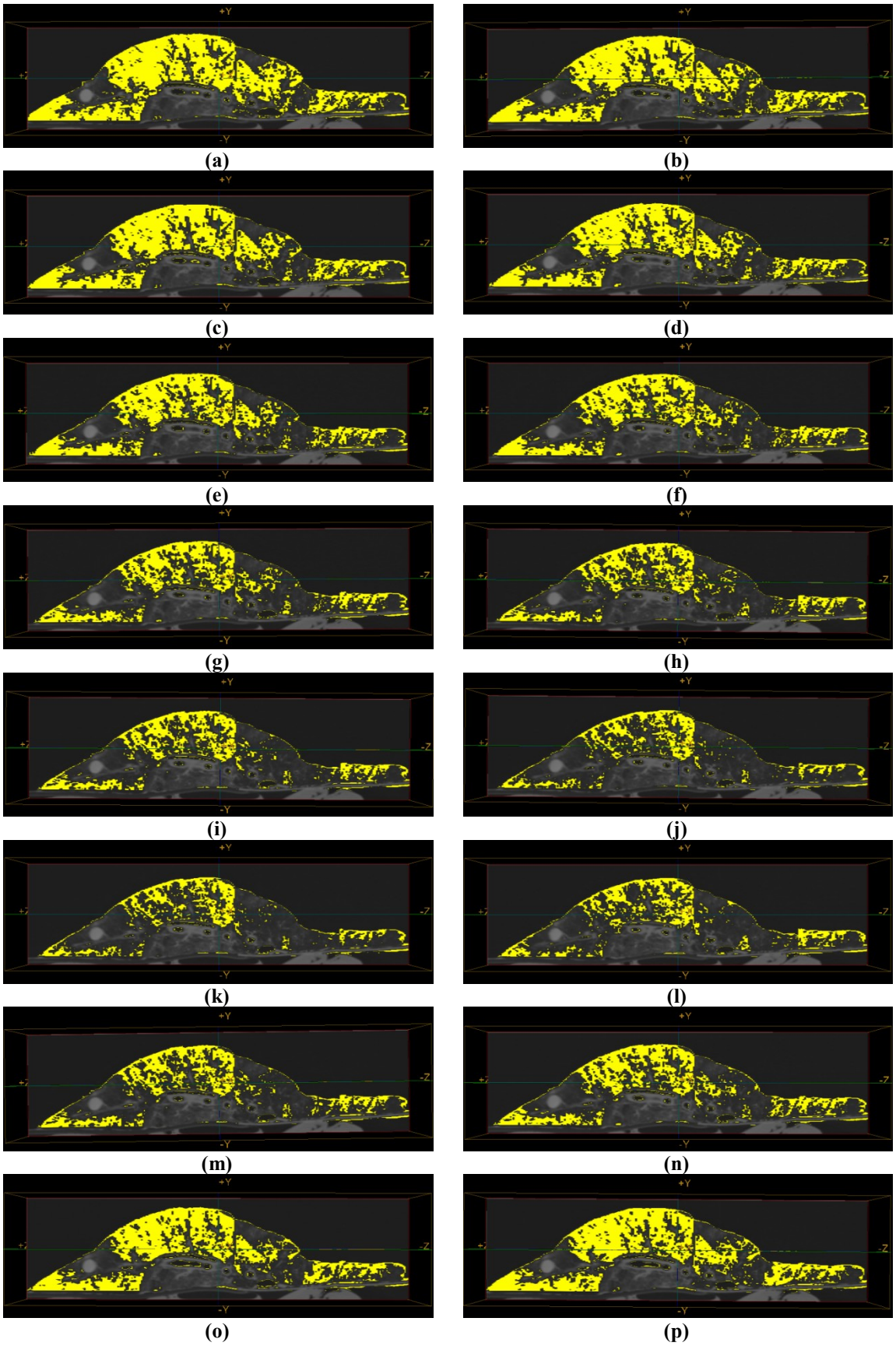

(a) (b)

(c) (d)

(e) (f)

(g) (h)

(i) (j)

(k) (l)

(m) (n)

(o) (p)

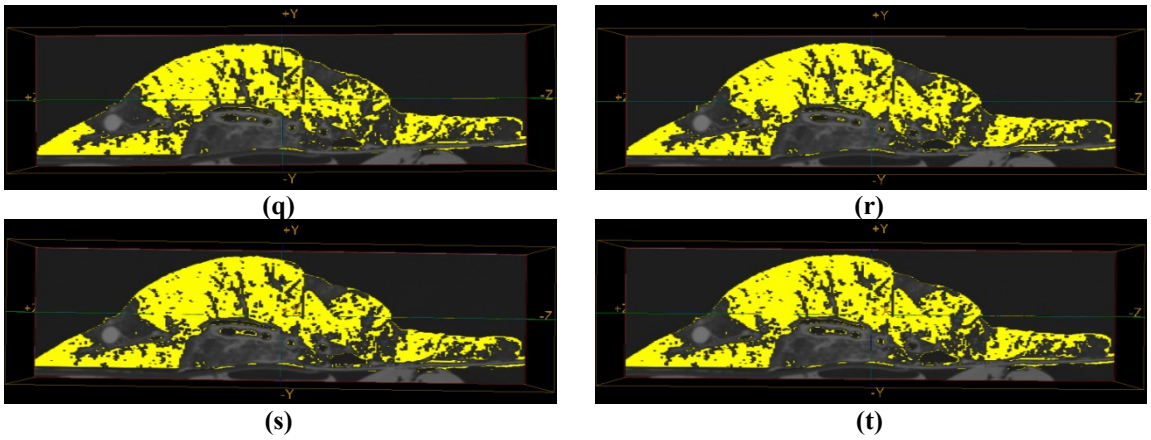

Figure 3.4: (a) - (t): One lung image slice passing through a tumor from the respiratory 4D-CT image sequence acquired while the lung was being respired continuously; The air inside the lung was segmented using the determined optimal lower and upper threshold values. The bright and dark regions show the air and soft tissue with the background, respectively. The estimated air volumes calculated based on the segmentations are: (a) 920 ml, (b) 826 ml, (c) 782 ml, (d) 714 ml, (e) 642 ml, (f) 573 ml, (g) 501 ml, (h) 441 ml, (i) 436 ml, (j) 359 ml, (k) 347 ml, (l) 375 ml, (m) 445 ml, (n) 532 ml, (o) 728 ml, (p) 802 ml, (q) 878 ml, (r) 949 ml, (s) 982 ml, (t) 989 ml, respectively.

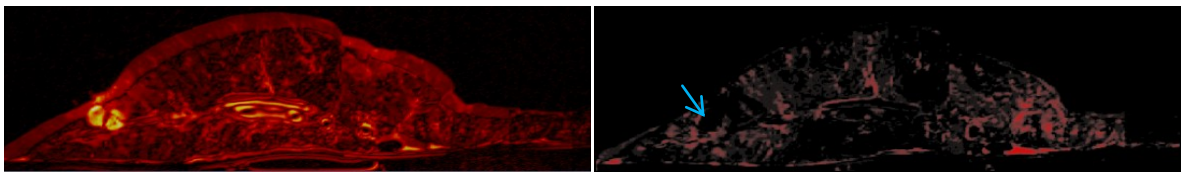

Figure 3.5: (a): one difference lung image slice passing through a tumor. It shows the difference between the CT image acquired at the least and most inflated phases in the respiratory image sequence. The tumors and the lung boundaries from the two images are clearly visible in the difference image. (b): the same difference image slice after the deformable registration, where the window and level functions have been adjusted to highlight the differences. The anatomy and the tumors have coincided reasonably accurately. The coincident tumors locations are pointed by an arrow.

Figure 3.6 demonstrates the extrapolation curve for one of the registration parameters (out of 65871 parameters). Available data values for this registration parameters were calculated in the registration block are shown with the "+" symbols as a function of V. These registration parameter values were obtained by registering the reference image with images within the respiratory CT sequence. A first order logarithmic polynomial (solid line) was fitted to these values through an optimization process, which was then extrapolated to estimate the required parameter value. The extrapolated values of the

65871 registration parameters were then used to construct the CT image of the lung in its totally deflated state from the reference image. The lung's volume, in its deflated state, was estimated at ~14% (V_d = 50 ml) of the lung's residual volume in the respiratory sequence (347 ml). This estimated value lies in the middle of the range (12%-16%) obtained in a number of experiments conducted before.

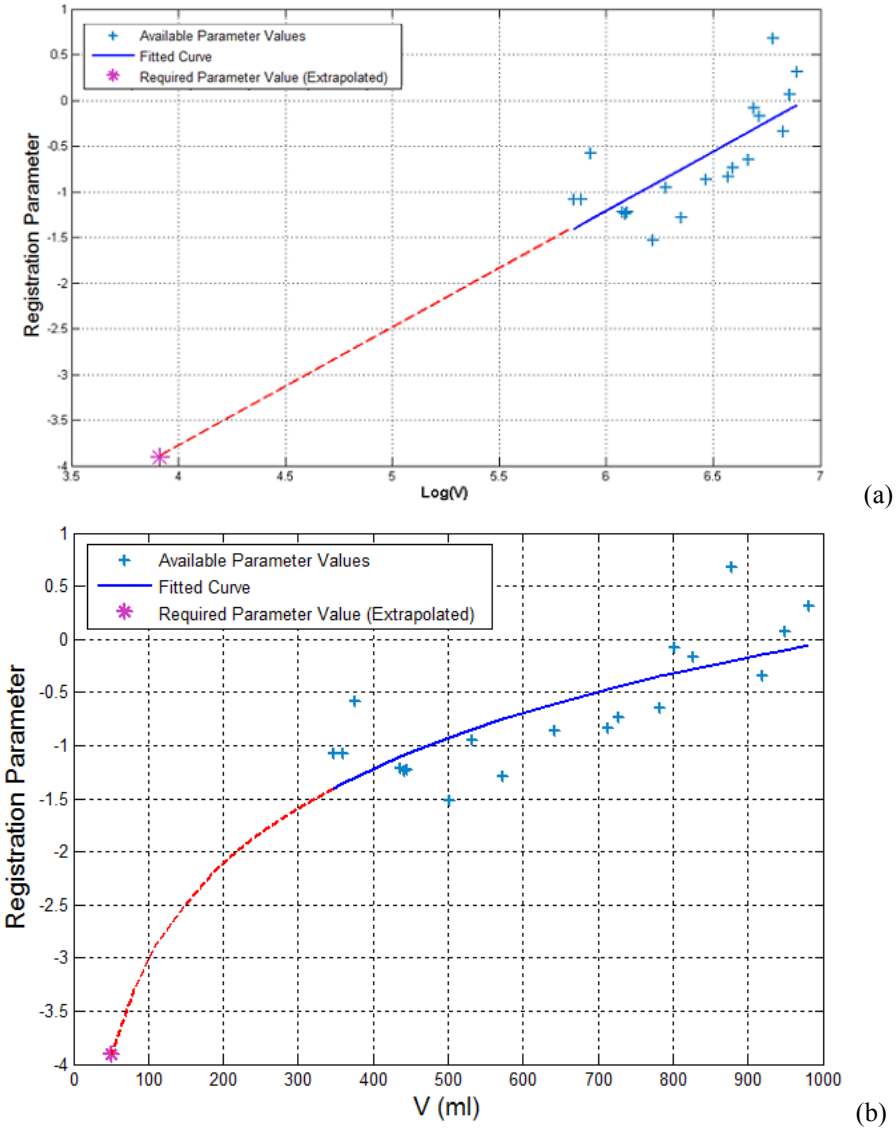

Figure 3.6: First order logarithmic polynomial (solid line) in: (a): logarithmic space; (b): linear space. The curve is fitted to available values of one of the registration parameters (shown by "+") obtained by registering the reference image with images within the respiratory CT sequence. The curve is then extrapolated (dashed line) in order to estimate the required parameter value ("*") to construct the CT image of the lung in its totally deflated state. This function empowers the FFD registration technique to capture highly complex deformations expected in the lung because several thousands of parameters are typically involved.

Figures 3.7 (a) and (b) illustrate one tumor passing slice of the lung's reference CT image and its corresponding tumor passing slice of the deflated lung's CT image acquired for the purpose of validation. Physical coordinates of the tumor's center are given in the parenthesis for both images. An anatomical feature, which may be regarded as a fiducial marker, is also marked in the deflated lung and its physical coordinates are presented. This anatomical feature is located in physical coordinates of (207.9, 100.7, 104.8) mm in the reference image. Figure 3.7 (c) shows the extrapolated deformation fields (arrows) fused with the two overlaid CT image slices shown in Figure 3.7 (a) and (b) where the location of the tumor in the overlaid images is highlighted with circles. It can be seen that the extrapolated arrows clearly point to the directions of local deformations used to construct the CT image of the lung in its totally deflated state. Figure 3.7 (d) demonstrates the constructed CT image where the center of the tumor and the anatomical feature physical coordinates are given in parenthesis. Difference images of the totally deflated lung's CT image with the lung's reference CT image as well as with the deflated lung's constructed CT image are illustrated in Figure 3.7 (e) and (f), respectively. In these images, the intensity mean absolute differences were calculated to be at 7% and 1%, respectively. The constructed CT image shows very good similarity with the corresponding actual CT image of the deflated lung shown in Figure 3.7 (b). The high accuracy of the constructed CT image can be more appreciated by comparing the physical coordinates of the tumor's center and the traced anatomical feature in the constructed and validation CT images. The error vectors for the physical coordinates of the tumor's center and the traced anatomical feature in the constructed images are (0.5, 0.5, 0.0) mm and (0.5, 0.0. 0.0) mm, respectively. The maximum misalignment of these features in one direction is only 0.5 mm which is highly desirable in the lung brachytherapy application. In order to further validate the constructed CT image's accuracy, 10 other anatomical fiducial markers were traced in different corresponding slices of the constructed and the deflated lung's CT images where an average error vector of (0.64, 0.39, 0.11) mm was obtained. While the obtained results are encouraging as they clearly demonstrate a proof of principle and feasibility of the proposed technique, further *in vivo* studies are required to assess its accuracy and suitability in the clinic.

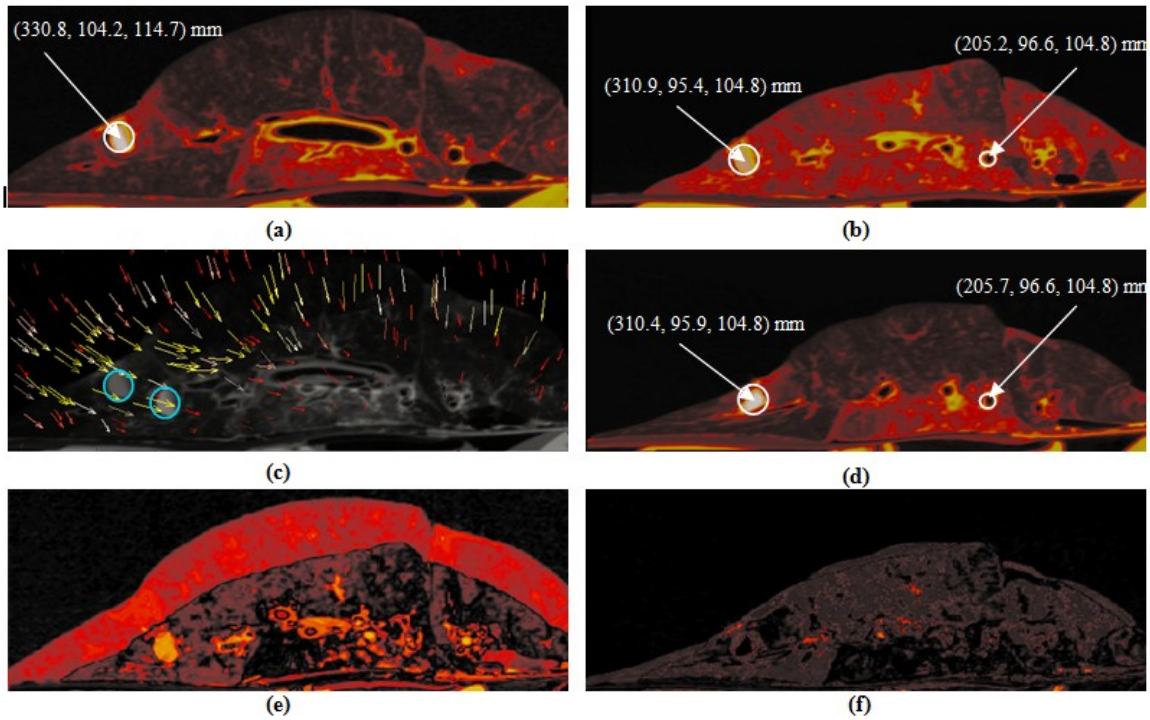

Figure 3.7: One tumor passing slice of the (a): lung's reference CT image (989ml), (b): totally deflated lung's CT image (required), (d): constructed CT image of the deflated lung; the center of the tumor and anatomical feature physical coordinates is given in parenthesis. The physical coordinates of the anatomical feature in the reference image is (207.9, 100.7, 104.8) mm. (c): extrapolated deformation field (arrows) fused with the two overlaid CT images of the lung in its most inflated (reference) and totally deflated (required) states; the locations of the tumor in the overlaid images is highlighted with circles; the extrapolated arrows clearly point to the directions of local deformations used to construct the CT image of the lung in its totally deflated state based on the reference image. (e): difference image of the lung's reference CT image and the totally deflated lung's CT image (required) and (f): difference image of the totally deflated lung's constructed CT image and the totally deflated lung's original CT image (required).

Finally, the effect of using a subset of pre-operative CT images (instead of the whole set) in the CT image construction process was investigated. Figure 3.8 (a)-(d) demonstrate the construction results using two, three, six, and ten pre-operative images out of twenty where the center of the tumor physical coordinates is given in parenthesis. As can be seen in these images, the quality of the reconstructed images is low in Figure 3.8 (a) and (b) where a few unrealistic artifacts can be seen. However, the constructed image quality is acceptable in Figure 3.8 (c) and (d). Accuracy of these constructed CT images can be further appreciated by comparing the physical coordinates of the tumor's center in the constructed and acquired CT images of the deflated lung. In comparison

with Figure 3.7 (b) the corresponding misalignment error vector of the tumor's center in Figure 3.8 (a)-(d) are (14.3, 7.4, 5.1) mm, (13.9, 6.6, 4.7) mm, (3.4, 2.5, 3.5) mm, (0.9, 1.3, 0) mm, respectively. It can be concluded that applying more pre-operative image in the construction process would result in more accurate constructed CT image. In this investigation the results indicate that while using a small subset of pre-operative images may cause significant errors and unrealistic artifacts, employing ten or more pre-operative images results in reasonably accurate constructed CT image.

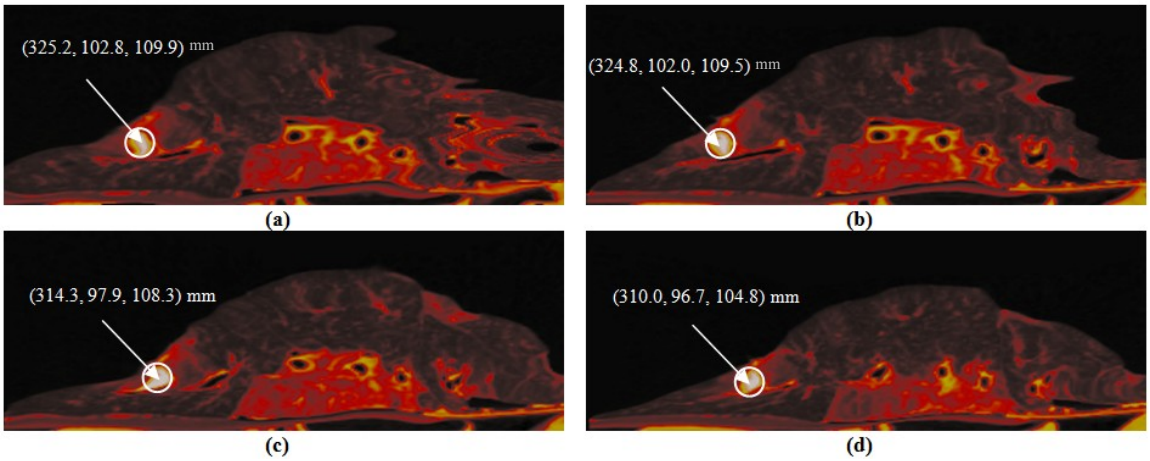

Figure 3.8: Effects of using a subset of 20 pre-operative 4D-CT images in the CT image construction process with figures (a), (b), (c), (d) showing using 2, 3, 6, and 10 pre-operative images, respectively. The center of the tumor physical coordinates is given in parenthesis. The original CT image of the totally deflated lung (required) is shown in Figure 3.7 (b).

3.5 Discussion and Conclusion

A new technique was introduced in this chapter to construct CT image of a totally deflated lung using the lung's free-breathing 4D-CT image sequence acquired pre-operatively. In principle, precise and high quality images of the deflated lung are very useful in implementing ablative procedures such as image-guided brachytherapy for lung cancer treatment as the target lung is almost completely deflated during such procedures. The proposed technique involves determining the lung tissue deformations that occur during the respiratory cycles. Each deformation is presented by means of free-form deformable registration parameters. This step is followed by formulating the obtained registration parameters as functions of the lung's air volume variations. The image

construction pipeline estimates the lung's air volume automatically in each image using the technique proposed in Chapter 2; hence there is no need to use any external marker for position tracking throughout the respiratory cycle. The fitted deformation function is then used to extrapolate parameters of tissue deformation that would occur as a result of total deflation of the lung. The predicted deformation is finally used to construct a new CT image corresponding to the lung in its deflated state from one of the lung's pre-operative images that we used as a reference image.

The technique was evaluated by conducting *ex vivo* experiments on a porcine lung. Results obtained from these experiments were very encouraging as they demonstrated the technique's capability of constructing reliable CT image of the deflated lung. To assess the techniques accuracy, we used the tumor area in addition to a number of anatomical features as fiducial markers. In this assessment, the average misalignment in the constructed CT image was found to be (0.64, 0.39, 0.11) mm. Such an accurate constructed CT image of the totally deflated lung is potentially suitable in image-guided procedures for pre-operative tasks (such as treatment planning), as well as for intra-operative tasks (such as tumor localization, and fusing with real-time navigation data) that involve image registration with intra-operative ultrasound (US) images in order to enhance their poor quality. However, *in vivo* experiments are required for further assessing the reliability and accuracy of the proposed techniques in clinical applications where other sources of error such as cardiac and breathing motions are introduced to the system.

References

[1] A. Sadeghi Naini, R. V. Patel, A. Samani, “CT image construction of the lung in a totally deflated mode”, Proc. of the 2009 IEEE International Symposium on Biomedical Imaging: From Nano to Macro (ISBI 2009), Boston, Massachusetts, USA, pp. 578-581, June 2009.

[2] A. Sadeghi Naini, R. V. Patel, A. Samani, “A totally deflated lung’s CT image construction by means of extrapolated deformable registration”, Proc. of SPIE Medical Imaging 2011: Image Processing, Orlando, Florida, USA, Vol. 7962, 796228, February 2011.

[3] G. Carnes, S. Gaede, E. Yu, J. V. Dyk, J. Battista, T. Y. Lee, “A fully automated non-external marker 4D-CT sorting algorithm using a serial cine scanning protocol,” Phys. Med. Biol., 54, 2049–2066 (2009).

[4] J. V. Hajnal, D. L. G. Hill, D. J. Hawkes, “Medical image registration”, CRC Press, Boca Raton, 2001.

[5] D. Ruckert, L. I. Sonoda, C. Hayes, D. L. G. Hill , M. O. Leach , D. J. Hawkes, “Nonrigid registration using free-form deformations: Application to breast MR images”, IEEE Trans. Med. Imaging, vol. 18, no. 8, pp. 712-721, 1999.

[6] J. Kybic, M. Unser “Fast parametric elastic image registration” IEEE Trans. Med. Imaging, vol. 12, no. 11, pp. 1427-1441, 2003.

[7] T. Rohlfing, C.R. Maurer, W.G. O'Dell, J. Zhong, “Modeling liver motion and deformation during the respiratory cycle using intensity-based nonrigid registration of gated MR images” Med. Phys., vol. 31, no. 3, pp.427-432, 2004.

[8] J. R. McClelland, A. G. Chandler, J. M. Blackall, S. Ahmad, D. B. Landau, D. J. Hawkes, “4D motion models over the respiratory cycle for use in lung cancer radiotherapy planning”, Proc. SPIE 5744, pp. 173–183, 2005.

[9] J. R. McClelland, J. M. Blackall, S. Tarte “A continuous 4D motion model from multiple respiratory cycles for use in lung radiotherapy”, Med. Phys., vol. 33, no. 9, 2006.

[10] S. Lee, G. Wolberg, S. Y. Shin, “Scattered data interpolation with multilevel B-splines”, IEEE Trans. Visualization Comput. Graph., vol. 3, pp. 228–244, 1997.

[11] C. Runge, "Über empirische Funktionen und die Interpolation zwischen äquidistanten Ordinaten", Zeitschrift für Mathematik und Physik, vol. 46, pp. 224–243, 1901.

[12] J. P. Berrut, L. N. Trefethen, "Barycentric Lagrange interpolation", SIAM Review, vol. 46, pp. 501–517, 2004.

[13] D. Mattes, D. R. Haynor, H. Vesselle, T. K. Lewellen, W. Eubank, “PET-CT image registration in the chest using free-form deformations,” IEEE Trans. on Medical Imaging, 22(1), 120-128, (2003).

Chapter 4

CT Enhanced Ultrasound Image of a Totally Deflated Lung

The material presented in this chapter has been published in IEEE Tran. Biomed. Eng., 57(10): 2627-2630 (2010).[*]

4.1 Introduction

IMAGING technologies play a significant role in Minimally Invasive Surgery (MIS) procedures by making it possible to visualize tissue target areas pre- and/or intra-operatively or even remotely. The role of imaging in this context is so critical that most of the state of the art MIS treatment systems were fully implemented only after challenges related to their imaging component were addressed thoroughly [1-4]. Lung tumor ablative procedures, such as Low Dose Rate (LDR) brachytherapy, follow the same rule. As described earlier, the concept of lung brachytherapy involves using ultrasound (US) imaging intra-operatively. To adapt a minimally invasive approach for lung cancer therapy, a number of difficulties need to be overcome. They include lack of: 1) useful three-dimensional (3D) images of the tumor for treatment planning, 2)

---

[*] © 2011 IEEE. This modified version has been reprinted, with permission, from A. Sadeghi Naini, R.V. Patel, and A. Samani, "CT enhanced ultrasound image of a totally deflated lung for image-guided minimally invasive tumor ablative procedures", IEEE Transaction on Biomedical Engineering, October 2010.

possibility to localize the tumor intra-operatively and 3) possibility to overlay real-time navigation information with image data during the procedure [5]. The two latter difficulties stem from the poor quality of intra-operative US images of the deflated lung. Such difficulties do not arise in similar applications, e.g., US-guided prostate brachytherapy [6, 7], as the poor image quality is due to residual air remaining in the deflated lung. Pre-operative Computed Tomography (CT) or Magnetic Resonance (MR) Images are frequently used with brachytherapy applications such as brain brachytherapy [1, 2]. Such images are not as effective in lung brachytherapy because the target lung is almost completely deflated during surgery whereas pre-operative images are acquired while the lung is partially inflated. To address the poor quality issue of the intra-operative US images of the deflated lung, it is possible to register the US images with more reliable and high-quality images obtained pre-operatively. A suitable candidate for such high quality image is pre-operative CT images. However, given that they correspond to the inflated lung, the CT images need to be pre-processed to obtain CT images pertaining to the lung's deflated state. This issue was addressed in Chapter 3 by developing a novel construction technique to obtain CT image of a totally deflated lung using its pre-operative images acquired in different phases of respiration. This fully automatic technique does not require any external marker as it is capable of estimating the lung's air volume from the CT images automatically using a newly developed segmentation approach described in Chapter 2.

During recent years, multi-modal registration of CT and US images has been applied in other biomedical applications including orthopaedic surgery [8], head and neck cancer treatment planning [9], femur and pelvis surgery [10], kidney and liver indeterminate lesions diagnosis [11], liver surgery [12], and minimally invasive cardiac procedures [13]. Unlike in lung tumor ablative procedures, these applications do not involve major tissue deformation. Hence, the pre-operative CT images still represent the anatomy's physical domain and can be directly applied intra-operatively. In addition, although the quality of US images in these applications tend to be lower than their CT images counterpart, it is not considered poor since anatomical structures and features are relatively detectable in the US images. Such anatomical information is very helpful in the registration process required for accurate image alignment. As such, the registration

process employed in almost all of the above research work consists of a simple rigid or affine registration. Among them a few used semi-automatic non-rigid registration in their process. These latter techniquess are land-mark based, which again require visibility of anatomical features in US images.

In this chapter, an enhancement pipeline is proposed to improve the quality and usability of a deflated lung's intra-operative US images undergoing tumor ablative procedure. As described in Section 4.2, the proposed pipeline applies two concurrent and fully-automatic registration processes which do not need registration landmarks. The pipeline outputs an enhanced intra-operative US image positioned and oriented accurately in its corresponding deflated lung CT image. The proposed pipeline employs higher quality information of the constructed CT image to improve the quality of the US image. This research introduces a CT enhanced US image of a totally deflated lung for the first time to complement the CT image construction technique proposed in Chapter 3. The enhanced intra-operative US images of the deflated lung in conjunction with the constructed CT image can be used effectively for intra-operative tumor localization as well as surgical tools navigation during a minimally invasive tumor ablative procedure. To the author's knowledge, no other intra-operative system has been developed before for lung brachytherapy. A schematic structure of an image-guided minimally invasive lung's tumor ablative procedure based on the solution introduced in this chapter is shown in Figure 4.1. *Ex vivo* experiments were conducted in order to validate the technique. The results are given in Section 4.3, which indicate that the proposed technique is useful for enhancing the quality of deflated lung's intra-operative US images as it yields reasonably accurate and reliable images of lung undergoing tumor ablative procedure. As discussed and concluded in Section 4.4, this is a significant milestone for our ongoing development of a precise system for lung tumor ablative procedures.

4.2 The US Enhancement Pipeline

The proposed US enhancement pipeline is input with a pre-operative four-dimensional CT (4D-CT) respiratory image sequence and an intra-operative US image of a slice containing the tumor area. The pre-operative 4D-CT sequence is used to construct the CT image of the totally deflated lung using the technique described in Chapter 3. Next, a 3D

CT sub-volume surrounding the target tumor area is cropped from the whole CT volume. The 3D sub-volume along with the two-dimensional (2D) US slice is taken through two simultaneous processes: 1) a (rigid + affine) registration, briefly described in Section 3.2.1, where the 2D US slice is registered into the 3D CT sub-volume; 2) a free-form deformation registration (rigid + affine + deformable), briefly described in Section 3.2.2, where the 3D CT sub-volume is registered into the 2D US slice. In the former registration process the best position and orientation of the 2D US slices within the 3D CT is found. The latter registration process, which employs a B-spline registration as the deformable registration, is conducted for enhancing the quality of the 2D US image using higher quality information within the CT sub-volume. In order to avoid being trapped in local minima during optimization in the deformable registration process, the applied B-spline registration involves a multi resolution mesh scheme starting with a coarse mesh. The pipeline's output is a CT enhanced US image of the totally deflated lung positioned and oriented accurately in its pre-operatively constructed CT counterpart. Figure 4.2 represents a schematic view of the enhancement pipeline proposed.

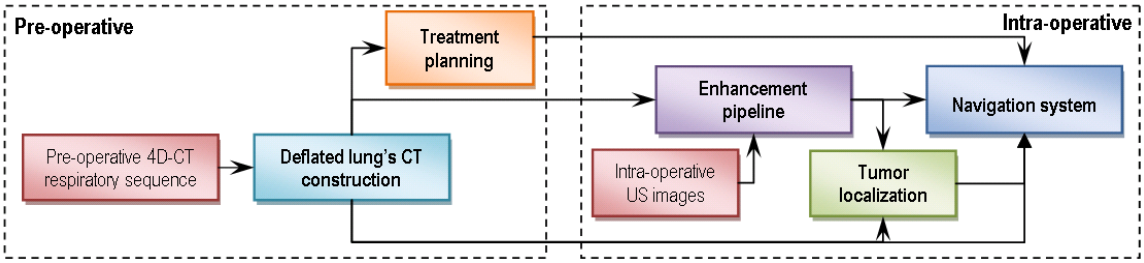

Figure 4.1: Schematic structure of the proposed image-guided minimally invasive lung tumor ablative procedure. Pre-operative steps start with acquiring a 4D-CT respiratory sequence used to construct CT image of the deflated lung. This CT image is initially used for pre-operative treatment planning. In intra-operative phase, US images are enhanced using the constructed CT image. Tumor localization is performed by applying the enhanced US image in conjunction with the constructed CT image. These two images along with the planned treatment are also employed in intra-operative navigation.

4.3 Experiments and Results

Ex vivo experiments were conducted on a porcine lung in order to evaluate the accuracy of the proposed technique. A number of phantom tumors were sutured inside the porcine

left lung. The tumors were constructed of gelatin and agar in addition to ~3 mg/ml iodine CT contrast agent such that they had a Hounsfield Unit of ~200 HU. After tumor suturing, the lung was respired using an intra-trachea tube in conjunction with a ventilator machine. A 4D-CT respiratory sequence was next acquired while the lung was being respired continuously.

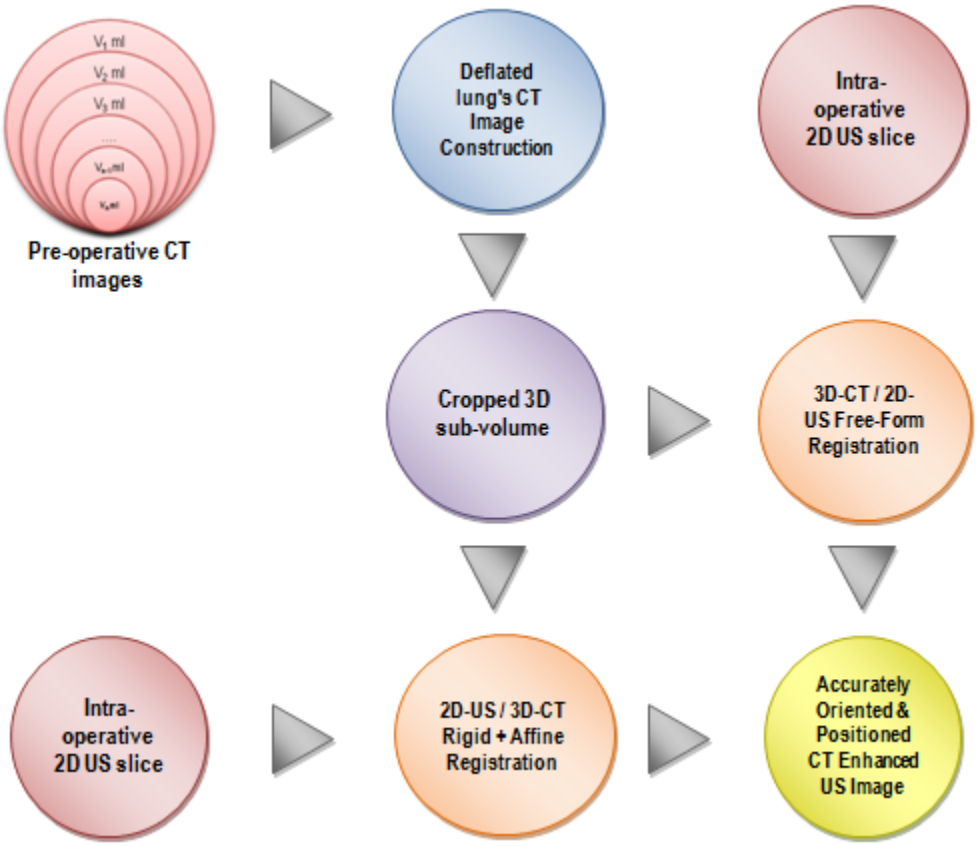

Figure 4.2: Schematic view of the intra-operative US enhancement pipeline: CT image of the totally deflated lung is constructed pre-operatively. A 3D CT sub-volume surrounding target tumor area is first cropped from the whole CT volume. The 3D sub-volume along with the intra-operative 2D US slice go through 2 simultaneous processes: 1) a (rigid + affine) registration of the 2D US into the 3D CT in which the best position and orientation of the 2D US slices within the 3D CT is found; 2) a free-form registration (rigid + affine + deformable) of the 3D CT into the 2D US in which the quality of the 2D US image is enhanced. The output is a CT enhanced US image of the totally deflated lung positioned and oriented accurately in its pre-operatively constructed CT counterpart.

The scans were performed using a GE Healthcare Discovery CT 750 HD scanner. A series of sequential adjacent cine scans were performed. Each scan had a 4.0 cm axial

field of view. The CT scanning parameters were: 80 kVp, 200 mA and a gantry rotation period of 0.4 s. The 4D-CT images were produced using a 4D-CT sorting method proposed in [14]. Afterwards, the lung was taken into the operation room where it was completely deflated by applying a negative pressure via the bronchi. A number of intra-operative 2D US images were, then, acquired from the target tumor area using an Ultrasonix Sonix RP system and a L14-5/38 transducer. The frequency of the transducer was set to 10 MHz and the acquired images had a dynamic range of 75dB. The acquired 4D-CT image sequence was used to construct a CT image of the lung in its totally deflated mode. The resultant image is displayed in Figure 4.3 using MicroView open source software (GE Healthcare). This Figure demonstrates one sagittal and one axial plane of the constructed CT image passing through a tumor. The cropped 3D sub-volume (40×85×40 voxels) surrounding the target tumor is highlighted in this image. This 3D sub-volume along with the intra-operative US slice (269×341 pixels) were used in two simultaneous registration processes in the enhancement pipeline. Mutual information was employed as similarity measure in all of the multi-modal registration processes [15]. The interpolation was performed using a simple linear interpolator in the registration processes. In the hierarchical deformable registration grids of 4×4×4 to 6×6×6 control points were used. The enhancement pipeline was run on a machine with a dual core CPU (2×2.83 GHz) and 4.00 GB RAM. Using this machine, the two concurrent registration processes performed in the pipeline took 102 Sec and 107 Sec to converge, respectively.

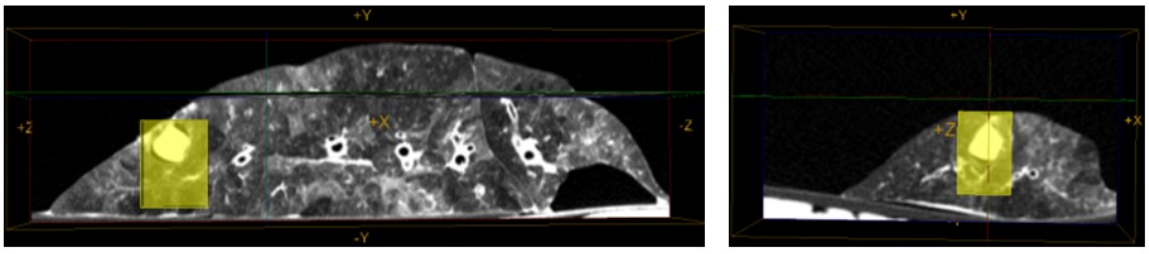

Figure 4.3: One Sagittal (left) and one axial (right) plane of the constructed CT image of the totally deflated lung. The 3D sub-volume surrounding the target tumor employed in the registration processes is highlighted.

The resultant images are displayed using ParaView open source software (Kitware, Inc.). The optimum position and orientation obtained for the 2D US slice within the 3D

sub-volume, which led to the best tumor alignment, is presented in Figure 4.4. After this registration step, misalignments of the tumor and anatomy boundaries were estimated by two medical experts to be at about 4.5-5.5 mm. A number of point to point misalignment measurements performed on the tumor's center and the tumor and anatomy boundaries using a medical image analysis software confirmed the experts' maximum misalignment estimation. The average and maximum amounts of misalignments determined by the software were 3.98 mm and 5.1 mm, respectively. The major source of these misalignments is the local deformations occurred in the lung tissue because of: 1) transferring the lung from the CT bed to the operation room, and 2) the pressure applied at the lung's surface by the US probe.

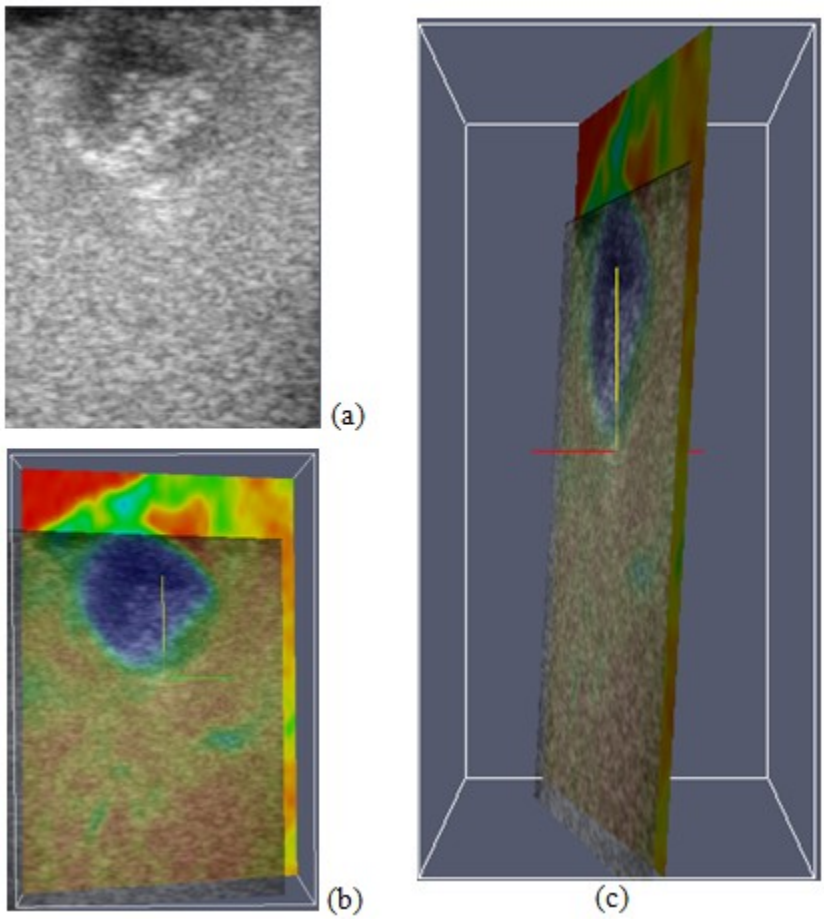

Figure 4.4: Orientation and position of the 2D-US plane within the 3D-CT sub-volume obtained throughout a 2D-US/3D-CT (rigid + affine) registration. (a): Original intra-operative 2D-US slice. (b): Overlaid 2D-US plane on its corresponding oriented plane from 3D-CT sub-volume. (c): Orientation of the overlaid US/CT planes in the 3D-CT sub-volume.

Figure 4.5 demonstrates the results of US slice enhancement. The original and CT enhanced US slices are shown in Figure 4.5 (a) and (b), respectively. These two slices are overlaid in Figure 4.5 (c). As can be seen in these images the quality of the original US slice has been considerably improved. The tumor boundaries as well as different tissue regions which are not clear or even detectable in the original US slice can be clearly determined in the enhanced US slice. Misalignments of the tumor and anatomy boundaries are estimated by two medical experts to be within 0.5-1.25 mm, which indicates high accuracy. A number of point to point misalignment measurements were performed using the medical image analysis software. These involved the tumor's center and its boundary in addition to the lung's boundary. This assessment verified the experts' estimations and confirmed the high accuracy of CT enhanced US slice. The average amount of misalignments determined by the software was 1.06 mm. Such an accurate and reliable image of the deflated lung would address one of the major challenges encountered in lung minimally invasive tumor ablative procedures.

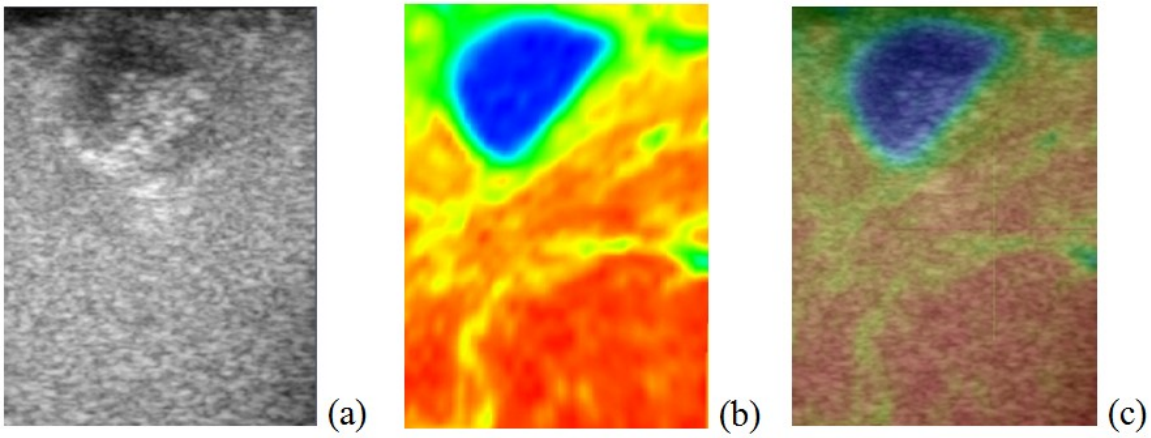

Figure 4.5: Results of the US enhancement. (a): intra-operative US image of the lung's tumor area, (b): CT enhanced version of the US image obtained through a 3D-CT/2D-US free-form deformation registration, (c) original US image overlaid on its CT enhanced version.

4.4 Discussion and Conclusion

In this chapter, an image enhancement pipeline was introduced to improve the quality of intra-operative US images. The pipeline uses higher quality CT image of a deflated lung constructed pre-operatively, in order to enhance the US quality and its usability. The core part of the pipeline consists of two simultaneous registration processes with exchanged

fixed and moving images. The first process determines the optimum orientation and position of the US slice within the CT volume, and the second one improves its quality. The output is a CT enhanced US image of a totally deflated lung oriented and positioned accurately within its pre-operative CT counterpart. The technique was validated through *ex vivo* porcine lung experiments. Obtained results from these experiments are encouraging both in terms of registration accuracy and image quality improvement. The whole registration based image enhancement procedure took less than 110 sec on a regular desktop computer. This confirmed that a considerable image quality improvement can be achieved relatively fast. More computational power or Graphics Processing Unit (GPU) based computing is necessary to achieve real-time US image enhancement. As such, this work may be regarded as a promising step for clinical implementation of image-guided minimally invasive lung tumor ablative procedures.

References

[1] R. C. Krempien, S. Daeuber, F. W. Hensley, M. Wannenmacher, W. Harms, "Image fusion of CT and MRI data enables improved target volume definition in 3D-brachytherapy treatment planning", Brachytherapy vol. 2, pp. 164–171, 2003.

[2] N. Tselis, C. Kolotas, G. Birn, S. Röddiger, I. Filipowicz, M. Kontova, G. Fountzilas, P. Selviaridis, D. Baltas, R. Heyd, G. Anagnostopoulos, N. Zamboglou, "CT-guided interstitial HDR brachytherapy for recurrent glioblastoma multiforme", Strahlentherapie und Onkologie, vol. 183, pp. 563-570, 2007.

[3] G. Fichtinger, T. L. DeWeese, A. Patriciu, A. Tanacs, D. Mazilu, J. H. Anderson, K. Masamune, R. H. Taylor, D. Stoianovici, "System for robotically assisted prostate biopsy and therapy with intraoperative CT guidance", Journal of Academic Radiology, vol. 9, issue 1, pp. 60-74, 2002.

[4] G. Fichtinger, E. C. Burdette, A. Tanacs, A. Patriciu, D. Mazilu, L. L. Whitcomb, D. Stoianovici, "Robotically assisted prostate brachytherapy with transrectal ultrasound guidanced–phantom experiments", Brachytherapy, vol. 5, issue 1, pp. 14-26, 2006.

[5] A. W. Lin, A. L. Trejos, R. V. Patel, R. A. Malthaner, "Robot-Assisted Minimally Invasive Brachytherapy for Lung Cancer", Telesurgery, Springer Berlin Heidelberg, 2007, Chap. 4, pp. 33-52.

[6] S. Nag, J. P. Ciezki, R. Cormack, S. Doggett, K. DeWyngaert, G. K. Edmundson, R. G. Stock, N. N. Stone, Y. Yu, M. J. Zelefsky, "Intraoperative planning and evaluation of permanent prostate brachytherapy: report of the American Brachytherapy Society", Int. J. Radiat. Oncol. Biol. Phys., vol. 51, no. 5, pp.1422–1430, 2001.

[7] H. Bassan, T. Hayes, R. V. Patel, M. Moallem, "A novel manipulator for 3D ultrasound guided percutaneous needle insertion", IEEE International Conference on Robotics and Automation, Rome Italy, pp. 617-622, 2007.

[8] B. Brendel, S. Winter, A. Rick, M. Stockheim, H. Ermert, "Registration of 3D CT and Ultrasound Datasets of the Spine using Bone Structures", Computer Aided Surgery, vol. 7, pp. 146–155, 2002.

[9] W. Wein, B. Roper, N. Navab, "Automatic registration and fusion of ultrasound with CT for radiotherapy", Med Image Comput Comput Assist Interv, vol. 8, Part 2, pp. 303-311, 2005.

[10] G. P. Penney, D. C. Barratt, C. S. K. Chan, M. Slomczykowski, T. J. Carter, P. J. Edwards, D. J. Hawkes, "Cadaver validation of intensity-based ultrasound to CT registration", Medical Image Analysis, vol. 10, pp. 385-395, 2006.

[11] W. Wein, S. Brunke, A. Khamene, M. R. Callstrom, N. Navab, "Automatic CT-ultrasound registration for diagnostic imaging and image-guided intervention",

Medical Image Analysis, vol. 12, pp. 577-585, 2008.

[12] T. Lange, N. Papenberg, S. Heldmann, J. Modersitzki, B. Fischer, H. Lamecker, P. M. Schlag, "3D ultrasound-CT registration of the liver using combined landmark-intensity information", Int. J. CARS, vol. 4, pp. 79-88, 2009.

[13] X. Huang, J. Moore, G. Guiraudon, D. L. Jones, D. Bainbridge, J. Ren, T. M. Peters, "Dynamic 2D Ultrasound and 3D CT Image Registration of the Beating Heart", IEEE Trans. Med. Img., vol. 28, no. 8, pp. 1179-1189, 2009.

[14] G. Carnes, S. Gaede, E. Yu, J. V. Dyk, J. Battista, T. Y. Lee, "A fully automated non-external marker 4D-CT sorting algorithm using a serial cine scanning protocol", Phys. Med. Biol., vol. 54, pp. 2049–2066, 2009.

[15] D. Mattes, D. R. Haynor, H. Vesselle, T. K. Lewellen, W. Eubank, "PET-CT image registration in the chest using free-form deformations", IEEE Trans. on Medical Imaging, vol. 22, no. 1, pp. 120–128, 2003.

Chapter 5

Measuring Hyperelastic Properties of Lung Tissue

The material presented in this chapter has been peer reviewed in IEEE Tran. Biomed. Eng. (2011), and is undergoing first round of revisions for publication.[*]

5.1 Introduction

EXTENSIVE worldwide efforts, as described earlier, are ongoing to tackle lung cancer as the leading cause of cancer death in both men and women [1, 2]. In many biomedical applications related to computer aided lung cancer diagnosis and treatment planning, tissue deformation modelling is involved. In such applications having the biomechanical properties of lung tissues is a paramount necessity. An example of such applications includes Low Dose Rate (LDR) lung brachytherapy proposed for lung cancer treatment [3]. As described in Chapter 1, the major consideration in this minimally invasive procedure involves accurate radioactive seed implantation according to a pre-planned distribution pattern determined by clinician to achieve a proper radiation dosage. Small deviations in seed alignment can create significant areas of over- or under-dosage [4]. A significant challenge which frequently hampers the accuracy of brachytherapy seed

[*]

implantation, and consequently the entire procedure's outcome, is tumor motion due to soft tissue shift and deformation during respiration. This is because while the target lung is totally deflated during surgery in order to minimize the respiratory motion [5], the other lung's respiration is ongoing. Hence there is still considerable shift and deformation in the target lung due to respiratory contact forces. Compensating for tumor motion caused by such tissue shift and deformation requires biomechanical modeling of lung tissue [6]. This modeling can be performed by employing conventional Finite Element Method (FEM) [7] or the accelerated Statistical FEM (SFEM) which was recently proposed in [8]. An essential prerequisite for the tissue biomechanical modeling is having reliable biomechanical properties of the deflated lung tissues.

Respiratory tumor motion tracking is very challenging in external beam radiation therapy of the lung including Three-dimensional conformal radiotherapy (3D-CRT) [9], Intensity Modulated Radio Therapy (IMRT) [10], Stereotactic body radiation therapy [11], and Proton beam therapy [12]. This is because the target lung's respiration is ongoing during the procedure, hence the cancerous region moves significantly due to the resulting lung's tissue deformation. By taking into account the mechanical effects of inhaled air volume and/or pressure as well as diaphragm contact forces during respiration on the lung tissue deformation, the respiratory tumor motion can be estimated in a real-time fashion using the lung's SFEM based model [8]. A major advantage of this approach over approaches that employ pre-operative respiratory images for intra-operative tumor motion estimation [13] is that the former can take into account the gravity and contact forces effects in consistence with the patient's intra-operative positions.

Other computer aided surgical procedures can also benefit from measured lung tissue biomechanical parameters. This includes procedures where a needle and/or other surgical instruments need to be inserted in the lung tissue accurately and minimally invasively to reach a target area, *e.g.*, tumor. Needle biopsy and tumor ablative procedures for targeting lung cancer including cryotherapy [14, 15], Radio-Frequency Ablation (RFA) [16, 17], and LDR brachytherapy [3], are among examples of such cutting edge applications where tissue deformation affects the overall outcome of the operation, and hence need to be compensated for.

Virtual Reality (VR) systems have emerged recently to train surgical residents. They allow residents to train on their own schedule in addition to allowing trainees to review residents' practice sessions before progressing to real surgery [18]. The quality of such systems is assessed based on the realism of haptic and visual perception they provide. A determinant factor for such realism in VR systems used for lung and thoracic surgery training is the accuracy of lung tissue biomechanical properties [19-21]. While VR systems are frequently equipped with detailed anatomical description, they rarely contain accurately validated and reliable tissue biomechanical properties. This usually restricts the realistic haptic sense of the model and consequently limits its value. As such, enriching such systems with accurate biomechanical properties of lung tissue can significantly enhance their compatibility with the real cases and hence improve their reliability for training thoracic surgeons.

In principle, biomechanical properties of a material describe its stress-strain relationship under loading. Such relationship can be modeled through elastic or hyperelastic models. While the stress-strain relationship is presented by a linear equation in an elastic model, in a hyperelastic model, it is characterized through a nonlinear regime that takes into account both intrinsic material nonlinearity, and geometric nonlinearity arising from large deformation. Most biological soft tissues including lung tissues are intrinsically hyperelastic as they exhibit a nonlinear biomechanical response [22]. However, in many biomedical applications [23-26], lung soft tissue is usually modeled based on linear elasticity which is only reliable for small strain values of less than 5% [27]. This is because while extensive research has been conducted to develop techniques to measure the elastic modulus of lung soft tissues [28-30], little research has been conducted to measure its hyperelastic properties. As such measuring the hyperelastic parameters of lung soft tissues is of major interest to researchers in the field as it is expected to provide data necessary to improve the accuracy of current biomechanical models of the lung used in various medical applications.

In this chapter hyperelastic properties of lung soft tissues have been characterized using an inverse Finite Element (FE) approach. Several indentation experiments were conducted on samples resected from several fresh porcine lung regions and lobes. Two

major reasons were behind the choice of porcine lung tissue. The first reason is that porcine lung anatomy and its tissue properties are quite similar to those of humans [31, 32]. This is not surprising since such similarity has also been found in biomechanical properties of other human and porcine tissues, *e.g.*, aorta and pulmonary trunk [33, 34]. The other reason is that porcine lung is frequently used as an animal model in many medical research projects where a new system for lung cancer diagnosis and/or treatment is under development and needs to be investigated before being clinically approved [5, 34-38]. To calculate the hyperelastic parameters of each sample a nonlinear inverse FE problem was formulated and solved by an optimization technique. This technique seeks the set of hyperelastic parameters that minimizes the difference between the experimentally acquired and FE simulated indentation force-displacement data. Comparison of force-displacement responses obtained from the calculated hyperelastic parameters with their experimental counterparts in conjunction with independent validation tests confirmed the accuracy and uniqueness of the obtained results.

5.2 Theory

In this thesis different strain energy models, which are frequently used for modeling biological soft tissue, were employed for characterizing the hyperelastic properties of lung tissue. The first model is the Ogden strain energy function which is defined as:

$$U=\sum_{i=1}^{N}\frac{2\mu_i}{\alpha_i^2}\left(\lambda_1^{-\alpha_i}+\lambda_2^{-\alpha_i}+\lambda_3^{-\alpha_i}-3\right)+\sum_{i=1}^{N}\frac{1}{D_i}\left(J_{el}-1\right)^{2i} \tag{5.1}$$

where α_i's are non-dimensional constants, μ_i's are the material constants, λ_i's are the deviatoric stretches, J_{el} is the elastic volume strain, and D_i is a compressibility coefficient that tends to zero for incompressible tissues such deflated lung tissue. In this research, a first-order Ogden model was applied where the hyperelastic material property was modeled with two unknown variables: μ the initial shear modulus, and α.

The second hyperelastic model applied in this study, the Polynomial model, has a strain energy function as follows:

$$U = \sum_{i+j=1}^{N} C_{ij}\left(I_1 - 3\right)^i \left(I_2 - 3\right)^j + \sum_{i=1}^{N} D_i \left(J_{el} - 1\right)^{2i} \tag{5.2}$$

where C_{ij} are the unknown parameters with a physical dimension of [F/L^2], I_1 and I_2 are strain invariants, and J_{el}, and D_i have the same meanings as in Equation 5.1. In this study, a second-order Polynomial strain energy function was applied which results in five hyperelastic parameters.

It has been observed that constitutive equations of many materials including biological tissues are less sensitive to the second strain invariant I_2. This led to the development of Yeoh hyperelastic model, which is the third model applied in this research. This model follows a modified form of the third order Polynomial model where the strain energy function is independent of I_2 leading to the following:

$$U = \sum_{i=1}^{3} C_{i0}\left(I_1 - 3\right)^i + \sum_{i=1}^{N} D_i \left(J_{el} - 1\right)^{2i} \tag{5.3}$$

where C_{i0}, I_1, J_{el}, and D_i have the same meanings as in Equation 5.2. This formulation results in three hyperelastic parameters.

5.3 Method

Figure 5.1 demonstrates a flowchart of the algorithm applied in this study used to determine the unknown parameters of interest for each hyperelastic model. This optimization algorithm is a modified version of the algorithm developed by O'Hagan and Samani [39]. It systematically changes the set of unknown hyperelastic parameters for each model to find the best parameter set that yields the optimum fit between the experimental and simulated FE force-displacement profiles.

5.3.1 Sample's FE Meshing

As illustrated in Figure 5.1 the iterative optimization process initially requires the tissue specimen to be meshed for FE analysis. The process applied for creating each sample's 3D FE mesh involved reducing the meshing area to a radius of approximately 10*r*, where

r = 0.75 mm refers to the radius of the indenter. The reason behind this simplification was that in numerical FE experiments conducted there was insignificant vertical and in-plane displacements and stresses at the model's edges. This is in line with Saint-Venant's principle, which implies that the effects of point load applied at a point decays so fast that they can be ignored in regions far from the load. As such, while it does not impose considerable error on the model's accuracy, this geometry simplification can effectively reduce the FE model complexity. Since all of the applied tissue specimens were resected such that they had a larger area than *10r,* the applied geometry simplification resulted in a homogenous cylindrical mesh with a radius of *10r,* and a specific height for each sample. Eight node hexahedral elements were used for meshing the specimens' geometry. The meshing algorithm developed in this research involved the use of a transfinite interpolation technique [40] to transform five rectangular grids in the logical domain to the spatial domain. With the meshing also involved using Compactly Supported Radial Basis Functions (CSRBF) [41] to warp part of the grid to the boundary of the circular indentation area. Figure 5.2(a) shows result of FE meshing for a typical lung specimen. Based on the height of the samples, the mesh in this work contained 5551 to 15860 elements. In a FE mesh convergence analysis conducted, it was observed that increasing the number of these elements had very little impact on the results.

5.3.2 Optimization Algorithm for Hyperelastic Parameters Estimation

The hyperelastic parameters, $C = [c_1, \ldots, c_n]$, are estimated using optimization. This involves finding the set of hyperelastic parameters that lead to the best FE fit of the indentation experiment force-displacement data. As such, as indicated in the flowchart, the objective function to be minimized is of the following least squares form:

$$\min_{C} f(C) = \sum (F_{Exp}(\Delta) - F_{FEM}(\Delta))^2 \tag{5.4}$$

Following the flowchart in Figure 5.1, after the sample model mesh generation the hyperelastic parameters are next initialized to create the FE model. This is followed by inputting the indentation displacement data (Δ) and starting the FE analysis (Figure 5.2(b)). The FE analysis was conducted using ABAQUS software (D S Simulia. ©

Dassault Systèmes, 2004, 2011). Next, *f*, the Least Squares Error (LSE) between the computed reaction forces ($F_{FEM}(\Delta)$) and the experimental forces ($F_{Exp}(\Delta)$) are calculated. In the next step, the calculated LSE is compared to a user-defined tolerance. The optimization process is terminated if the tolerance condition is met; otherwise the hyperelastic parameters are updated. To achieve the best accuracy and convergence, two different methods were utilized for updating the parameters depending on the hyperelastic model. For the Polynomial and Yeoh models, the slope-variation technique [39] was used, whereas for the Ogden model the Nelder–Mead simplex method [42] was employed. In all cases, the iterative process was terminated when the specified tolerance condition was met, at a maximum of 40 iterations, or when the least-squares error measure displayed no improvement. To ensure uniqueness of the estimated parameters, the optimization algorithm was initiated with various initial values. It was observed that the final calculated parameters for every model were independent of the parameters initiation.

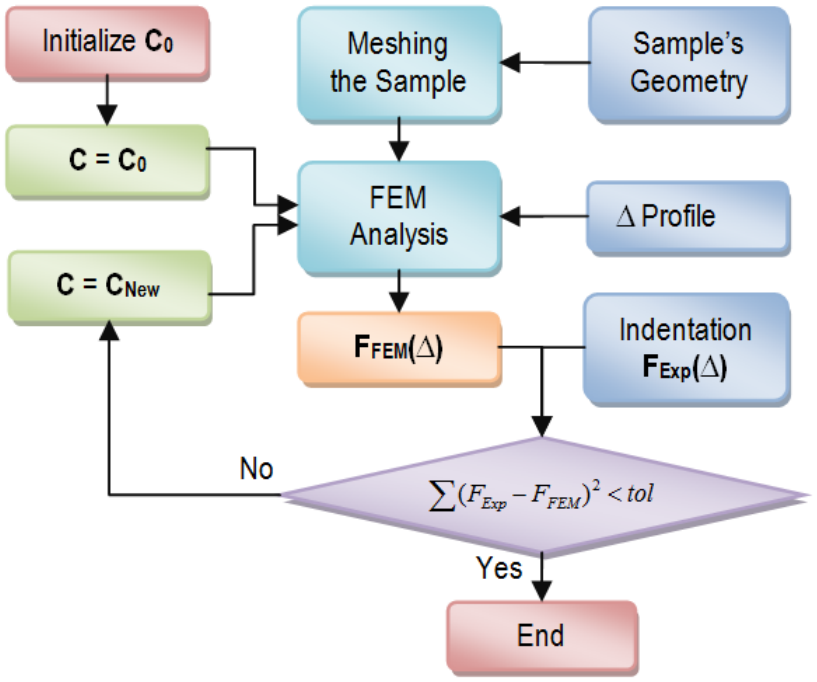

Figure 5.1: Flowchart of the algorithm used to calculate the optimum hyperelastic parameters of the lung tissue samples based on the sample's geometry and the force (F_{Exp})/displacement (Δ) data acquired throughout the indentation process.

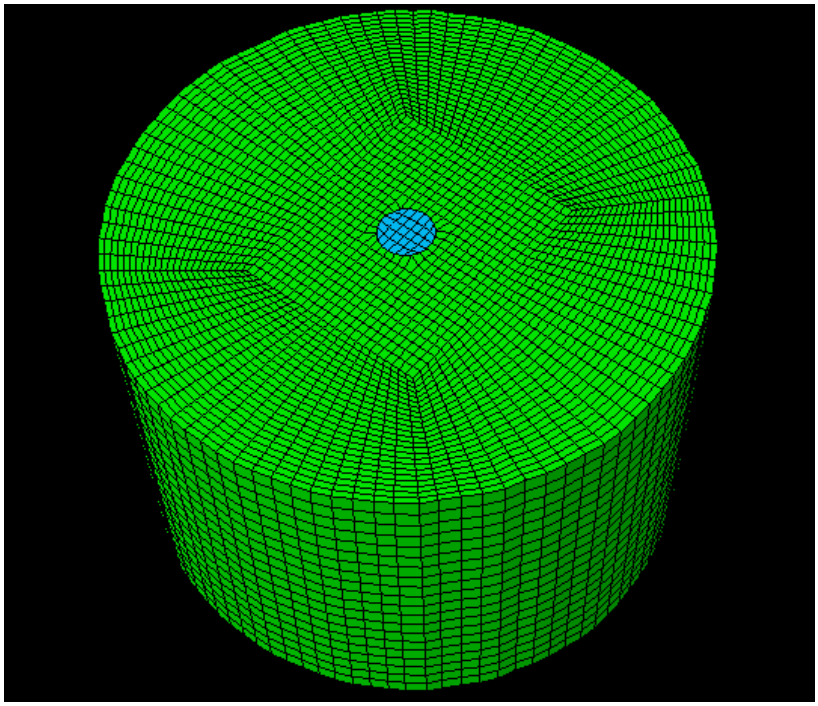

(a)

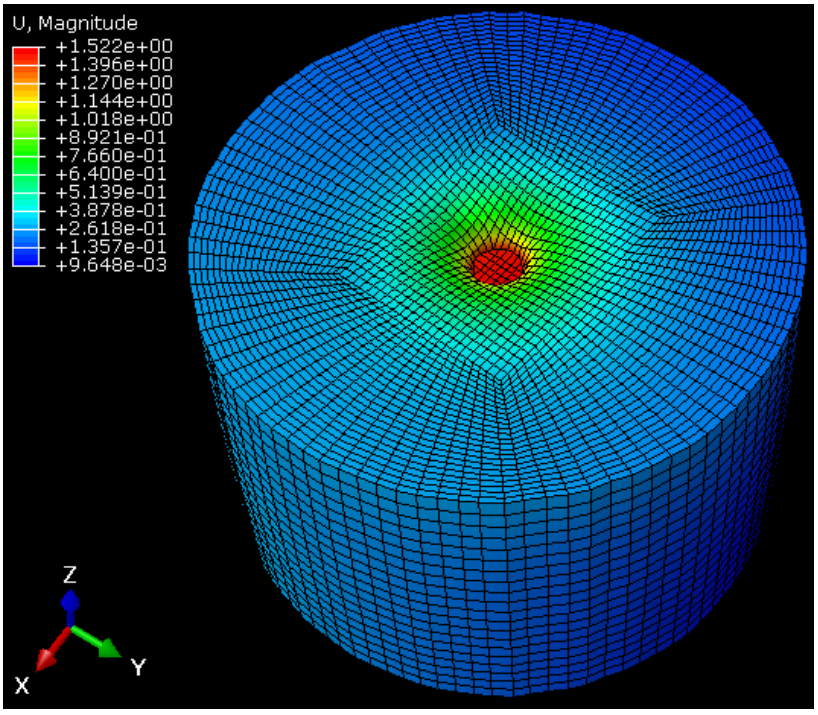

(b)

Figure 5.2: Typical FE model of a lung tissue specimen for simulated indentation. (a): Undeformed FE mesh of the sample where the circular indentation area can be detected on the center of the upper surface. (b): The deformed FE mesh of the sample under 1.5 mm indentation.

5.4 Experiments

5.4.1 Preparation of Lung Tissue Specimens

Thirty lung specimens were resected from different regions of all lobes of several fresh porcine whole lungs acquired from a local abattoir. All of the specimens were resected and tested within 2-4 hrs after sacrificing. All the samples were kept in phosphate buffered saline (PBS) solution until the experiment were conducted. A smooth, homogenous area of lung tissue was selected for indentation and marked to identify the indentation area. The slice thickness at the indentation area was measured with digital calipers and recorded for mesh generation step. Thickness measurements were also conducted at randomly selected points across each tissue specimen to ensure thickness variability was not significant.

5.4.2 Indentation Apparatus

Figure 5.3 depicts a schematic representation of the indentation apparatus used in this study. This system is a custom made computerized electro-mechanical machine which consists of a servo actuator with a controller for tissue actuation, load cell for force measurement and a computer to control and collect the force-displacement profiles. The actuator is a linear servo motor LAL-30 (SMAC, Carlsbad, CA, USA) with a motion range of 25 mm, resolution of 0.5 μm and accuracy of 1 μm. This actuator is controlled by a 6K2 motor controller (Parker Hannifin Corporation, Rhonert Park, CA, USA). As depicted in Figure 5.3, the load cell is mounted underneath a pivoted solid platform which transports the tissue indentation force to the load cell. The actuation and force measurement systems are controlled by a single computer (PC) via a LabVIEW program. For force data acquisition, the load cell signal is first amplified, then sampled at a frequency of 1000 samples/s using an analog input card NI 6020E (National Instruments, Austin, TX, USA). The control program was responsible for preloading the tissue sample, driving the servo motor for tissue indentation using user defined input parameters of a predefined motion profile and finally sampling the force and displacement data.

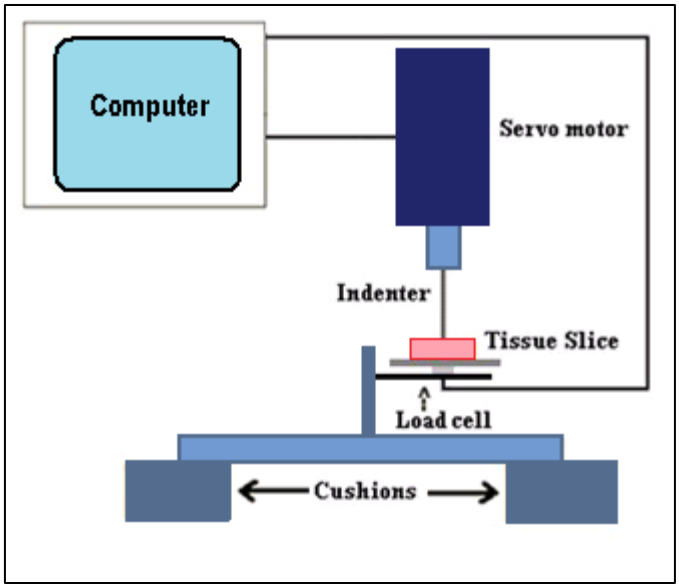

Figure 5.3: Schematic of the measurement system for tissue slice biomechanical parameters. The system consists of a servo motor for programmed indentation profile and a load cell system for force measurement, both connected to a computer for data acquisition and recording.

5.4.3 Indentation Tests

Low frequency Indentation was applied to stimulate tissue samples, collect their response, and measure their biomechanical properties, accordingly. A 1.5 mm diameter plane-ended indenter was used for indenting tissue specimens. Such small size leads to stress propagation through only a small tissue volume around the indenter, hence properly dealing with tissue inhomogeneity.

A larger 5 mm diameter plane-ended indenter was also used through independent set of experiments to validate the uniqueness of the obtained parameters. This larger-tip indenter stimulates a larger area distant from the initially indented area, hence can represent a favorable validation, especially as a different point within the tissue slice is selected for indentation.

For each tissue specimen sufficiently large areas were selected with a minimum diameter of 10 times the indenter diameter. The indenter was then manually positioned such that the indenter's end was almost in contact with the marked indentation area. To establish full contact with the indenter, the tissue was preloaded with a force of 0.1gr. Seven sinusoidal indentation cycles with an amplitude of 1.5 mm and a frequency of 0.1

Hz were applied to each specimen. Up to three indentation tests were performed for each specimen and the smoothest force-displacement curve was selected for further post-processing.

5.5 Results

5.5.1 Optimized Hyperelastic Parameters for Each Model

Figure 5.4(a) demonstrates a typical fitting process for unknown parameters of a hyperelastic model through several iterations. Gradual convergence of the model's unknown parameters from their initial values to the actual values can be observed via convergence of the simulated force-displacement curves to the corresponding experimental curve. Typical final fits for Ogden, Yeoh, and polynomial strain energy models are shown in Figures 5.4(b)-(d), respectively. As it can be observed in these figures a very good final match is typically obtained for all the three hyperelastic models. Table 5.1 summarizes the average performance of the optimization algorithm for the models employed in this study. While all the models satisfy the stopping criteria after an average number of iterations ranging from 9-39, the average values of curve fitting final error range between 2.3% and 6.2% which are sufficiently small. To assess differences of calculated hyperelastic parameters obtained for samples obtained from different lung lobes we performed statistical t-tests. These tests indicate that there are no statistically significant difference between the hyperelastic properties of different lung lobes and regions ($p>0.05$). As such, for each hyperelastic model, the calculated parameter values obtained for all the lung specimens were averaged and their Standard Deviation (STD) were calculated. The average values characterizing hyperelastic properties of lung tissue specimens along with their STD values are presented in Table 5.2.

5.5.2 Results of Uniqueness Validation Tests

As mentioned earlier, a set of several independent experiments were conducted where a different point of previously tested tissue specimens was indented using a considerably larger indenter in order to validate the uniqueness of the optimized parameters. A corresponding set of FE simulations were also performed using the calculated hyperelastic parameters. The simulations were conducted to verify whether they can

accurately predict these indentation experiments performed for the purpose of validation. The resultant force-displacement profiles obtained from simulation were then compared to their corresponding experimental profiles acquired through the validation tests. Figure 5.5(a)-(c) represents typical results obtained for Ogden, Yeoh, and Polynomial hyperelastic models, respectively. The average values of errors obtained from several experiments conducted for this purpose are summarized in Table 5.3. Given that the validation experiments were performed independently using a different indenter tip and on a different point of the specimens, the small differences observed between the two force-displacement curves illustrated for each strain energy model confirm the uniqueness of the optimized parameters obtained with the 1.5 mm-diameter indenter.

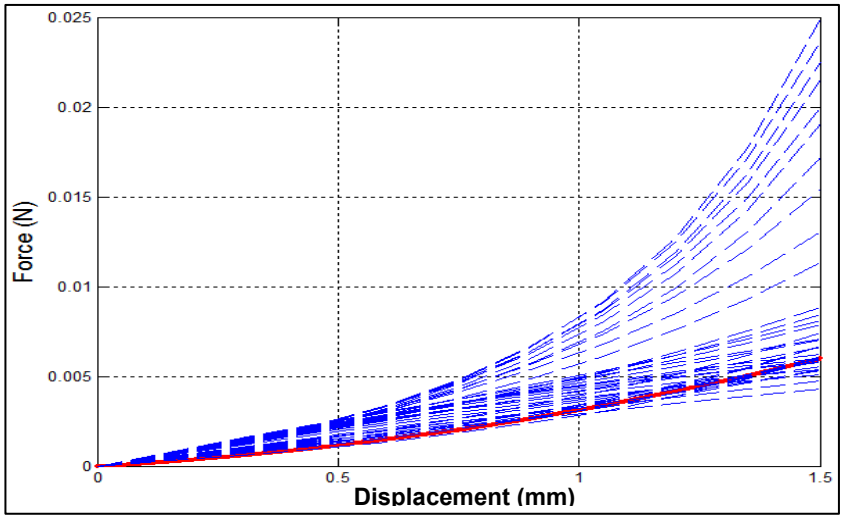

(a)

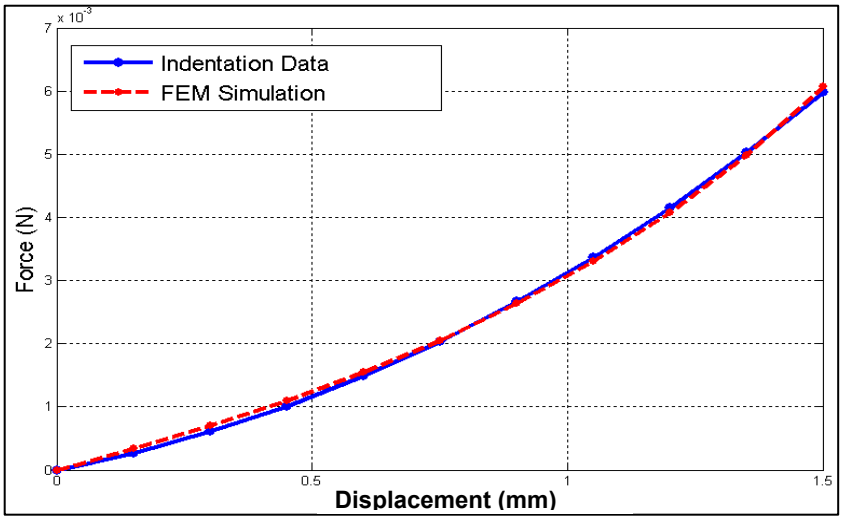

(b)

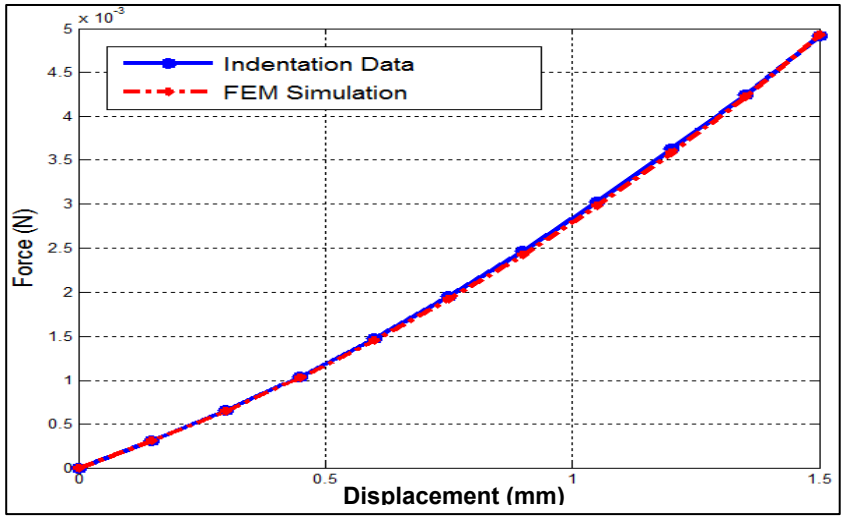

(c)

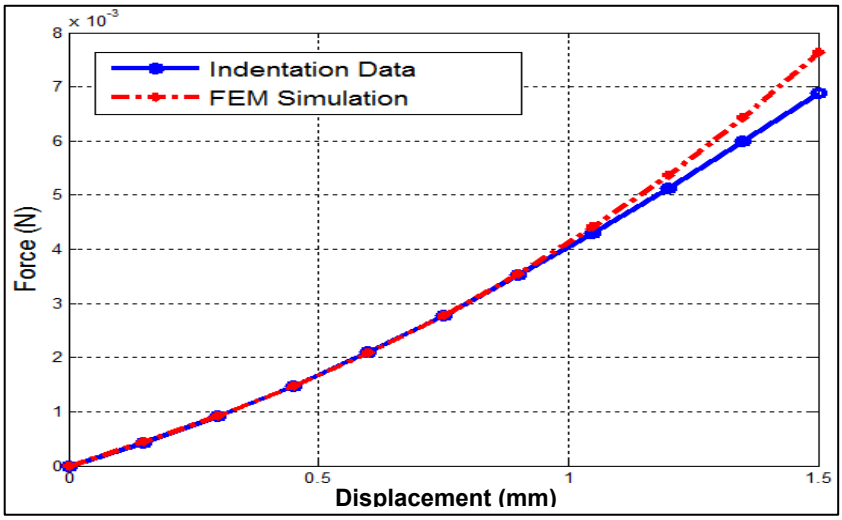

(d)

Figure 5.4: (a): Strain energy models' fitting process through several iterations; typical results obtained after convergence for (b): Ogden, (c):Yeoh, and (d): Polynomial strain energy models.

Table 5.1: Results of the optimization processes summarized for each hyperelastic model; the final error calculated as the average and STD of the absolute differences between the experimental and simulated indentation forces.

Strain Energy Model	*Average and STD number of iterations to converge*	*Average and STD values of final error (%)*
Ogden	39 ± 2	2.36 ± 4.79
Yeoh	12 ± 2	3.67 ± 3.33
Polynomial	9 ± 5	6.28 ± 2.49

Table 5.2: Average and STD values of the hyperelastic models' parameters obtained for the lung specimens. The units for all the parameters (excluding the unitless Ogden α-parameter) are in Pascals (N/m^2).

Strain Energy Model	*Parameter*	*Average ± STD*
Ogden	μ	452.9 ± 59.4
	α	9.5 ± 2.9
Yeoh	C_{10}	194.4 ± 26.4
	C_{20}	257.9 ± 125.8
	C_{30}	0.0033 ± 0.0022
Polynomial	C_{10}	95.8 ± 14.3
	C_{01}	95.8 ± 14.3
	C_{11}	344.3 ± 224.2
	C_{20}	1.19 ± 1.6
	C_{02}	1.19 ± 1.6

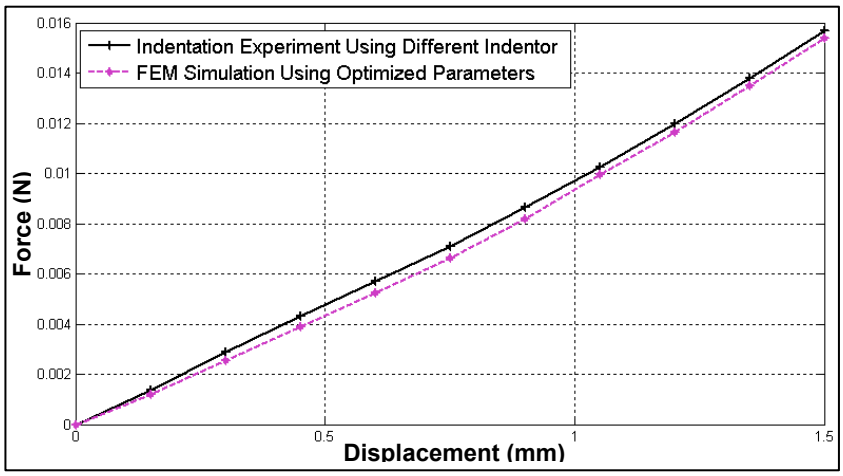

(a)

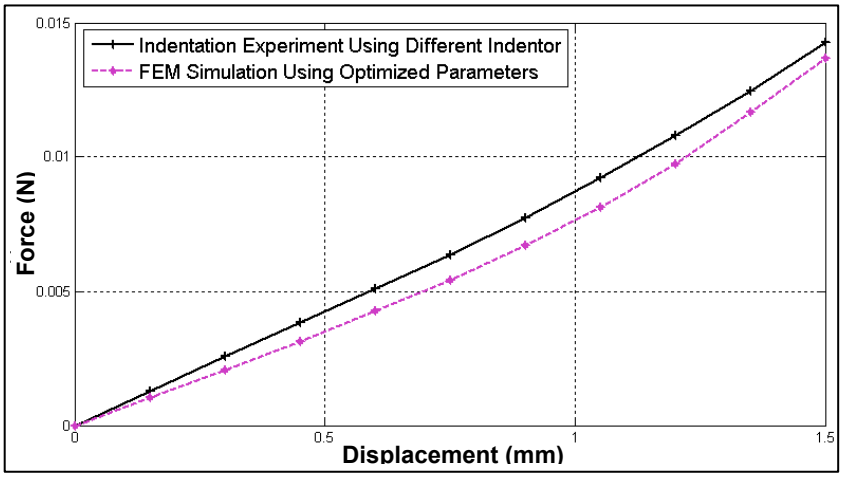

(b)

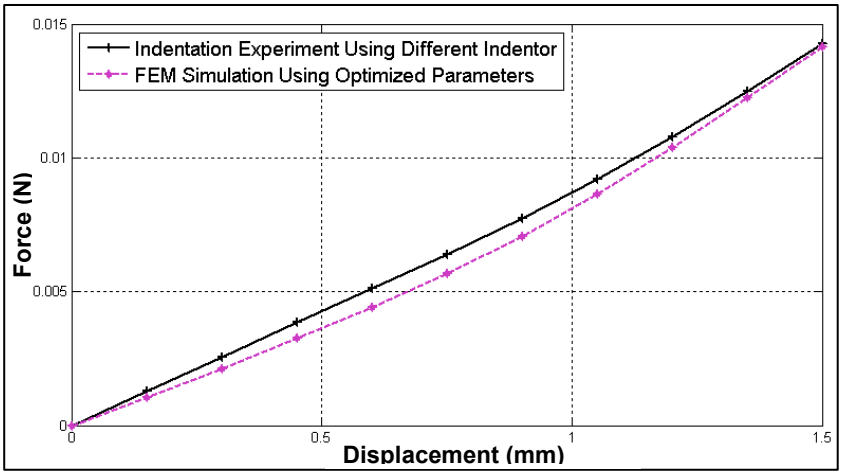

(c)

Figure 5.5: Typical results obtained from the uniqueness validation tests. Each indentation experiment was repeated on a different point of the same tissue sample using a different indenter with a considerably larger tip. Force-displacement curves obtained have been compared with those obtained from FEM simulation using the optimized parameters obtained previously for (a): Ogden, (b):Yeoh, and (c): Polynomial strain energy models.

Table 5.3: Average errors obtained in several experiments conducted for uniqueness validation with the optimized parameters of strain energy models.

Strain Energy Model	*Ogden*	*Yeoh*	*Polynomial*
Average validation error	6.83%	10.24%	10.46%

5.6 Discussion and Conclusion

Hyperelastic parameters of deflated lung tissue were characterized in this chapter using three different strain energy models. This involved an iterative optimization process where the parameters which best fit the experimental data to those obtained from FE simulations were calculated. For this purpose and following a protocol for tissue resection, preparation, and indentation, several tests were performed on various fresh lung specimens using a small-tip indenter. While the amplitude of indentation was 1.5 mm, which translates into 10-30% average strain for 5-15 mm thick slices, indentation stress concentration leads to much higher strains around the indentation region. Observations from FE analysis's performed indicated that the maximum principal strain

reaches as much as 76% in the region underneath the indenter. This ensures sufficiently large loading for probing the tissues' hyperelastic properties. The inverse algorithm's loop converged in reasonable numbers of iterations and with favorably low final errors ranging between 2.3% and 6.2%. This small disagreement between experimental and simulated force-displacement data is due to a number of factors including: 1) small tissue inhomogeneities under indentation area; 2) uncertainties associated with slightly non-smooth and/or slipping boundary conditions at the sample's bottom as well as at the indentation contact area used in the FE analysis; 3) small computational error due to FE meshing, averaging and/or rounding the numeric values, etc.

As the results imply, the Ogden model produced the most accurate outcomes. The Yeoh model was second in terms of accuracy with a slightly higher average error. However, the Yeoh and Poylnomial models outperformed the Ogden model in terms of the required number of iterations due to the high efficiency of the applied slope variation optimization technique. As such, it may be beneficial to select the Yeoh model for characterizing the lung tissue biomechanical properties since it has fairly balanced trade-off between accuracy and speed of convergence. It also has a moderate number of parameters to solve for, hence is easier to interpret. Moreover, the Yeoh model is preferable to the polynomial model due to its independence from the second strain invariant [43]. This is based on the observations that not only the second invariant dependency is hard to measure, but also on the minimal sensitivity of the strain–energy function to modifications in the second invariant in comparison to those of the first invariant. Our results confirm Yeoh's observations in this regard, as overall the Yeoh model produced more accurate fits than the polynomial model.

In order to ensure the uniqueness of the obtained results a set of independent validation tests were performed using a considerably larger indenter tip on different indentation points within each tissue specimen. While the previous small-tip indenter can properly deal with the tissue inhomogeneity, this larger tip indenter results in measuring an average tissue response in a larger area, hence can reliably validate the uniqueness of the previously obtained parameters. The outcomes of the validation tests were very encouraging as they demonstrated the uniqueness of the calculated hyperelastic

parameters. The average indentation errors in these tests ranged from 6.8% to 10.4%. Taking the tissue inhomogeneities across a specimen, slight uncertainties on boundary conditions, as well as possible (low) experimental and computational errors, the errors obtained seem quite reasonable. As such it can be concluded that the obtained results are convincingly reliable, therefore, they can pave the way for more accurate and realistic biomechanical systems for modeling lung tissue behavior under loading in various medical applications.

References

[1] S. F. Altekruse, C. L. Kosary, M. Krapcho, N. Neyman, R. Aminou, W. Waldron, J. Ruhl, N. Howlader, Z. Tatalovich, H. Cho, A. Mariotto, M. P. Eisner, D. R. Lewis, K. Cronin, H. S. Chen, E. J. Feuer, D. G. Stinchcomb, B. K. Edwards, "SEER Cancer Statistics Review, 1975-2007", National Cancer Institute, available at http://seer.cancer.gov/csr/1975_2007/, based on November 2009 SEER data submission, posted to the SEER web site, 2010.

[2] Canadian Cancer Society, "Canadian Cancer Society's Steering Committee: Canadian cancer statistics 2009", Toronto, ISSN: 0835-2976, April 2009.

[3] A. Lin, A. L. Trejos, R. V. Patel, R. A. Malthaner, "Robot-assisted minimally invasive brachytherapy for lung cancer", In Telesurgery, S. Kumar, J. Marescaux (eds), pp. 33-52, Springer-Verlag, Berlin, 2008.

[4] V. W. Ng, J. E. Husband, V.M. Nicolson, I. Minty, A. Bamias, "CT evaluation of treatment response in advanced gastric cancer". Clin Radiol, vol. 51, issue 3, pp. 215-220, 1996.

[5] A. Sadeghi Naini, G. Pierce, T. Y. Lee, R. V. Patel, A. Samani, "CT image construction of a totally deflated lung using deformable model extrapolation", Med. Phys. vol. 38, issue 2, pp. 872-883, 2011.

[6] W. Maurel, Y. Wu, N. M. Thalmann, D. Thalmann, "Biomechanical Models for Soft Tissue Simulation", Springer Berlin Heidelberg, 1998.

[7] M. Bro-Nielsen, "Finite element modeling in medical VR," J. IEEE, vol. 86, no. 3, pp. 490–503, 1998.

[8] S. R. Mousavi, I. Khalaji, A. Sadeghi Naini, K. Raahemifar, A. Samani, "Statistical finite element method for real-time tissue deformation estimation", In Press, Computer Methods in Biomechanics and Biomedical Engineering, 2011.

[9] K. L. Wu, G. L. Jiang, Y. Liao, H. Qian, L. J. Wang, X. L. Fu, S. Zhao, "Three-dimensional conformal radiation therapy for non-small-cell lung cancer: A Phase I/II dose escalation clinical trial", Int. J. Rad. Oncol. Biol. Phys., vol. 57, issue 5, pp. 1336-1344, 2003.

[10] S. Sura, V. Gupta, E. Yorke, A. Jackson, H. Amols, K. E. Rosenzweig, "Intensity-modulated radiation therapy (IMRT) for inoperable non-small cell lung cancer: the Memorial Sloan-Kettering Cancer Center (MSKCC) experience", Radiother. Oncol. vol. 87, issue 1, pp. 17-23, 2008.

[11] M. Hiraoka, Y. Matsuo, K. Takayama, "Stereotactic Body Radiation Therapy for Lung Cancer: Achievements and Perspectives", Jpn. J. Clin. Oncol., vol. 40, issue 9, pp. 846-854, 2010.

[12] H. Nakayama, S. Sugahara, M. Tokita, H. Satoh, K. Tsuboi, S. Ishikawa, K. Tokuuye, "Proton beam therapy for patients with medically inoperable stage I non-small-cell lung cancer at the university of tsukuba", Int. J. Radiat. Oncol. Biol. Phys., vol. 78, issue 2, pp. 467-471, 2010.

[13] J. R. McClelland, J. M. Blackall, S. Tarte, A. C. Chandler, S. Hughes, S. Ahmad, D. B. Landau, D. J. Hawkes, "A continuous 4D motion model from multiple respiratory cycles for use in lung radiotherapy", Med. Phys. vol. 33, issue 9, pp. 3348–3358, 2006.

[14] H. Wang, P. J. Littrup, Y. Duan, Y. Zhang, H. Feng, Z. Nie, "Thoracic masses treated with percutaneous cryotherapy: initial experience with more than 200 procedures", Radiology, vol. 235, issue 1, pp. 289–298, 2005.

[15] O. Maiwand, G. Asimakopoulos, "Cryosurgery for lung cancer: clinical results and technical aspects", Technol. Cancer Res. Treat., vol. 3, pp. 143-150, 2004.

[16] M. C. Ambrogi, P. Dini, F. Melfi, A. Mussi, "Radiofrequency ablation of inoperable non-small cell lung cancer", J. Thorac Oncol., vol. 2, S2-3, 2007.

[17] T. T. Healey, D. E. Dupuy, "Radiofrequency Ablation: a safe and effective treatment in nonoperative patients with early-stage lung cancer", Cancer, vol. 17 - issue 1 – pp. 33-37, 2011.

[18] A. Liu, F. Tendick, K. Cleary, C. Kaufmann, "A survey of surgical simulation: applications, technology, and education", Pres. Teleop. Virt. Environ., vol. 12, pp. 599-614, 2003.

[19] A. J. Carpenter, S. C. Yang, P. N. Uhlig, Y. L. Colson, "Envisioning simulation in the future of thoracic surgical education", J. Thorac. Cardiovasc. Surg., vol. 135, pp. 477-484, 2008.

[20] R. Kneebone, "Evaluating Clinical Simulations for Learning Procedural Skills: A Theory-Based Approach", Academic Medicine, vol. 80, issue 6, pp. 549-553, 2005.

[21] R. Playter1, M. Raibert, "A virtual surgery simulator using advanced haptic feedback", Minim. Invasive Ther. Allied Tech, vol. 6, issue 2, pp. 117-121, 1997.

[22] Y. Fung, "Biomechanics Mechanical Properties of Living Tissues", Springer, New York, 1993.

[23] Q. Grimal, B. A. Gama, S. Naili, A. Watzky, J. W. Gillespie, "Finite element study of high-speed blunt impact on thorax: linear elastic considerations", Int. J. Impact Eng., vol. 30, issue 6, pp. 665-683, 2004.

[24] T. Zhang, N. P. Orton, T. Rockwell Mackie, and B. R. Paliwal, "Technical note: a novel boundary condition using contact elements for finite element based deformable image registration", Med. Phys., vol. 31, pp. 2412-5, 2004.

[25] A. P. Santhanam, C. Imielinska, P. Davenport, P. Kupelian, and J. P. Rolland, "Modeling Real-Time 3-D Lung Deformations for Medical Visualization", IEEE Trans. Info. Tech. Biomed., vol. 12, issue. 2, pp. 257-270, 2008.

[26] R. Werner, J. Ehrhardt, R. Schmidt, and H. Handels, "Modeling respiratory lung motion: A biophysical approach using finite element methods",Proc. SPIE 6916, 69160N, 2008.

[27] A. Al-Mayah, J. Moseley, and K. K. Brock, “Contact surface and material nonlinearity modeling of human lungs”, Phys. Med. Biol. vol. 53, pp. 305-17, 2008.

[28] Y. J. Zeng, D. Yager, Y. C. Fung, “Measurement of the mechanical properties of the human lung tissue”, J. Biomech. Eng., vol. 109, issue 2, pp. 169-74, 1987.

[29] S. J. Lai-Fook, R. E. Hyatt, “Effects of age on elastic moduli of human lungs”, J. Appl. Physiol., vol. 89, pp. 163–168, 2000.

[30] K. P. McGee, R. D. Hubmayr, D. Levin, R. L. Ehman, “Feasibility of quantifying the mechanical properties of lung parenchyma in a small-animal model using (1)H magnetic resonance elastography (MRE)”, J. Magn. Reson. Imaging, vol. 29, issue 4, pp. 838-45, 2009.

[31] K. O. Mckay, B. R. Wiggs, P. D. Pare, And R. D. Kamm, “Zero-stress state of intra- and extraparenchymal airways from human, pig, rabbit, and sheep lung”, J. Appl. Physiol., vol. 92, pp. 1261-1266, 2002.

[32] X. Zhang, B. Qiang, R.D. Hubmayr, M.W. Urban, R. Kinnick, J. F. Greenleaf, “Noninvasive ultrasound image guided surface wave method for measuring the wave speed and estimating the elasticity of lungs: A feasibility study”, Ultrasonics, vol. 51, issue 3, pp. 289-295, 2011.

[33] W C. Li, M. H. Yu, M. H. Zhang, H. Q. Wang, G. M. Xi, B. C. Yao, Z. H. Deng, Y. J. Zeng, “Biomechanical properties of ascending aorta and pulmonary trunk in pigs and humans”, Xenotransplantation, vol. 15, issue 6, pp.384-9, 2008.

[34] P. B. Matthews, A. N. Azadani, C. S. Jhun, L. Ge, T. S. Guy, J. M. Guccione, E. E. Tseng, “Comparison of Porcine Pulmonary and Aortic Root Material Properties”, The Annals of Thoracic Surgery, vol. 89, issue 6, pp. 1981-1988, 2010.

[35] A. Sadeghi Naini, R. V. Patel, A. Samani, “CT enhanced ultrasound image of a totally deflated lung for image-guided minimally invasive tumor ablative procedures“, IEEE Trans. Biomed. Eng., vol. 57, issue 10, pp. 2627-2630, 2010.

[36] G. Pierce, K. Wang, S. Gaede, J. Battista, T. Y. Lee, “The effect of an inconsistent breathing amplitude on the relationship between an external marker and internal lung deformation in a porcine model”, Med. Phys. vol. 37, issue 11, pp. 5951-60, 2010.

[37] R. P. Dickson, D. L. Hotchkin, W. J. Lamm, C. Hinkson, “A porcine model for initial surge mechanical ventilator assessment and evaluation of two limited-function ventilators”, Crit. Care. Med., vol. 39, issue 3, pp. 527-532, 2011.

[38] A. Sadeghi Naini, T. Y. Lee, R. V. Patel, A. Samani, “Estimation of lung’s air volume and its variations throughout respiratory CT image sequences”, IEEE Trans. Biomed. Eng., vol. 58, issue 1, pp. 152-158, 2011.

[39] J. O'Hagan, A. Samani, “Measurement of the hyperelastic properties of tissue slices with tumour inclusion”, Phys. Med. Biol., vol. (53), pp. 7087-7106,

2008.

[40] P. Knupp, S. Steinberg, “Fundamentals of grid generation”, CRC Press, Boca Raton, Florida, 1993.

[41] M. Fornefett, K. Rohr, H. Stiehl, “Radial basis functions with compact support for elastic registration of medical images”, Image and Vision Computing, vol. 19, issue 1, pp. 87-96, 2001.

[42] J. Nelder, R. Mead, “A simplex method for function minimization”, The Computer Journal vol. 7, pp. 308-313, 1965.

[43] O. Yeoh, “Some forms of the strain energy function for rubber”, Rubber Chem. Technol., vol. 66, pp. 754–71, 1993.

Chapter 6

Effects of Geometry Simplification on Biomechanical Models of the Lung

The material presented in this chapter has been published in Proc. of SPIE Med. Imaging 2011, Orlando, Florida, USA, 7964: 79642F (2011).[*]

6.1 Introduction

PREDICTING tumor motion due to tissue deformation caused by anatomical contact forces and needle insertion requires tissue biomechanical modeling, as described earlier. Finite Element Method (FEM) is the technique of choice for biomechanical modeling in many biomedical applications [1-3]. One critical step in FEM is geometry extraction and Finite Element (FE) meshing. This is often a very tedious step, especially when a complex geometry such as the lung's with all airway details is involved. In addition, FEM suffers from being excessively time consuming, especially when it involves more complex loading and nonlinear tissue models. As such, it is frequently attempted to simplify the FE model to reduce its time and memory complexity as long as its accuracy is not compromised. One effective way to reduce the complexity of an FE

[*] © 2011 Society of Photo-Optical Instrumentation Engineers (SPIE). This modified version has been reprinted, with permission, from A. Sadeghi Naini, R.V. Patel, and A. Samani, "Effects of deflated lung's geometry simplifications on the biomechanical model of its tumor motion: a phantom study", Proceedings of SPIE Medical Imaging 2011: Visualization, Image-Guided Procedures, and Modeling, March 2011.

model is simplifying its geometry by omitting fine details a complex geometry may involve. The simplification, however, should be performed with caution since over simplification may result in a significant drop in the model's accuracy.

In this chapter, the influence of a deflated lung's geometry simplification on the accuracy of its tumor motion prediction is investigated. Tumor's motion is predicted by tissue biomechanical modeling using FEM as described in Section 6.2. Here, the simplification is performed via neglecting the airways inside the lung. As described in Section 6.3, several numerical experiments were conducted with different tumor and airway sizes and locations using both elastic and hyperelastic material models. Sensitivity of the tumor's motion prediction accuracy to the geometry simplification was then presented as a function of airways' size relative to the tumor's size. The results obtained are then discussed and concluded in section 6.4.

6.2 Methods

6.2.1 Finite Element Analysis

FE analysis and modeling has been used for many years as a numerical technique for systems of differential equations in various engineering and sciences applications. More recently, these techniques have been utilized in biomedical engineering applications. This includes applications where modeling parts of the human body is involved using realistic biomechanical data of tissues/materials [1-3]. The basic concept of FEM is discretizing the object into smaller "Elements" of finite dimensions. The process of this dicretization is referred to as mesh generation. The original object is then considered as an assembly of these elements connected at a finite number of joints called "Nodes". The properties of the elements are formulated and combined to predict the response of the entire body. The equations of equilibrium for the entire structure or body are obtained by combining the equilibrium equations of each element such that the continuity is ensured at each node. The necessary "Boundary conditions" are imposed and the equations of equilibrium are solved to obtain the required variables such as displacement, strain and stress. In addition to geometry, boundary conditions and elements' type, proper material models is also required for an accurate FE model. Moreover, a precise FE model should take advantage

of a suitable meshing technique in order to discretize the geometry in a consistent manner.

6.2.2 Mesh Generation

As mentioned earlier, mesh generation is a critical step in the FE analysis process. The mesh affects the accuracy, convergence and speed of the computational process. As such, a more precise and efficient FE mesh would result in a more accurate and faster solution. It should be noted that suitable geometry simplification plays a major role in obtaining a proper FE model for a specific application. Simplifications usually involve elimination of less important details that unnecessarily increase the meshing complexity. There are several techniques for mesh generation applied in different applications [4].Transfinite Interpolation (TFI), which is also known as the standard method of algebraic mesh generation, is one of the most popular techniques for mesh generation. TFI was first introduced by Gordon and Hall [5] and have been then extensively developed [6] because of its rapid computation and high degrees of control over the nodal location. In this method a logical space mesh (a meshed unit square or cube) is mapped to the physical space mesh using an interpolation function. The idea of using interpolation for mesh generation stems from the fact that in most cases, the mesh nodal coordinates are known on all of the object's boundaries, and the problem involves propagating the boundary nodal configuration into the interior of the domain using blending functions. More details on this technique can be found in [7].

6.3 Experiments and Results

Several numerical experiments were conducted on deflated lung phantoms. The phantoms are three-dimensional (3D) blocks with dimensions of 440mm × 640mm × 100mm (Figure 6.1). The reason for choosing such a phantom shape was the fact that the lower part of the lung which undergoes the diaphragm contact forces resembles a block. The contact surface of the lung and diaphragm, although not planar, is close to planar. Hence a block shape phantom can reasonably model this region of interest. The simplified reference phantom contained no airways and has a cylindrical shape tumor inclusion located at the center of the volume (Figure 6.1 (a)). The other phantom

contained two airways located below the inclusion (Figure 6.1 (b)). Each airway was surrounded with a thin ring which is stiffer than normal tissue to mimic the airway tubes in the lung. The position of each airway was selected randomly in each phantom. Each phantom was meshed with 8-node hexahedral elements using the TFI technique. The meshing scheme for both cases is demonstrated in Figure 6.1.

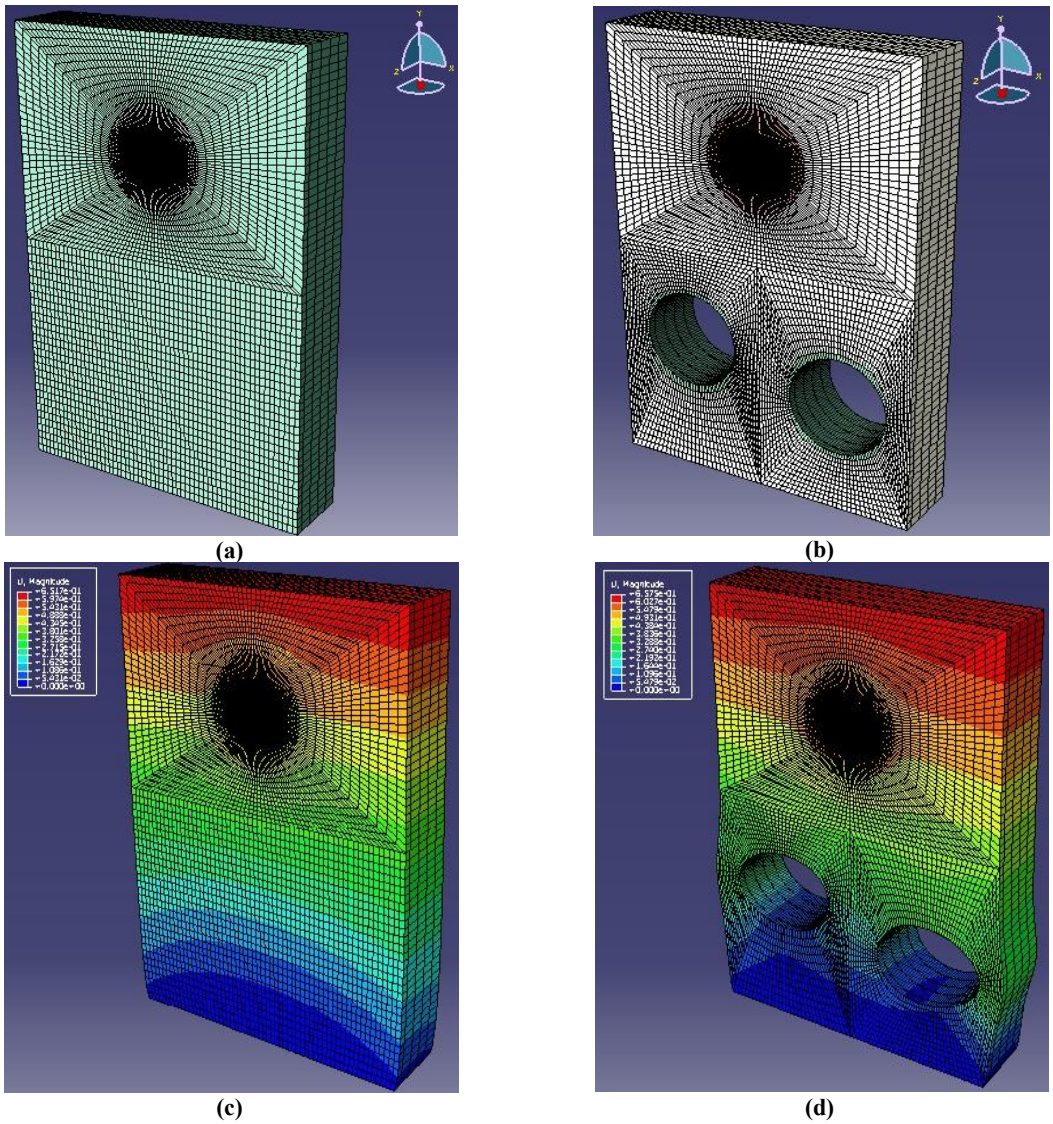

Figure 6.1: Finite Element models applied for the numerical phantom study; (a): Undeformed shape of the simplified (reference) phantom with no airways, (b) Undeformed shape of a phantom with two airways with the same size as the inclusion size, (c) displacement field overlaid on the deformed shape of the reference phantom and (d): displacement field overlaid on the deformed shape of the phantom shown in (b).

Both linear elastic and nonlinear hyperelastic material models were used for the lung's normal tissue in this study. A young's modulus of 3.74 KPa was used for the normal tissue in the linear elastic model with a Poissons' ratio of 0.49 [8]. For the hyperelastic model, the Marlow model was used that best fitted the test data reported in [8] for the lung. A Poissons' ratio of 0.49 was used in this model. Linear elastic models with Young's moduli of 18.7 KPa and 37.4 KPa were used for the airways' walls and inclusion, respectively with a Poisson's ratio of 0.49.

Each experiment was initiated by applying proper contact forces on the top surface of the phantom such that downward displacement of the top surface was about 10% of the phantom height. This mimics the maximum surface displacement of the deflated lung due to diaphragm motion during respiration. Several experiments were conducted using 5 different inclusion sizes with 15 different airway sizes for each inclusion size. The airways sizes in different experiment sets varied between 10% and 150% of the inclusion size with an increment step of 10%. After applying contact forces in each experiment, the deformation model was calculated by FEM using ABAQUS software (D S Simulia. © Dassault Systèmes, 2004, 2011). In each set of experiments with a specific inclusion size, tumors nodal displacements were obtained in both the reference phantom and the simplified phantoms. The magnitude of differences between the displacements of each reference phantom and the simplified phantom obtained by omitting the airways was calculated. The relative differences of the tumor's nodal displacements between each two cases were obtained by dividing the displacement differences by the tumor's diameter. The average values and standard deviation of absolute and relative differences of the tumor's nodal displacements obtained from several experiments conducted on different tumor and airways sizes using both linear elastic and nonlinear hyperelastic material models are given in Table 1 and Figure 2.

As suggested by the results obtained for both material models, as long as the airways size does not exceed the tumor size, the tumor displacement due to surface contact forces estimated by the FEM is not very sensitive to the geometry simplification. In this case the maximum average error is 0.21±0.18mm (1.87±1.13% of the average tumor's diameter) which is negligible. It can be concluded that small airways with a size up to the tumor

size can be omitted in the deflated lung's FE model without imposing significant error in the tumor motion estimation. Beyond this airways size, the tumor's motion estimation error increases with a relatively considerable rate, hence it cannot be ignored. Comparing the results corresponding to the linear elastic and nonlinear hyperelastic material models shows that larger errors were most frequently produced using the hyperelastic material model. This indicates that the nonlinear material model is more sensitive to the geometry simplification. Given that a nonlinear hyperelastic material model is a better representative of soft tissue biomechanical properties, its corresponding estimated errors are more reliable.

Table 6.1: Results of numerical phantom studies: Absolute and relative difference of inclusion's nodal displacements between the cases where the airways were considered and omitted in the Finite Element model. The experiments were conducted using several sizes of inclusions; mean and standard deviation values of the obtained results are given in the table.

Experiments set	Relative size of airways diameter to the inclusion diameter	Average difference of inclusion's nodal displacements		Average relative difference of inclusion's nodal displacements to the inclusion diameter	
		Elastic soft tissue model	Hyperelastic soft tissue model	Elastic soft tissue model	Hyperelastic soft tissue model
1	**10%**	0.03±0.00mm	0.04±0.00mm	0.37±0.11%	0.47±0.11%
2	**20%**	0.04±0.01mm	0.06±0.01mm	0.45±0.09%	0.68±0.23%
3	**30%**	0.05±0.01mm	0.08±0.01mm	0.56±0.11%	0.79±0.12%
4	**40%**	0.04±0.0mm	0.10±0.03mm	0.50±0.17%	1.06±0.20%
5	**50%**	0.04±0.01mm	0.09±0.01mm	0.47±0.27%	0.96±0.19%
6	**60%**	0.04±0.01mm	0.10±0.03mm	0.45±0.25%	1.06±0.28%
7	**70%**	0.05±0.02mm	0.09±0.03mm	0.51±0.20%	1.02±0.43%
8	**80%**	0.07±0.06mm	0.08±0.02mm	0.65±0.38%	0.96±0.42%
9	**90%**	0.12±0.10mm	0.08±0.03mm	1.05±0.74%	0.96±0.62%
10	**100%**	0.15±0.16mm	0.21±0.18mm	1.24±1.05%	1.87±1.13%
11	**110%**	0.22±0.22mm	0.31±0.41mm	2.01±1.80%	2.61±2.79%
12	**120%**	0.19±0.13mm	0.29±0.36mm	1.93±1.26%	2.68±2.83%
13	**130%**	0.30±0.26mm	0.51±0.66mm	2.80±2.21%	4.60±5.27%
14	**140%**	0.45±0.50mm	0.47±0.53mm	4.12±3.97%	4.38±4.16%
15	**150%**	0.68±0.58mm	0.69±0.89mm	6.35±4.72%	6.17±7.26%

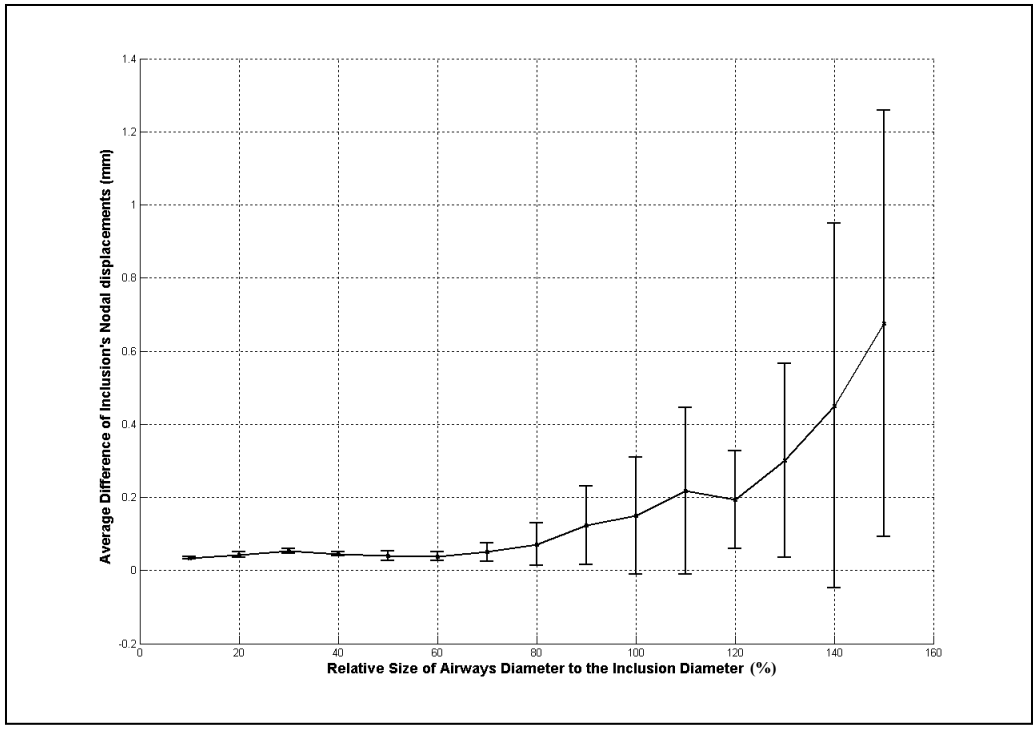

(a)

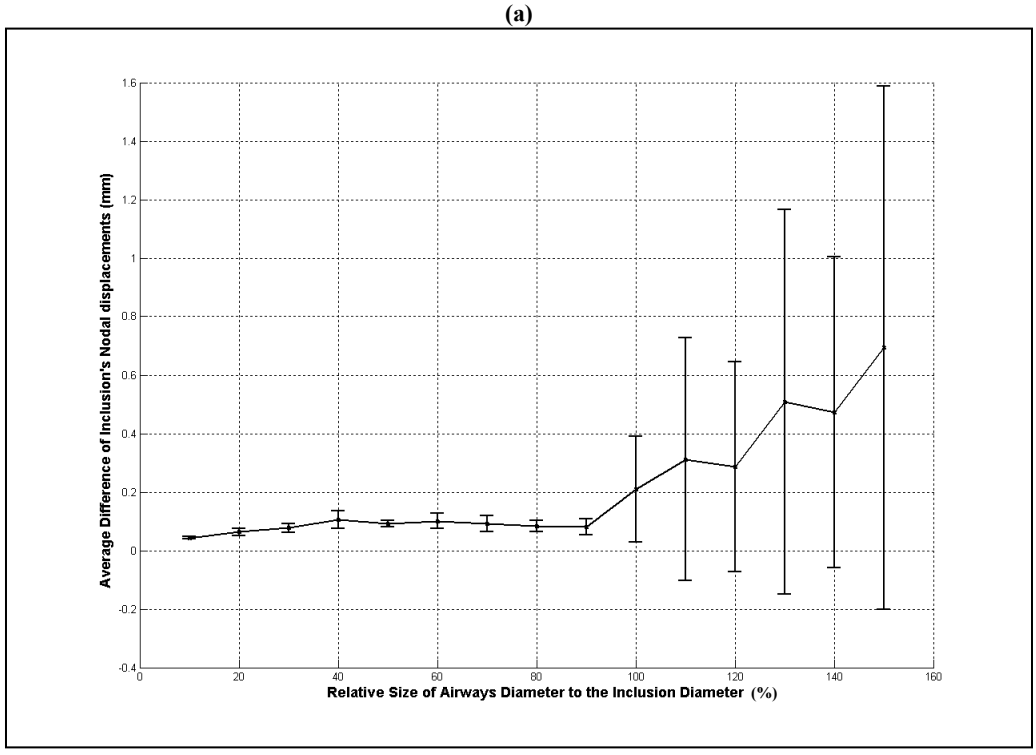

(b)

Figure 6.2: Average differences of inclusion's nodal displacement between results of Finite Element models of simplified (reference) and non-simplified phantoms as a function of airways relative diameter; the experiments were conducted using several sizes of inclusions; mean (×) and standard deviation (bars) values of the results obtained are demonstrated. Results are given using FE models with (a): Elastic soft tissue model and (b): Hyperelastic soft tissue model.

6.4 Discussion and Conclusion

In this chapter, the possibility of simplifying a deflated lung's geometry without compromising the accuracy of the finite element model used for its tumor motion estimation was investigated. Several numerical experiments were conducted on deflated lung's phantoms with different sizes of inclusion. Each set of experiments included one set of phantoms were the airways were considered while the other one was a reference phantom where the airways were omitted. Results obtained from the experiments conducted using different sizes of tumor and airways were assessed. For this assessment, the sensitivity of the tumor's motion prediction accuracy to the geometry simplification was presented as a function of airways' size relative to the tumor's size. Final results obtained for both linear elastic and nonlinear hyperelastic material models suggest that the tumor displacement due to surface contact forces estimated by the FEM is not very sensitive to the geometry simplification of omitting airways as long as the airways size does not exceed the tumor size. While the phantom's geometry is simple compared to the lung's actual geometry, its mechanical properties are realistic and the obtained results provide important insight on how a time consuming FE analysis of a deflated lung deformation can be simplified without compromising the accuracy of its tumor motion prediction. Such simplification can facilitate fast prediction of tumor location during a lung tumor ablative procedure such as Low Dose Rate (LDR) brachytherapy. This fast prediction is very important for developing a clinical lung brachytherapy system.

References

[1] M. Bro-Nielsen, “Finite element modeling in medical VR”, J. IEEE, vol. 86, issue 3, pp. 490-503, 1998.

[2] A. Horsch, T. M. Deserno, H. Handels, H. P. Meinzer, T. Tolxdorff, “Finite Element Simulation of Moving Targets in Radio Therapy”, Informatik aktuell, vol. 12, pp. 353-357, 2007.

[3] A. P. Santhanam, C. Imielinska, P. Davenport, P. Kupelian, J. P. Rolland, “Modeling real-time 3-D lung deformations for medical visualization”, IEEE Trans. on Inform. Tech. in Biomed., vol. 12, issue 2, pp. 257-270, 2008.

[4] P. M. Knupp, S. Steinberg, “Fundamentals of grid generation”, CRC Press, 1993.

[5] W. J. Gordon, C. A. Hall, “Construction of curve linear coordinate systems and applications to mesh generation”, Int. J. Numer. Methods in Eng., vol. 7, pp. 461-477, 1973.

[6] Y. C. Liou, Y. N. Jeng, “A transfinite interpolation method of grid generation based on multipoints”, Journal of Scientific Computing, vol. 13, issue 1, pp. 105-114, 1998.

[7] L. E. Eriksson, “Practical three-dimensional mesh generation using transfinite interpolation”, J. Sci. Stat. Comput., vol. 6, issue 3, pp. 721-741, 1985.

[8] A. Al-Mayah, J. Moseley, M. Velec, K. K. Brock, “Sliding characteristic and material compressibility of human lung: parametric study and verification”, Med. Phys., vol. 36, issue 10, pp. 4625-33, 2009.

Chapter 7

Conclusion and Future Work

7.1 Conclusion

DIFFERENT types of tissue motion and deformation in the lung while it undergoes minimally invasive tumor ablative procedures were investigated and modeled in this study. As described in Chapter 1, the motivation behind such modeling is based on the fact that the lung is the most deformable organ within the body. If not properly taken into account and consequently compensated for, this property can significantly hamper the accuracy of procedures pre-planned for targeting lung cancer. For example, it may result in targeting an area outside the aimed tumor region and/or lead to significant areas of radiation over- and/or under-dosage.

Based on the source and stage in a tumor ablative procedure, two types of major motions and deformations were recognized and investigated in this thesis. The first one was the deformation encountered only once in procedures where the lung is totally deflated before starting the operation. A consequence of this deflation is that pre-operative lung images acquired during respiration become inaccurate for pre- and/or intra-operative tasks. The second major type of lung deformation tackled in this thesis is the one that has a continuous effect during the procedure, and occurs due to anatomical respiratory contact forces or needle insertion. This type of tissue deformation can be predicted effectively and accurately using tissue biomechanical modeling. Two major

prerequisites of such modeling are: 1) having the biomechanical parameters of the lung soft tissue; 2) generating the lung's finite element mesh which involves acceptable geometry simplification. The investigations conducted in this study were presented in five chapters. The main research contributions and results described in each chapter are summarized below.

7.1.1 Chapter 2: Lung's Air Volume Estimation during Respiration

A novel concept of image sequence analysis was introduced in this chapter to obtain appropriate lower and upper threshold bounds for threshold-based image segmentation. This concept is equally useful for segmenting both static and dynamic image sequences. In this study, the concept was utilized to estimate the lung's air volume and its variations in respiratory Computed Tomography (CT) image sequences using combined sequence histogram and satisfying the lung's air mass conservation as well as tissue incompressibility principles. The results obtained from the experiments conducted on static breath-hold CT images as well as free-breasting four-dimensional CT (4D-CT) image indicated a very favorable ability of the method for estimating the lung's air volume and its variations throughout a respiratory image sequence. A comparison between the two sets of obtained results shows that the proposed optimization thresholding technique outperforms the maximum peak separation thresholding when used in the lung's air volume estimation. Considering its favorable capabilities, this technique can be used effectively in clinical applications such as Low Dose Rate (LDR) lung brachytherapy where the lung's air volume and/or its variations in a respiratory sequence are needed. The concept of finding the optimum segmentation threshold values from an image sequence's combined histogram introduced in this work can also be used in other biomedical applications, *e.g.*, ventricle's ejection fraction, where important physiological parameters need to be extracted.

7.1.2 Chapter 3: CT Image Construction of a Totally Deflated lung

In this Chapter, a new technique was introduced to construct CT image of a totally deflated lung using the lung's free-breathing 4D-CT image sequence acquired pre-operatively. The proposed technique involves determining the lung tissue deformations

that occur during the respiratory cycles. Each deformation is presented by means of free-form deformable registration parameters. This step is followed by formulating the obtained registration parameters as functions of the lung's air volume variations. The image construction pipeline estimates the lung's air volume automatically in each image using the technique proposed in Chapter 2; hence there is no need to use any external marker for position tracking throughout the respiratory cycle. The fitted deformation function is then used to extrapolate parameters of tissue deformation that would occur as a result of total deflation of the lung. The predicted deformation is finally used to construct a new CT image corresponding to the lung in its deflated state from one of the lung's pre-operative images that was used as a reference image. Results obtained from conducted *ex vivo* lung experiments were very encouraging as they demonstrated the technique's capability of constructing accurate and reliable CT image of the deflated lung. Such a reliable constructed CT image is suitable in image-guided procedures for pre-operative tasks such as treatment planning. This technique can also be applied in intra-operative tasks, such as tumor localization and fusing with real time navigation data. These intra-operative applications involve image registration with intra-operative ultrasound (US) images in order to enhance their poor quality.

7.1.3 Chapter 4: Intra-operative US Image Enhancement

An image enhancement pipeline was introduced in this chapter to improve the quality of deflated lung's intra-operative US images. The pipeline uses higher quality CT image of a deflated lung constructed pre-operatively, in order to enhance the US quality and its usability. The core part of the pipeline consists of two simultaneous registration processes with exchanged fixed and moving images. The first process determines the optimum orientation and position of the US slice within the CT volume, and the second improves its quality. The output is a CT enhanced US image of a totally deflated lung oriented and positioned accurately within its pre-operative CT counterpart. The results obtained from the conducted experiments were promising both in terms of registration accuracy and image quality improvement. The results also confirmed that significant image quality improvement can be achieved in a near real-time fashion. As such, this work may be

regarded as an important step for clinical implementation of lung's image-guided minimally invasive tumor ablative procedures.

7.1.4 Chapter 5: Characterizing Lung's Hyperelastic Properties

Hyperelastic parameters of lung's soft tissue were characterized in this chapter using three different strain energy models. This involved an iterative process were the optimum parameters which best fit the experimental data to those obtained from Finite Element (FE) simulations were calculated. For this purpose and following a strict protocol for tissue resection, preparation, dozens of lung tissue specimens were pre-processed for indentation tests. Indentation experiments conducted on of lung tissue samples followed by inverse numerical simulations performed led to accurate measurement of lung tissue hyperelastic parameters. The inverse algorithm converged in reasonable numbers of iterations and with favorably low final errors. Tests were performed to validate the results which demonstrated the uniqueness and accuracy of the obtained parameters. As such, it was concluded that the results are convincingly reliable, and hence can be applied for more accurate and realistic biomechanical modeling of lung tissue behavior under loading in many medical applications.

7.1.5 Chapter 6: Effect of Geometry Simplification

In this chapter, the possibility of simplifying a deflated lung's geometry without compromising the accuracy of the finite element model used for its tumor motion estimation was investigated. Several numerical experiments were conducted on deflated lung's phantoms with different sizes of inclusion. Results obtained from the experiments conducted using different sizes of tumor and airways were assessed. For this assessment, the sensitivity of the tumor's motion prediction accuracy to the geometry simplification was presented as a function of airways' size relative to the tumor's size. Final results obtained for both linear elastic and nonlinear hyperelastic material models suggest that the tumor displacement due to surface contact forces estimated by the Finite Element Method (FEM) is not very sensitive to the geometry simplification of omitting airways as long as the airways size does not exceed the tumor size. Such simplification can facilitate fast prediction of tumor location during a lung tumor ablative procedure such as LDR

brachytherapy. The findings of this investigation have paved the way for biomechanical modeling of the lung under contact force or needle insertion in future studies.

7.2 Future Directions

Results reported in Chapter 2, Chapter 3 and Chapter 4 proved the principles and demonstrated the feasibility of the entire imaging framework proposed for image-guided minimally invasive tumor ablative procedures such as LDR lung brachytherapy. However, more *in vivo* experiments are required before the protocol can be recommended for clinical applications. Future studies may involve conducting ethically approved *in vivo* experiments on animal models and human subjects to demonstrate the reliability of these techniques in the clinic. One other interesting branch for future investigations includes implementation of these methods on Graphics Processing Unit (GPU) processors to achieve near real-time responses from the proposed techniques.

As mentioned before, the information reported in Chapters 5 and Chapter 6 have paved the way for future research efforts to investigate intra-operative lung's needle insertion or contact force related deformations via biomechanical modeling. Such modeling, which is frequently performed using the finite element method, can accurately characterize such continuous and complex deformations. Defining such accurate models requires extensive amounts of information such as the lung geometry, boundary conditions, material models, proper FE meshing, etc. The CT construction technique proposed in Chapter 3 can be used efficiently to extract the deflated lung geometry pre-operatively. The data presented in Chapter 5 can be reliably used to model the hyperelastic properties of the lung's tissue in such models, while the results presented in Chapter 6 provide important insight on how a time consuming FE analysis of a deflated lung deformation can be simplified without compromising the accuracy of its tumor motion prediction. Figure 7.1 illustrates the preliminarily the results of a lung biomechanical model. This model has been developed through an ongoing project in our research group for modeling lung tissue deformation undergoing anatomical respiratory contact forces.

One major practical challenge in biomechanical modeling of the lung via the finite element method is that the FEM suffers from being excessively time consuming, especially with more complex and accurate nonlinear tissue models. This issue can be addressed in future studies through a Statistical FEM (SFEM) briefly described in Chapter 1. SFEM has been recently proposed and developed in our research group by Mousavi *et al.* for fast and accurate biomechanical modeling of soft tissue. This technique is both highly accurate and very fast such that each analysis takes less than 0.1sec on a regular desktop computer irrespective of the model's complexity. This technique is ideal for the mechanical analysis of a set of objects that have similar overall geometry, *e.g.,* lung shape of various individuals. The method assumes that conventional

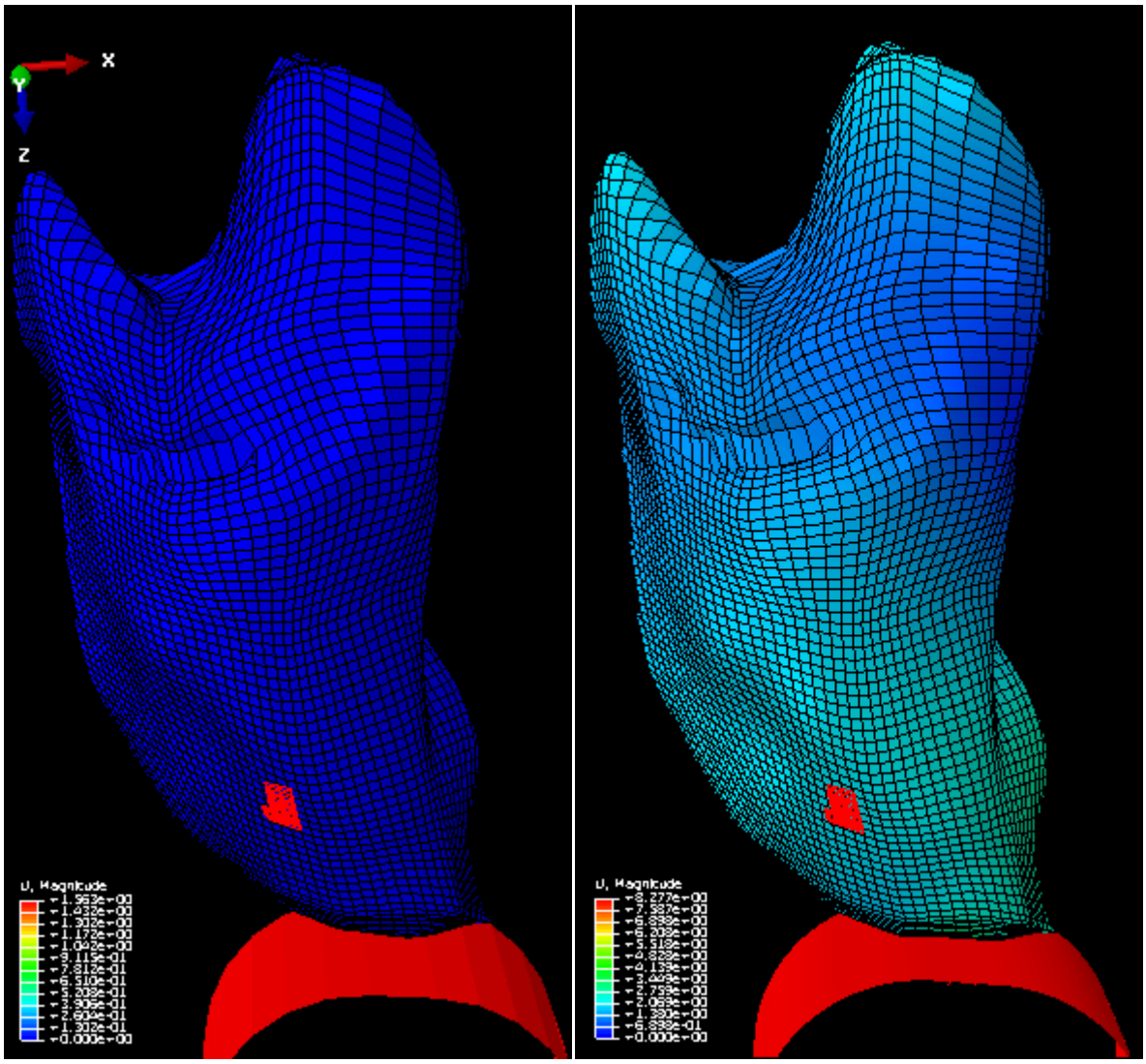

(a) **(b)**

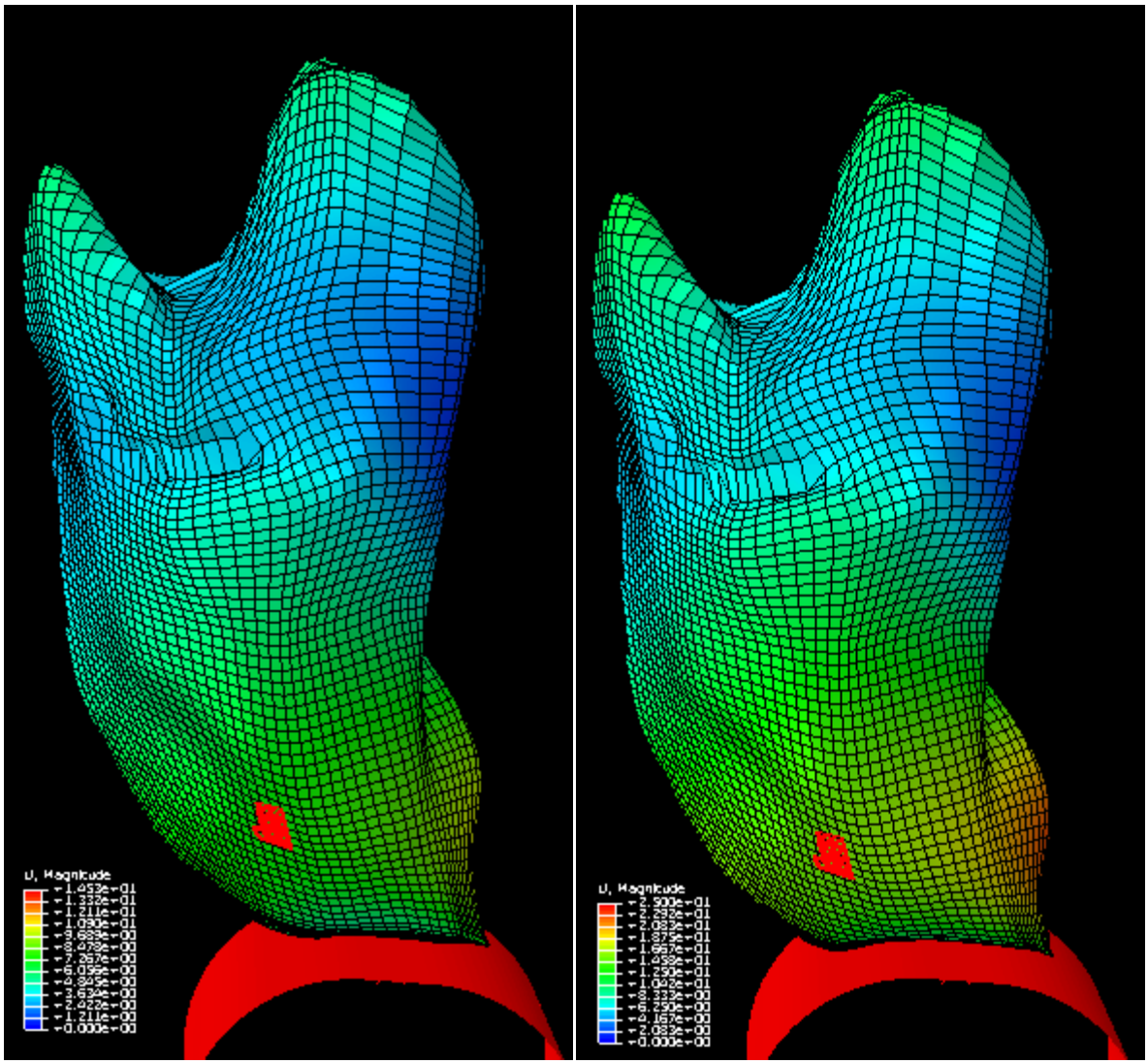

(c) (d)

Figure 7.1: Preliminary results obtained from the lung biomechanical model developed for simulating the lung tissue deformation due to anatomical respiratory contact forces. Projection of the tumor area inside the lung has been marked on the bottom surface of the lung. (a): meshing scheme of the unreformed geometry with minimum contact; (b)-(d): sequence of lung's deformation field through a complete phase of simulated respiration.

FE results (data) of a sufficiently large number of shapes of an organ are available. With such data, the essence of this technique is fitting a function that relates the geometry of each shape in the set as well as the loading parameters to its corresponding FE displacements. After training the model through this fitting process, the displacements of any organ with a shape not included in the set can be obtained by inputting its geometry parameters along with the loading information into the model. Employing SFEM for the

lung's biomechanical modeling can facilitate fast prediction of the lung's tissue motion and deformation during a tumor ablative procedure such as LDR brachytherapy. Such fast prediction is very important for developing a clinical lung brachytherapy system.

7.3 Closing Remarks

Different types of lung's tissue motion and deformation can be characterized and modeled through a combination of different techniques such as image processing, mathematical representations, machine learning, and biomechanical modeling, as presented in this thesis. Selecting the appropriate method for each case can be decided based on the nature of the deformation's cause, occurrence stage, and other specific requirements of the application. The proposed models developed for the lung's motion and deformation compensation is a substantial incremental step towards development of the ongoing system for minimally invasive tumor ablative procedures. These models are expected to improve the accuracy of such procedures significantly leading to their reliable clinical utility. However, further investigations involving *in vivo* experiments are required for assessing the reliability and accuracy of the proposed techniques in clinical applications as suggested in this Chapter.

Appendices

Appendix 1: Permission to reproduce the papers, which has been published under IEEE copyright, in this thesis.

Ali Sadeghi Naini

From: j.hansson
Sent: March-13-11 1:53 PM
To: Ali Sadeghi
Subject: Re: Including My IEEE Published Papers in the PhD Thesis

Comments/Response to Case ID: 00014086
From: Jacqueline Hansson Date: 03/13/2011

Dear Ali Sadeghi:

In response to your email below, we are happy to grant you this permission to reprint your below described IEEE copyrighted papers in your thesis and, if you wish, have your paper placed on your university's website. The following requirements must be satisfied before we can consider this permission grant final:

(1) The following IEEE copyright/credit notice must be placed prominently on the first page of the reprinted material, with the appropriate details filled in: © [year of original publication] IEEE. Reprinted, with permission, from [author names, paper title, IEEE publication title, and month/year of publication].

(2) The following message should be displayed at the beginning of the credits or in an appropriate place on the website: This material is posted here with permission of the IEEE. Such permission of the IEEE does not in any way imply IEEE endorsement of any of The University of Western Ontario's products or services. Internal or personal use of this material is permitted. However, permission to reprint/republish this material for advertising or promotional purposes or for creating new collective works for resale or redistribution must be obtained from the IEEE by writing to pubspermissions@ieee.org. By choosing to view this material, you agree to all provisions of the copyright laws protecting it.

If applicable, the Library and Archives of Canada may supply single copies of the dissertation.

Sincerely,
Jacqueline Hansson, Coordinator
© © © © © © © © © © © © © © © © © ©
IEEE Intellectual Property Rights Office

IEEE - - Fostering technological innovation and excellence for the benefit of humanity.
© © © © © © © © © © © © © © © © © ©

2011-03-08

Dear Sir/Madam,

I'm writing in order to get your permission for including the following papers I authored which were published under IEEE copyright in IEEE Transaction on Biomedical Engineering as two separate chapters in my thesis. The thesis is to be submitted in partial fulfillment of the requirements for the degree of Doctor of Philosophy to The School of Graduate and Postdoctoral Studies, The University of Western Ontario. The papers' information are listed below.

- A. Sadeghi Naini, T.Y. Lee, R.V. Patel, A. Samani, "Estimation of lung's air volume and its variations throughout respiratory CT image sequences", IEEE Transaction on Biomedical Engineering, vol. 58, issue 1, pp. 152-158,DOI: 10.1109/TBME.2010.2086457, IEEE, 2011.

- A. Sadeghi Naini, R.V. Patel, A. Samani, "CT enhanced ultrasound image of a totally deflated lung for image-guided minimally invasive tumor ablative procedures", IEEE Transaction on Biomedical Engineering, vol. 57, issue 10, pp. 2627-2630, DOI: 10.1109/TBME.2010.2058110, IEEE, 2010.

I appreciate your time in advance and looking forward to hearing from you soon,

Best regards,

Ali Sadeghi Naini, M.Sc.
Ph.D. Candidate / CAMI NSERC-CREATE Scholar / Research Assistant
Department of Electrical & Computer Engineering |
Canadian Surgical Technologies & Advanced Robotics (CSTAR) |
Imaging Research Laboratories, Robarts Research Institute (RRI)
The University of Western Ontario

Appendix 2: Permission to reproduce the paper, which has been published under the American Association of Physicists in Medicine (AAPM) copyright, in this thesis.

Ali Sadeghi Naini

From: Medical Physics Journal
Sent: March-09-11 6:24am
To: Ali Sadeghi
Subject: Re: Including My AAPM Published Paper in the PhD Thesis

Hi Ali,

Thank you for your email. Yes, you may have permission to use the material for your thesis.

Penny Slattery
Journal Manager

On Tue, Mar 8, 2011 at 7:14 PM, Ali Sadeghi

2011-03-08

Dear Sir/Madam,

I'm writing in order to get your permission for including the following paper I authored which was published under AAPM copyright in *Medical Physics* as a chapter in my thesis. The thesis is to be submitted in partial fulfillment of the requirements for the degree of Doctor of Philosophy to *The School of Graduate and Postdoctoral Studies*, *The University of Western Ontario*. The paper information is listed below.

- A. Sadeghi Naini, G. Pierce, T.Y. Lee, R.V. Patel, A. Samani, "*CT image construction of a totally deflated lung using deformable model extrapolation*", Medical Physics, vol. 38, issue 2, pp. 872-883, DOI:10.1118/1.3531985, AAPM, 2011.

I appreciate your time in advance and looking forward to hearing from you soon,

Best regards,

Ali Sadeghi Naini, M.Sc.
Ph.D. Candidate / CAMI NSERC-CREATE Scholar / Research Assistant
Department of Electrical & Computer Engineering |
Canadian Surgical Technologies & Advanced Robotics (CSTAR) |
Imaging Research Laboratories, Robarts Research Institute (RRI)
The University of Western Ontario

Appendix 3: Permission to reproduce the paper, which has been submitted for publication under IEEE copyright, in this thesis.

Ali Sadeghi Naini

From: j.hansson
Sent: March-22-11 10:15 AM
To: Ali Sadeghi
Subject: Re: Including My Paper Submitted to IEEE-TBME in the PhD Thesis

Comments/Response to Case ID: 005C388B
From: Jacqueline Hansson Date: 03/22/2011

Dear Ali Sadeghi:

In response to your email below, we are happy to grant you this permission to reprint your below described IEEE copyrighted papers in your thesis and, if you wish, have your paper placed on your university's website. The following requirements must be satisfied before we can consider this permission grant final:

(1) The following IEEE copyright/credit notice must be placed prominently on the first page of the reprinted material, with the appropriate details filled in: © [year of original publication] IEEE. Reprinted, with permission, from [author names, paper title, IEEE publication title, and month/year of publication].

(2) The following message should be displayed at the beginning of the credits or in an appropriate place on the website: This material is posted here with permission of the IEEE. Such permission of the IEEE does not in any way imply IEEE endorsement of any of The University of Western Ontario's products or services. Internal or personal use of this material is permitted. However, permission to reprint/republish this material for advertising or promotional purposes or for creating new collective works for resale or redistribution must be obtained from the IEEE by writing to pubspermissions@ieee.org. By choosing to view this material, you agree to all provisions of the copyright laws protecting it.

If applicable, the Library and Archives of Canada may supply single copies of the dissertation.

Sincerely,
Jacqueline Hansson, Coordinator
© © © © © © © © © © © © © © © © © ©
IEEE Intellectual Property Rights Office

IEEE - - Fostering technological innovation and excellence for the benefit of humanity.
© © © © © © © © © © © © © © © © © ©

2011-03-21

Dear Sir/Madam,

I'm writing in order to get your permission for including the following papers I authored which were recently submitted for publication in IEEE Transaction on Biomedical Engineering as a chapter in my thesis. The copyright of this paper has been transferred to IEEE upon submission. The thesis is to be submitted in partial fulfillment of the requirements for the degree of Doctor of Philosophy to The School of Graduate and Postdoctoral Studies, The University of Western Ontario. The papers' information is listed below.

- A. Sadeghi Naini, R.V. Patel, A. Samani, "Measurement of lung hyperelastic properties using inverse finite element approach", Submitted to IEEE Transaction on Biomedical Engineering, IEEE, 2011.

I appreciate your time in advance and looking forward to hearing from you soon,

Best regards,

Ali Sadeghi Naini, M.Sc.
Ph.D. Candidate / CAMI NSERC-CREATE Scholar / Research Assistant
Department of Electrical & Computer Engineering |
Canadian Surgical Technologies & Advanced Robotics (CSTAR) |
Imaging Research Laboratories, Robarts Research Institute (RRI)
The University of Western Ontario

Appendix 4: Permission to reproduce the paper, which has been published under Photo-Optical Instrumentation Engineers (SPIE) copyright, in this thesis.

Ali Sadeghi Naini

From: Scott McNeill
Sent: March-14-11 12:11 PM
To: Ali Sadeghi
Subject: RE: Including My SPIE Published Paper in the PhD Thesis

Dear Ali Sadeghi,

Thank you for seeking permission from SPIE to reprint material from our publications. As an author of the cited work, you retain co-owner rights to the original content therein. Publisher's permission is hereby granted under the following conditions: (1) the material to be used has appeared in our publication without credit or acknowledgment to another source; and (2) you credit the original SPIE publication. Include the authors' names, title of paper, volume title, SPIE volume number, and year of publication in your credit statement.

Sincerely,

Scott McNeill for
Eric Pepper, Director of Publications
SPIE

From: Ali Sadeghi
Sent: Tuesday, March 08, 2011 4:15 PM
To: copyrights
Subject: Including My SPIE Published Paper in the PhD Thesis

2011-03-08

Dear Sir/Madam,

I'm writing in order to get your permission for including the following paper I authored which was published under SPIE copyright in *Proc. of SPIE Medical Imaging 2011* in my thesis. The thesis is to be submitted in partial fulfillment of the requirements for the degree of Doctor of Philosophy to *The School of Graduate and Postdoctoral Studies, The University of Western Ontario*. The paper information is listed below.

- A. Sadeghi Naini, R. V. Patel, A. Samani, "*Effects of deflated lung's geometry simplifications on the biomechanical model of its tumor motion: a phantom study*", Proc. of SPIE Medical Imaging 2011: Visualization, Image-Guided Procedures, and Modeling, vol. 7964, 79642F, Orlando, Florida, USA, February 2011.

I appreciate your time in advance and looking forward to hearing from you soon,
Best regards,

Ali Sadeghi Naini, M.Sc.
Ph.D. Candidate / CAMI NSERC-CREATE Scholar / Research Assistant
Department of Electrical & Computer Engineering |
Canadian Surgical Technologies & Advanced Robotics (CSTAR) |
Imaging Research Laboratories, Robarts Research Institute (RRI)
The University of Western Ontario

Curriculum Vitae

Name **Ali Sadeghi Naini**

Post-secondary Education and Degrees

University of Isfahan (UI)
Isfahan, Isfahan, IRAN
1999-2004, B.Sc., Computer Engineering, Software Engineering

Tehran Polytechnic University (AUT)
Tehran, Tehran, IRAN
2004-2006, M.Sc., Computer Engineering, Artificial Intelligence

The University of Western Ontario (UWO)
London, Ontario, CANADA
2008-2011, Ph.D., Electrical and Computer Engineering, Biomedical Systems

Honors and Awards

Distinctions:

- **Achieved Honors Degree Certificate,** Certificated by the University Vice-president in educational affairs, Tehran Polytechnic University, Authenticated by the Ministry of Science, Research & Technology, Tehran, IRAN, 2006.
- **Distinguished Honored student** by the Office of Exceptional Talents and Honored Students, Tehran Polytechnic University, Tehran, IRAN, 2006.
- **Gold medalist** among M.Sc. students of Computer Engineering, Computer Engineering and Information Technology Department, Tehran Polytechnic University, Tehran, IRAN, 2004 - 2006.

Research Awards:

- **GTA Union Scholarship** for Outstanding Academic Achievements, Graduate Teaching Assistants (GTA) Union, The University of Western Ontario, London, Ontario, CANADA, 2011, ($500).
- **Dr. Alfred Jay Award Runner up** for Demonstrating Innovation and Entrepreneurship in PhD Field of Research Study, Department of Medical Biophysics, Schulich School of Medicine and Dentistry, The University of Western Ontario, London, Ontario, CANADA, 2011.
- **CAMI NSERC-CREATE Scholarship**, Computer-Assisted Medical Interventions (CAMI) Collaborative Research and Training Experience (CREATE) Program at The University of Western Ontario, Natural Sciences and Engineering Research Council (NSERC) of CANADA, 2010 - 2011, ($21000 over 2 years).
- **Conference Travel Grants**, Department of Electrical and Computer Engineering, The University of Western Ontario, London, Ontario, CANADA, Awarded in 2010 and 2011, (Two $500 grants).

- **Best Medical Imaging Paper Award**, 5th Canadian Student Conference on Biomedical Computing and Engineering (CSCBCE 2010), Waterloo, Ontario, CANADA, 2010.
- **Prasanna Mohan Scholarship,** Graduate Teaching Assistants (GTA) Union, The University of Western Ontario, London, Ontario, CANADA, 2010, ($1000).
- **Western Graduate Research Scholarship (WGRS) / Western Engineering Scholarship (WES)**, The University of Western Ontario, London, Ontario, CANADA, 2008 - 2011, ($52500 over 3.5 years).
- **Research Grants for Ph.D. studies,** The University of Western Ontario, London, Ontario, CANADA, 2008 - 2011, ($38000 over 3.5 years).
- **Conference Travel Grant**, Office of Exceptional Talents and Honored Students, Tehran Polytechnic University, Tehran, IRAN, 2006, ($300).
- **Full Ph.D. Scholarship**, Nominated by the Tehran Polytechnic University, Awarded by the Ministry of Science, Research & Technology: one of the 100 awardees awarded by the ministry in all disciplines over the nation, IRAN, 2007, (~$14000 over 4 years), Declined.

Related Work Experience

Research Experiences

- **CAMI NSERC- CREATE Scholar**, Natural Sciences and Engineering Research Council (NSERC) of CANADA's Collaborative Research and Training Experience (CREATE) Program in Computer-Assisted Medical Interventions (CAMI), The University of Western Ontario, 2010 - 2011.
- **Graduate Research Assistant (GRA)**, Imaging Research Laboratories, Robarts Research Institute (RRI), London, Ontario, CANADA, 2008 - 2011.
- **Graduate Research Assistant (GRA)**, Canadian Surgical Technologies & Advanced Robotics (CSTAR), Lawson Health Research Institute (LHRI), London Health Sciences Centre (LHSC), London, Ontario, CANADA, January 2008 - 2011.
- **Graduate Research Assistant (GRA)**, Biomedical Systems Group, Department of Electrical and Computer Engineering, The University of Western Ontario, London, Ontario, CANADA, January 2008 - 2011.
- **Graduate Research Assistant (GRA)**, Laboratory for Intelligent Voice & Speech Processing, Computer Engineering and Information Technology Department, Tehran Polytechnic University, Tehran, IRAN, 2005 - 2007.

Teaching Experiences

- **Graduate Teaching Assistant (GTA)** for *"Electromechanics"* course, Department of Electrical and Computer Engineering, The University of Western Ontario, London, Ontario, CANADA, winter 2011.
- **Graduate Teaching Assistant (GTA)** for *"Electrical Instrumentation and measurement"* course, Department of Electrical and Computer Engineering, The University of Western Ontario, London, Ontario, CANADA, fall 2010.

- **Graduate Teaching Assistant (GTA)** for *"Engineering Analysis of Physiological Systems"* course, Department of Electrical and Computer Engineering, The University of Western Ontario, London, Ontario, CANADA, winter 2009, winter 2010.
- **Graduate Teaching Assistant (GTA)** for *"Digital Logic Systems"* course, Department of Electrical and Computer Engineering, The University of Western Ontario, London, Ontario, CANADA, fall 2008, fall 2009.
- **Graduate Teaching Assistant (GTA)** for *"Digital Logic Design"* course, Department of Electrical and Computer Engineering, University of Windsor, Windsor, Ontario, CANADA, fall 2007.
- **Instructor** for *"UML and Java Programming"* course, Futurz Curriculum, NIIT Tehran Center (Mitco), Tehran, IRAN, spring & summer 2006.
- **Instructor** for *"Computer Fundamentals and Applications"* course (For 3 separate groups), a first year course for student of architecture, librarianship and public affairs, University of Applied Science and Technology, Tehran, IRAN, winter & spring 2006.
- **Instructor** for *"Programming Fundamentals using Pascal"* course, a first year course for students of computer graphics, University of Applied Science and Technology, Tehran, IRAN, winter 2006.
- **Graduate** Teaching Assistant (GTA) for *"Signals & Systems"* course, Computer Engineering and Information Technology Department, Tehran Polytechnic University, Tehran, IRAN, fall 2005 & winter 2006.

Scholarly Activities / Memberships

- **Reviewer** for Medical Image Computing and Computer-Assisted Intervention (MICCAI) Society, Since 2011.
- **Reviewer** for BMC Medical Imaging Journal, Since 2010.
- **Reviewer** for Iranian Journal of Electrical and Computer Engineering (IJECE), Since 2009.
- **Member** of Biomedical Imaging Research Centre (BIRC), London, Ontario, Canada, Since 2010.

Publications

Peer-Reviewed Journal Papers

- **A. Sadeghi Naini**, G. Pierce, T. Y. Lee, R. V. Patel, A. Samani, "*CT image construction of a totally deflated lung using deformable model extrapolation*", Medical Physics, vol. 38, issue 2, pp. 872-883, DOI:10.1118/1.3531985, AAPM, 2011.
- **A. Sadeghi Naini**, T. Y. Lee, R. V. Patel, A. Samani, "*Estimation of lung's air volume and its variations throughout respiratory CT image sequences*", IEEE Transaction on Biomedical Engineering, vol. 58, issue 1, pp. 152-158, DOI: 10.1109/TBME.2010.2086457, IEEE, 2011.
- S. R. Mousavi, I. Khalaji, **A. Sadeghi Naini**, K. Raahemifar, A. Samani, "*Statistical finite element method for real-time tissue deformation estimation*", In Press, Computer Methods in Biomechanics and Biomedical Engineering, DOI: 10.1080/10255842.2010.550889, Taylor & Francis, 2011.

- **A. Sadeghi Naini**, R. V. Patel, A. Samani, "*CT enhanced ultrasound image of a totally deflated lung for image-guided minimally invasive tumor ablative procedures*", IEEE Transaction on Biomedical Engineering, vol. 57, issue 10, pp. 2627-2630, DOI: 10.1109/TBME.2010.2058110, IEEE, 2010.
- **A. Sadeghi Naini**, M. M. Homayounpour, A. Samani, "*A real-time trained system for robust speaker verification using relative space of anchor models*", Computer Speech & Language, vol. 24, issue 4, pp. 545-561, DOI:10.1016/j.csl.2009.07.002, Elsevier, 2010.
- A. Asgary, **A. Sadeghi Naini**, J. Levy, "*Intelligent security systems engineering for modeling fire critical incidents: towards sustainable security*", Journal of Systems Science and Systems Engineering, vol. 18, No. 4, pp. 477-488., DOI: 10.1007/s11518-009-5121-2, Springer, 2009.

Submitted/ Under Revision Journal Papers

- **A. Sadeghi Naini**, R. V. Patel, A. Samani, "*Measurement of lung hyperelastic properties using inverse finite element approach*", Under Revision in IEEE Transaction on Biomedical Engineering, IEEE, 2011.
- A. Asgary, **A. Sadeghi Naini**, "*Predicting business continuity planning by businesses using neural networks*", Under Revision in Intelligent Systems in Accounting, Finance & Management, John Wiley & Sons, 2011.
- A. Asgary, **A. Sadeghi Naini**, "*Modeling the risk of structural fire incidents using a self organizing map*", Under Revision in Fire Safety Journal, Elsevier, 2011.
- **A. Sadeghi Naini**, Z. Shirzadi, A. Samani, "*Modeling Deflated Lung's Tumor Motion of Respiratory Contact Forces for Minimally Invasive Tumor Ablative Procedures*", To be Submitted to IEEE Transaction on Biomedical Engineering, IEEE, 2011.

Refereed Conference Papers

- **A. Sadeghi Naini**, R. V. Patel, A. Samani, "*Effects of deflated lung's geometry simplifications on the biomechanical model of its tumor motion: a phantom study*", Proc. of SPIE Medical Imaging 2011: Visualization, Image-Guided Procedures, and Modeling, vol. 7964, 79642F, Orlando, Florida, USA, February 2011.
- **A. Sadeghi Naini**, R. V. Patel, A. Samani, "*A totally deflated lung's CT image construction by means of extrapolated deformable registration*", Proc. of SPIE Medical Imaging 2011: Image Processing, vol. 7962, 796228, Orlando, Florida, USA, February 2011.
- **A. Sadeghi Naini**, R. V. Patel, A. Samani, "*Application of a respiratory CT sequence's combined histogram to estimate intra-sequence lung's air volume variations*", Proc. of the 5th Canadian Student Conference on Biomedical Computing and Engineering (CSCBCE 2010), pp. 21-25, Waterloo, Ontario, CANADA, May 2010. **(Achieved The Best Medical Imaging Paper Award)**.
- A. Asgary, **A. Sadeghi Naini**, A. Kong, "*Modeling loss and no-loss fire incidents using artificial neural network: case of Toronto*", Proc. of the 2009 IEEE Toronto International Conference – Science and Technology for Humanity (TIC-STH 2009), pp. 159-163, Toronto, Ontario, CANADA, September 2009.
- **A. Sadeghi Naini**, R. V. Patel, A. Samani, "*CT image construction of the lung in a totally deflated mode*", Proc. of the 2009 IEEE International Symposium on Biomedical Imaging: From Nano to Macro (ISBI 2009), pp. 578-581, Boston, Massachusetts, USA, June 2009.
- **A. Sadeghi Naini**, M. M. Homayounpour, "*Speaker age & sex identification based on the Jitter, Shimmer and MFCC Mean using supervised and unsupervised discriminative classification methods*", Proc. of the 8th International Conference on Signal Processing (ICSP 2006), IEEE, vol. 1, Article number 4128931, Guilin, CHINA, November 2006.

- **A. Sadeghi Naini**, M. M. Homayounpour, "*Feature extraction for speaker recognition based on the fusion of speech signal's ranked sub-bands*", Proc. of the 14th CSI Computer Conference (CSICC2009), Tehran, IRAN, March 2009.
- **A. Sadeghi Naini**, M. M. Homayounpour, "*Speaker recognition in the state space of reference speakers*", Proc. of the 15th Iranian Conference on Electrical Engineering (ICEE2007), Tehran, IRAN, May 2007.
- **A. Sadeghi Naini**, H. Beigy, "*ELearn++: A novel incremental learning algorithm for MLP neural networks*", Proc. of the 12th International CSI Computer Conference (CSICC2007), pp. 596-604, Tehran, IRAN, February 2007.
- **A. Sadeghi Naini**, M. Rahmati, *"Introducing a compression/decompression framework for human bones model motions based on constrained polynomial regression and nonlinear optimization*", Proc. of the 11th International CSI Computer Conference (CSICC2006), Tehran, IRAN, January 2006.

Refereed Journal/Conference Abstracts

- **A. Sadeghi Naini**, *"Modeling Lung Tissue Motions and Deformations: Applications in Tumor Ablative Procedures"*, Medical Physics PhD Abstracts, AAPM, 2011.
- Z. Shirzadi, **A. Sadeghi Naini**, A. Samani, "*Respiratory Tumor Motion Estimation during Lung Brachytherapy*", Proc. Of the 6th Canadian Student Conference on Biomedical Computing and Engineering (CSCBCE 2011), pp. 115, London, Ontario, CANADA, May 2011.
- **A. Sadeghi Naini**, R. V. Patel, A. Samani, "*Modeling lung tissue local deformations in a full deflation process*", Proc. Of the 9th Imaging Network Ontario (ImNO) Symposium, Toronto, Ontario, Canada, January 2011.
- **A. Sadeghi Naini**, R. V. Patel, A. Samani, "*CT/US guided minimally invasive lung brachytherapy*", Accepted as a Scientific Formal (Paper) Presentation in Radiological Society of North America's 96th Scientific Assembly and Annual Meeting (RSNA 2010), Chicago, Illinois, USA, November 2010.

Dissertations

- **A. Sadeghi Naini**, *"Modeling Lung Tissue Motions and Deformations: Applications in Tumor Ablative Procedures"*, Ph.D. dissertation, The University of Western Ontario, London, Ontario, CANADA, June 2011.
- **A. Sadeghi Naini**, "*Speaker Recognition Based on the Fusion and State Space of Eigen Speakers*", M.Sc. dissertation, Tehran Polytechnic University, Tehran, IRAN, December 2006.
- **A. Sadeghi Naini**, *"Design and Implementation of a POP3-SMTP-MIME Mail Server with the Ability of Sending and Receiving Mails in Persian"*, B.Sc. final project and dissertation, University of Isfahan, Isfahan, IRAN, August 2004.